

Remote sensing of red and far-red sun-induced
chlorophyll fluorescence to estimate gross primary
productivity and plant stress in sugar beet

Inaugural-Dissertation

zur

Erlangung des Doktorgrades

der Mathematisch-Naturwissenschaftlichen Fakultät

der Universität zu Köln

vorgelegt von

Sebastian Wieneke

aus Steinheim

Köln

2016

Berichtersteller:

Prof. Dr. K. Schneider

Prof. Dr. S. Crewell

Prof. Dr. U. Rascher

Tag der mündlichen Prüfung:

25.01.2017

Abstract

Without photosynthesis, life on Earth as we know it would not be possible. The quantification of photosynthesis and its spatio-temporal description from canopy to global scales is one of the key challenges in terrestrial ecology. Light absorbed by plants can be used for the photosynthetic process, reemitted as fluorescence or released as heat (non-photochemical Quenching, NPQ). Recently developed methods allow assessing sun induced chlorophyll fluorescence (F) by vegetation from remote sensing platforms. Due to its direct physical link to photosynthesis, F opens new possibilities to quantify photosynthesis (usually defined as gross primary productivity, GPP) and detect plant stress in space and time.

In this thesis, seasonally and spatially resolved datasets from novel ground (*SIF-Sys*) and airborne (*HyPlant*) measurement systems are used to analyze the spatio-temporal relationships between F , the photochemical reflectance index (PRI), which is linked to NPQ, and the efficiency of light to carbon conversion (light use efficiency, LUE) under changing environmental conditions. It was found that the combination of red and far-red fluorescence yields ($F_{687\text{yield}}$ and $F_{760\text{yield}}$) and PRI explain 65% of intra-daily and 89% of inter-daily changes in LUE of sugar beet plants. In addition, airborne observations are used to assess the spatiotemporal variation of $F_{760\text{yield}}$, $F_{687\text{yield}}$, the ratio between red- and far-red fluorescence (F_{ratio}) and the enhanced vegetation index (EVI) for different plants within a flight line over the course of a day. Results demonstrate that $F_{760\text{yield}}$ and F_{ratio} have strong variability in time and between crop types suffering from different levels of water shortage, indicating a strong sensitivity of F products to plant stress reactions.

The findings described above are used to develop an empirical GPP model (GPP_{MR}) based on $F_{687\text{yield}}$, $F_{760\text{yield}}$ and PRI. Estimated GPP is then validated with GPP measurements derived from an eddy covariance tower (GPP_{EC}) and also compared with estimates of GPP derived from currently used models employing fluorescence and greenness-based vegetation indices. Results show that the newly developed model combining $F_{760\text{yield}}$, $F_{687\text{yield}}$ and PRI performs best in predicting intra- and inter-daily changes in GPP. The application of the GPP models to spatio-temporal datasets demonstrates that, in general, fluorescence-based estimations better represent spatial variability in GPP than the ones based on common greenness-based vegetation indices. Finally, a new modeling scheme based on the photosynthetic energy balance to predict GPP by PRI and the total fluorescence signal (F_{tot}) in a more process oriented manner is proposed.

In conclusion, this thesis provides evidence that the use of sun induced fluorescence improves estimates of GPP. However the most promising results are found when combining F_{yield} and PRI. In addition, it is shown that the ratio between red and far-red sun-induced fluorescence and their yields shows large potential for identifying spatio-temporal plant adaptation strategies in response to environmental stress.

Zusammenfassung

Ohne den Prozess der Photosynthese wäre das Leben auf der Erde, so wie wir es kennen, nicht möglich. Die Quantifizierung des Photosynthese-Prozesses und die Darstellung seiner räumlichen und zeitlichen Adaptierung ist eine der zentralen Herausforderungen in der terrestrischen Umweltforschung. Von Pflanzen absorbiertes Licht kann für den Photosynthese Prozess genutzt, oder aber auch in Form von Wärme (nichtphotochemisches Quenching, NPQ) oder als Fluoreszenz abgegeben werden. Jüngste Fortschritte in der Sensorentechnik ermöglichen es nun, die von der Vegetation emittierte, sonneninduzierte Chlorophyll Fluoreszenz (F) mit Fernerkundungsmethoden zu erfassen. Aufgrund der direkten physikalischen Verbindung zwischen Fluoreszenz und Photosynthese eröffnen sich dadurch neue Möglichkeiten, die Photosynthese-Leistung (normalerweise beschrieben als brutto Primärproduktion, GPP) räumlich und zeitlich zu quantifizieren und Pflanzenstress zu bestimmen.

In dieser Dissertation wurden neuartigen boden- (*SIF-System*) und flugzeuggestützte (*HyPlant*) gestützten Messsysteme genutzt, um die zeitlichen und räumlichen Beziehungen zwischen F, dem photochemischen Reflexionsindex (PRI – als Indikator für NPQ) und der Lichtnutzungseffizienz (LUE) unter wechselnden Umweltbedingungen zu analysieren. Dabei hat sich gezeigt, dass die Kombination aus roter und fern-roter Fluoreszenz Effizienz ($F_{687\text{yield}}$ und $F_{760\text{yield}}$) und dem PRI 65% der täglichen und 89% der saisonalen Variabilität der LUE von Zuckerrübe erklärt. Zusätzlich wurden flugzeuggestützte Messungen genutzt, um die räumliche und zeitliche Variabilität von $F_{760\text{yield}}$, $F_{680\text{yield}}$, dem Verhältnis zwischen roter und fern-roter Fluoreszenz (F_{ratio}) und dem sogenannten verbesserten Vegetationsindex (EVI) innerhalb eines Flugstreifens und eines Tages zu bestimmen. Die Ergebnisse zeigen in Abhängigkeit zur Wasserverfügbarkeit eine hohe Variabilität von $F_{760\text{yield}}$ und F_{ratio} im Laufe eines Tages und hinsichtlich der Feldfruchtart. Dies deutet darauf hin, dass Fluoreszenz-Produkte sensitiv auf Pflanzenstress reagieren.

Die oben beschriebenen Ergebnisse wurden genutzt, um ein empirisches GPP Modell zu entwickeln, das auf $F_{760\text{yield}}$, $F_{687\text{yield}}$ und PRI basiert. Die Ergebnisse wurden anschließend mit GPP-Werten, die aus Eddy Kovarianz Messungen (GPP_{EC}) abgeleitet wurden, validiert und mit den Ergebnissen dreier derzeit genutzten Modellen verglichen, die auf Fluoreszenz und Reflexion basieren. Die Ergebnisse zeigen, dass das neuentwickelte Modell, welches auf F_{yield} und PRI Informationen basiert, die Tages- und saisonale Variabilität von GPP am besten bestimmt. Die Anwendung der Modelle auf räumlich aufgelöste Daten zeigt, dass generell fluoreszenzbasierte Modelle die räumliche Variabilität von GPP besser erfassen als das Modell, welches allein auf Reflexionsindizes basiert. Abschließend wird der Entwurf für ein Modell vorgeschlagen, welches, basierend auf der photosynthetischen Energiebilanz, den PRI und die absolute Fluoreszenz (F_{tot}) nutzt, um GPP in einer stärkeren prozessorientierten Weise zu bestimmen.

Zusammengefasst stellt diese Arbeit heraus, dass sonneninduzierte Fluoreszenz die Abschätzung von GPP verbessert, wobei insbesondere die Kombination aus F und PRI die vielversprechendsten Ergebnisse liefert. Zusätzlich wird gezeigt, dass das Verhältnis von roter zu fern-roter Fluoreszenz sowie F_{yield} ein großes Potenzial haben, um stressbedingte raumzeitlichen Pflanzenanpassungsstrategien abzubilden.

Contents

Abstract	i
Zusammenfassung	iii
List of Abbreviations	vi
1. Introduction	1
1.1. <i>Methods to estimate GPP</i>	<i>1</i>
1.2. <i>Remote sensing of GPP</i>	<i>3</i>
1.3. <i>The Transregional Collaborative Research Center 32</i>	<i>6</i>
1.4. <i>Aim of this Study</i>	<i>8</i>
1.5. <i>Structure of this Study</i>	<i>9</i>
2. The process of photosynthesis and its estimation	11
2.1. <i>Photosynthesis</i>	<i>11</i>
2.2. <i>Photosynthetic energy balance</i>	<i>20</i>
2.3. <i>Measuring photosynthetic activity on the leaf level</i>	<i>21</i>
2.4. <i>Measurements of photosynthetic activity on the canopy level</i>	<i>22</i>
2.5. <i>Retrieval of sun induced chlorophyll fluorescence</i>	<i>24</i>
2.6. <i>Modeling approaches for estimating GPP using remotely sensed F</i>	<i>29</i>
2.7. <i>Fluorescence as an estimator of plant stress</i>	<i>30</i>
3. Observations	33
3.1. <i>Study area (TR32)</i>	<i>33</i>
3.2. <i>Selhausen campaign 2012</i>	<i>34</i>
3.3. <i>Merzenhausen campaign 2015</i>	<i>38</i>
4. Model descriptions	45
4.1. <i>Data usage</i>	<i>45</i>
4.2. <i>Estimation of GPP</i>	<i>45</i>
4.3. <i>Spatio temporal changes of fAPAR_{VI} and F_{760yield}</i>	<i>49</i>
4.4. <i>Model validation</i>	<i>49</i>

4.5.	<i>Model uncertainties</i>	50
5.	Results	53
5.1.	<i>In situ measurements</i>	53
5.2.	<i>Plant adaptation strategies in time and space</i>	60
5.3.	<i>Fluorescence measurement uncertainty</i>	71
5.4.	<i>The correlation between GPP and F</i>	74
5.5.	<i>Intra- and inter-daily estimation of GPP</i>	75
5.6.	<i>Estimation of spatiotemporal GPP</i>	84
6.	Discussion	95
6.1.	<i>In situ measurements</i>	95
6.2.	<i>Remote sensing of intra- and inter-daily plant adaptation strategies</i>	97
6.3.	<i>Remote sensing of spatiotemporal plant adaptation strategies</i>	99
6.4.	<i>Estimation of intra- and inter-daily GPP</i>	100
6.5.	<i>Spatiotemporal estimation of GPP</i>	102
6.6.	<i>Model applicability for satellite based remote sensing data</i>	103
6.7.	<i>Measurement uncertainty of the SIF-Sys</i>	103
6.8.	<i>Reliability of retrieved F_{760} and F_{687} maps</i>	104
7.	Towards a mechanistic model linking fluorescence with photosynthesis ..	107
8.	Summary and Conclusion	115
9.	Outlook	118
	Appendix	119
	Bibliography	128
	Danksagung	143
	Erklärung	144
	Teilveröffentlichungen	145
	Lebenslauf	146

List of Abbreviations

ADP	= adenosine diphosphate
APAR	= absorbed photosynthetically active radiation
ATP	= adenosine triphosphate
b _{6f}	= cytochrome b _{6f}
BBCH	= Biologische Bundesanstalt, Bundessortenamt und Chemische Industrie
CET	= cyclic electron transport
CH ₂ O	= carbohydrates
CO ₂	= carbon dioxide
DOY	= day of the year
EC	= eddy covariance
ER	= evapotranspiration
EVI	= enhanced vegetation index
F	= sun-induced chlorophyll fluorescence
F ₆₈₇	= sun-induced chlorophyll fluorescence at 687 nm
F ₇₆₀	= sun-induced chlorophyll fluorescence at 760 nm
F _{tot}	= total sun-induced chlorophyll fluorescence
F _{ratio}	= ratio of the F peaks
F _{yield}	= sun-induced chlorophyll fluorescence yield
fAPAR	= fraction of absorbed photosynthetically active radiation
FDX	= ferredoxin
FLD method	= Fraunhofer line depth method
FLEX	= Fluorescence Explorer
FLOX	= fluorescence box
FNR	= ferredoxin NADP reductase
FWHM	= full width at half maximum
GEC	= Gas-Exchange Chamber
GOME-2	= Global Ozone Monitoring Experiment-2
GOSAT	= Greenhouse Gases Observing Satellite
GPP	= gross primary production
H ₂ O	= water
I	= irradiance
iFLD	= improved Fraunhofer line depth
L	= radiance
\tilde{L}	= apparent radiance
LUE	= light use efficiency
NADP ⁺	= oxidized nicotinamide adenine dinucleotide phosphate
NADPH	= reduced nicotinamide adenine dinucleotide phosphate

NDVI	= normalized difference vegetation index
NEE	= net ecosystem exchange
NPQ	= non-photochemical quenching
O	= oxygen
OCO-2	= Orbiting Carbon Observatory-2
PAR	= photosynthetically active radiation
PAM	= pulse-amplitude modulation
PAR	= photosynthetically active radiation
PAW	= plant available water
PC	= plastocyanin
PGA	= phosphoglycerate
PGAL	= phosphoglyceraldehyde
Pi	= inorganic phosphate
PQ	= plastoquinone
PRI	= photochemical reflectance index
PSI	= photosystem I
PSII	= photosystem II
R	= reflectance
\tilde{R}	= apparent reflectance
R_{eco}	= ecosystem respiration
R_{plant}	= plant respiration
RS	= remote sensing
R_{soil}	= soil respiration
RuBisCO	= ribulose bisphosphate carboxylase
RuBP	= ribulose bisphosphate
SCIAMACHY	= Scanning Imaging Absorption Spectrometer for Atmospheric Cartography
SFM	= spectral fitting method
SVP	= saturated vapor pressure
TR32	= Transregional Collaborative Research Centre 32
V_{cmax}	= maximum rate of carboxylation
VIs	= vegetation indices
VPD	= vapor pressure deficit

1. Introduction

Photosynthesis is a key process in terrestrial ecosystems. Life on earth, as we know it, would not be possible without it. Through the use of sunlight and water, carbon dioxide (CO_2) is assimilated by plants to produce biomass, while oxygen (O) is released (Farquhar et al., 2001). The biomass serves as food, fiber and energy, while the exchange of carbon and oxygen affects the composition of our atmosphere. Photosynthesis is, therefore, often termed as gross primary production (GPP) (Denman et al., 2007), which can be defined as the sum of the photosynthesis by all leaves measured or estimated at ecosystem scale over a certain time (Chapin et al., 2006). Furthermore, photosynthesis significantly controls the energy, water and carbon exchange between soil, vegetation and the atmosphere (Bonan, 1995). Ozanne et al. (2003) estimated that up to 90% of the CO_2 exchange between atmosphere and biosphere is related to photosynthesis. Therefore, an accurate estimation of actual GPP is critical for a comprehensive understanding of the carbon budget, however, this still is one of the key challenges in terrestrial geoscience (IPCC, 2013).

1.1. Methods to estimate GPP

The most direct measurement of photosynthesis can only be obtained at leaf level. By the combination of a high precision gas analyzer and a pulse-amplitude modulation (PAM) fluorometer, the two photosynthetic processes (the dark and light reactions) can be non-destructively probed. This method, however can hardly provide measurements for a full canopy, much less for a whole ecosystem (Schreiber, 2004).

The CO_2 exchange (net ecosystem exchange; NEE) can be measured by gas exchange chambers for one or several plants at once. The CO_2 concentration is measured within the open chamber, then the chamber is closed for a short time. The CO_2 exchange can be calculated from the increase of CO_2 within the chamber. To derive GPP from these measurements, the CO_2 release by the plant (plant respiration) and by the soil (soil respiration) have to be known (Reicosky, 1990). Although the estimation of GPP on larger spatial extend is not possible with this method, the heterogeneity within the study area can be described by moving the chamber.

The CO_2 exchange between an ecosystem and the atmosphere can be estimated at a relatively high temporal resolution (ca. 30 min) by the eddy covariance (EC) method. However, these measurements only cover footprints of several hundred meters and are strongly affected by local setup and aerodynamic properties of the ecosystem (Baldocchi, 2008; Baldocchi et al., 2001).

The estimation of GPP at regional to global scales can be classified into three different methodological approaches: 1) process-based models; 2) measurement-based empirical upscaling models; or 3) models based on remotely sensed vegetation parameters. The different approaches are specified in the following paragraphs.

1) Process-based models explicitly describe the ecosystem dynamics by translating physical or biological processes into numerical formulas. The advantage of this modeling approach is that it allows analyzing the system behavior and the interactions between processes, from canopy to global scale (Sitch et al., 2003). A problem of process-based models is that their accuracy depends on a proper parameterization. Parameterization is a method to simplify processes which are too small-scale or complex to be numerically represented. Ideally the parameterization is derived from observations, but recent studies show that process-based models often use unrealistic parameterization, and that a more realistic parameterization would even result in deteriorated estimations (Bonan et al., 2012; Rogers, 2014; Schimel et al., 2015).

2) Empirical upscaling methods combine in-situ observations with empirical models (e.g. multi-tree ensemble (MTE) GPP by Jung et al. (2011)). Machine learning algorithms driven by substantial datasets from the global network of EC-Towers (FLUXNET c.f. Baldocchi et al. (2001)), meteorological data and information of land use can be utilized to estimate regional to global GPP. The main disadvantage of this method is that the accuracy of the GPP calculations is limited by the amount and quality of the observations. Validations of the MTE GPP show that seasonal patterns can be predicted well, but, due to environmental effects and disturbances (e.g. droughts, fires, heatwaves), inter annual variations are poorly captured. Furthermore, MTE GPP only estimates monthly values, which hampers the possibility to study daily variability (Jung et al., 2011, 2009).

3) Space- and airborne-based spectroscopy can be considered the only technology that continuously observes important information about vegetation status and functions on field to global scale. Typically, vegetation indices (VIs) derived from optical measurements are employed in estimating GPP, under the assumption that physiological plant processes and the biochemical composition of vegetation control the optical properties of vegetation canopies (Hilker et al., 2008). It is important to note that all products derived from remote sensing platforms are only related to the light reactions of photosynthesis. Since the estimation of GPP also requires information on the dark reactions and stomata conductance, models are needed to transfer RS information to GPP. With this work the remote sensing based approaches to estimate GPP will be further investigated.

1.2. Remote sensing of GPP

The foundation of basically all remote sensing (RS) approaches to estimate GPP is the resource balancing paradigm (Field et al., 1995), which hypothesizes that the plant's investment in the various resource-harvesting complexes is balanced, and that plant growth can be approximately estimated by measuring single growth-limiting factors. This idea is conceptualized in Monteith's light use efficiency model (Monteith, 1972; Monteith and Moss, 1977), and used in all RS-based GPP estimates (Eq. 1):

$$GPP = PAR \cdot fAPAR \cdot LUE \quad (1)$$

The model sets GPP in a proportional relationship with the incident photosynthetically active radiation (PAR), the fraction of PAR absorbed by the vegetation (fAPAR), and the photosynthetic light use efficiency (LUE; defined as the amount of $\mu\text{mol CO}_2$ absorbed per $\mu\text{mol photons}$). The challenge in RS is to parameterize the three terms of Monteith's equation. PAR is defined by the spectra of light, which can be accurately modeled by radiative transfer models. The challenge of estimating PAR is mainly connected to the estimation of cloud cover, where the uncertainty increases with higher spatial and temporal resolution. In this work, in-situ measurements of PAR were used to exclude uncertainty related to the use of modeled datasets.

1.2.1. Use of vegetation indices

According to Hilker et al. (2008), fAPAR can be estimated through various methods, some of them based on its empirical non-linear relationship to vegetation indices e.g., to the normalized difference vegetation index (NDVI). However, the saturation of VIs in dense canopies and their sensitivity to the background contributions of soil or non-photosynthetic vegetation components often leads to GPP being overestimated for sparse and less productive canopies and underestimated for dense and high productive canopies (Huete et al., 2002; Turner et al., 2003; Running et al., 2004; Xiao et al., 2008). Quantifying LUE is challenging, and direct measurements are not yet possible. Besides unrealistically assuming a constant LUE, more sophisticated approaches adjust biome-specific potential LUE values by using meteorological variables derived from in-situ measurements and geo-statistical modeling (Jung et al., 2011; Running et al., 2004; Ryu et al., 2011; Xiao et al., 2004). These approaches are based on vegetation greenness and do not show a direct mechanistic connection to actual photosynthesis, which is characterized by rapid and short-term adaptations to changing environmental conditions (e.g., fluctuating light, short term drought, etc.). Consequently, greenness-based approaches tend to be more related to potential than to actual photosynthetic rates (Meroni et al., 2009).

1.2.2. Use of sun induced chlorophyll fluorescence

Recently, sun-induced chlorophyll fluorescence (F) was proposed as a means to overcome the limitations mentioned previously when estimating GPP. Light energy absorbed by chlorophyll is channeled to three competitive pathways: (1) photosynthesis, (2) heat dissipation (non-photochemical quenching, NPQ), and (3) emission as fluorescence. Consequently, fluorescence is theoretically related to both APAR and LUE, which opens new perspectives to estimate GPP more accurately. Fluorescence light emitted by vegetation has a well-defined spectral shape, with two major peaks at 685nm ($\text{maxF}_{<685>}$; red) and 740nm ($\text{maxF}_{<740>}$; far-red) (Porcar-Castell et al., 2014). The radiance signal received at an optical sensor comprises two radiance fluxes: sunlight reflected by the surface and the emitted fluorescence. The fluorescence signal weakly adds to the reflected surface radiance (1-5% in the far-red), making its detection from RS challenging (Zarco-Tejada et al., 2000).

Analytical and technical developments nowadays allow fluorescence to be reliably measured using ground (Burkart et al., 2015; Cogliati et al., 2015a; Damm et al., 2010a), airborne (Damm et al., 2010b, 2011, 2014; Rossini et al., 2015; Rascher et al., 2015), and satellite sensors (Frankenberg et al., 2014; Guanter et al., 2012; Joiner et al., 2011). The latter is currently derived from sensors onboard OCO-2 (Orbiting Carbon Observatory 2), GOSAT (Greenhouse Gases Observing Satellite), GOME-2 (Global Ozone Monitoring Experiment-2) and SCIAMACHY (Scanning Imaging Absorption Spectrometer for Atmospheric Cartography). The primary objective of these missions is to track atmospheric carbon and ozone concentration, which results in fluorescence images with low spatial resolution (5 to 60km). Since the detection of atmospheric CO₂ concentration by these satellites is realized in the infrared part of the spectrum, the retrieval of F is furthermore only feasible for the far-red peak. The recently selected Fluorescence Explorer (FLEX) as part of the ESA Earth Explorer 8 mission will allow in the future (estimated launch 2022) an optimized global mapping of fluorescence in the red and far-red peak with a 300 meter spatial resolution.

Since the estimation of F from remote sensing platforms became feasible, several approaches to estimate GPP by using F were presented. In one of the first approaches, Frankenberg et al. (2011) showed that spatial and temporal patterns of F present a strong linear correlation with GPP and that this linear relationship can then be used to infer GPP from satellite F measurements. However, the assumption of a linear relationship between GPP and F is problematic, since GPP and F both depend on the amount of absorbed photosynthetic active radiation (APAR) and therefore are not independent. Furthermore, this approach was developed to estimate GPP from monthly averaged satellite images (GOSAT, GOME-2) of F with coarse spatial resolution (0.5°), and it is unclear if this approach is feasible for measurements of F at high spatial and temporal resolution.

An APAR-independent approach was proposed by Guanter et al. (2014), who suggested a semi-mechanistic model to estimate GPP on the basis of the relationship of LUE and F_{yield} . In contrast to the assumption that GPP and F are linearly connected, this model assumes that the LUE changes with F_{yield} . Since this approach was also developed for GOSAT satellite images, it is still unclear how this relationship develops during a day or a season. Furthermore, this model does not consider the dissipation of energy as heat (non-photochemical quenching; NPQ) which may result in an underdetermined system description. Recent studies proposed the photochemical reflectance index (PRI) (Gamon et al., 1992) as a proxy for LUE and as an indicator for NPQ activity (Porcar-Castell et al., 2012; Rahimzadeh-Bajgiran et al., 2012; Weng et al., 2006; Wu et al., 2015). Therefore, it is expected that the combination of F with PRI improves the estimation of GPP (Damm et al., 2015; Porcar-Castell et al., 2014; Wieneke et al., 2016).

Another idea to use fluorescence for GPP estimation is to use process-based models as data integration platform. Fluorescence can, for example, be used as an observational constraint for GPP (Parazoo et al., 2014). Based on van der Tol et al. (2014), Lee et al. (2015) incorporated the estimation of fluorescence into a land surface model by using an empirical relationship between the relative light saturation of photosynthesis and NPQ. Measured sun induced fluorescence can then be used as an observational constraint of the land surface model. Zhang et al. (2014) proposed to use sun induced fluorescence as an estimator for model sensitive parameters to improve the parameterization of land surface models.

Until now, most approaches to improve the estimation of GPP are based on empirical assumptions, either derived from active leaf level measurements of fluorescence or from coarse spatiotemporally resolved F images. Since active leaf level measurements of fluorescence are difficult to compare with passively measured F (Cendrero-Mateo et al., 2016), more field measurements with high temporal and spatial resolution are needed to improve the knowledge of the connection between F and GPP (Porcar-Castell et al., 2014).

1.3. The Transregional Collaborative Research Center 32

The research for this thesis was realized within the Transregional Collaborative Research Centre 32 (SFB/TR32) “*Patterns in Soil-Vegetation-Atmosphere Systems: Monitoring, Modeling, and Data Assimilation*”, funded by the German research foundation (DFG, Deutsche Forschungsgemeinschaft). The TR32 focuses on the research of energy, water and carbon exchange between soil, vegetation and atmosphere to better understand the underlying processes, interdependencies and resulting patterns. For this purpose the Rur catchment in western Germany was chosen as an extensive study area where many hydrologic, plant physiologic, and atmospheric key parameters were measured continuously over several years (project start; 2006) (Figure 1).

Since 2012 the yearly executed *HyPlant* campaign is embedded in the TR32 D2 project, designed to map sun induced chlorophyll fluorescence at 760nm (F_{760}) and 680nm (F_{680}) from aircraft at a high spatial resolution of 1m (c.f. Section 3.2.3 and 3.3.3). Also developed within the TR32 D2 project, a new ground spectrometer system (*SIF-Sys*) allows for continuous measurement of vegetation reflectance, F_{760} , F_{687} , and their yields (F_{760}^{yield} and F_{687}^{yield}) with high temporal (6s) and spectral (full width at half maximum (FWHM); 1nm) resolution (c.f. Section 3.3.1).

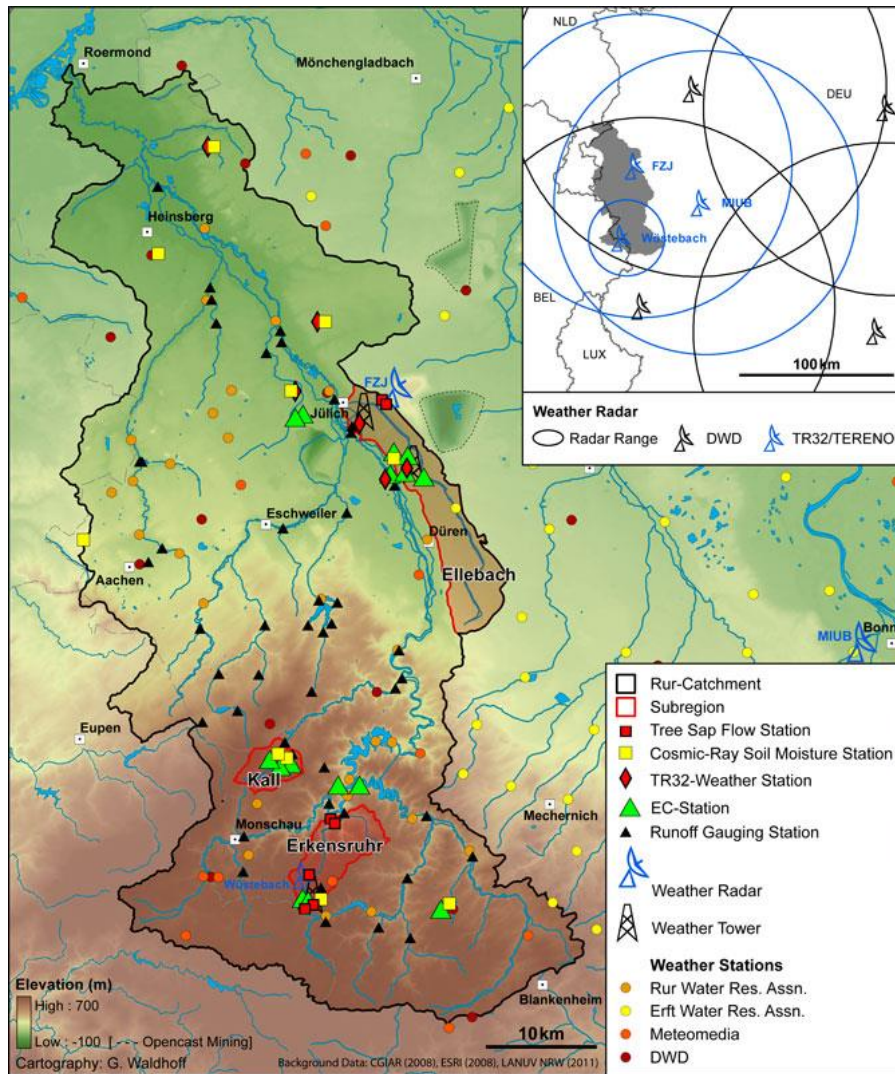


Figure 1: Study area of the Transregional Collaborative Research Centre 32 (SFB/TR32), located in the Rur catchment of western Germany. Map shows the location of several measurement stations and the intensive measurement sub regions (red line). Small map in the upper right corner shows the location of weather radar stations and their range.

Source: Transregional Collaborative Research Centre 32

1.4. Aim of this Study

The main purpose of this thesis is to investigate the spatiotemporal relationship of sun induced chlorophyll fluorescence, the photochemical reflectance index and light use efficiency, for a better system understanding towards an improved estimation of gross primary production from remote sensing data.

The in-situ acquired dataset of the *SIF-Sys* (15 days acquired within two months) with high temporal (6s sampling time) resolution, and airborne maps acquired by the HyPlant sensor (in 2012 & 2015) with high spatial (1m) resolution are presented with this thesis. This extensive dataset is used to describe and analyze the intra- and inter-daily relationship between $F_{760\text{yield}}$ and $F_{687\text{yield}}$, their ratio (F_{ratio}), the PRI and the LUE under changing environmental conditions (temperature and water availability) within sugar beet fields. From previous studies it is known that the PRI (photochemical reflectance index) serves as a good estimator for LUE (Cheng et al., 2013; Drolet et al., 2008; Rossini et al., 2010; Wu et al., 2015), while the relationship between F and LUE is less strong (Cheng et al., 2013). Due to the link of the additive signal of red- and far-red F to total sun-induced fluorescence (F_{total}) and the relationship of PRI to NPQ (non-photochemical quenching) it is hypothesized, that:

A combination of $F_{760\text{yield}}$ and $F_{687\text{yield}}$ and PRI is a better predictor of LUE than each on its own.

The first null hypothesis of this work is, thus:

- 1) *The additive signal of $F_{760+687\text{yield}}$ does not add information to the prediction of changes in light use efficiency based solely on the PRI*

First maps of red- and far-red fluorescence are used to analyze spatial patterns of fluorescence and reflectance parameters. Since light absorbed by chlorophyll is in part re-emitted as fluorescence when the molecules return from excited to non-excited states, the intensity of the fluorescence signal is an indicator of photosynthetic energy conversion. Therefore, effects of plant adaptation to environmental conditions affecting photosynthesis should be detectable within fluorescence maps. Thus, it is hypothesized, that:

Plant adaptation strategies are detectable with airborne based F observations.

This leads to the second null hypothesis:

- 2) *Spatiotemporal plant adaptation strategies are not detectable within maps of red- and far-red fluorescence.*

In order to analyze the potential of fluorescence to estimate GPP, in-field and remote sensing measurements are used, employing four different approaches with increasing complexity: (i) the commonly used reflectance based LUE model by Monteith (1972); (ii) the empirical F-GPP relationship approach proposed by Frankenberg et al. (2011); (iii) the semi-mechanistic approach by Guanter et al. (2014); (iv) a newly developed multiple regression model on the basis of PRI and F. Estimates of 30 min and daily averaged GPP, as well as maps of GPP, are calculated by these four models. Results are compared with each other and validated with eddy-covariance-and gas exchange chamber measurements. It is hypothesized that:

Due to the consideration of NPQ by the use of the PRI the multiple regression model will result in better estimates of GPP.

This lead to the third null hypothesis:

- 3) *The PRI, as a proxy for NPQ, does not improve fluorescence based intra- and inter-daily GPP estimations*

The aim of this thesis is to reject all three null-hypotheses.

1.5. Structure of this Study

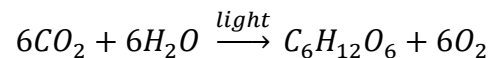
To fulfill the aims described in section 1.4 this study is structured as follows: The Introduction describes the state of the art of methods to estimate GPP and discusses the advantages of RS-based GPP estimates, in particular the ones based on sun-induced chlorophyll fluorescence (F). The aim of this study is also presented. Chapter 2 summarizes the general process of photosynthesis and its estimation. A special focus lies here on discussing the link between fluorescence and the photosynthetic process and the methods to retrieve F. In Chapter 3, the Observation sites of Selhausen and Merzenhausen are described. Chapter 4 describes the statistical Models used in this Study to estimate GPP and their uncertainty. In Chapter 5, the spatio-temporal model results are presented and compared to in-situ measurements for a validation of the model precision and accuracy. Chapter 6 presents a discussion on the potential of fluorescence-based observations to improve GPP estimation in space and time. In Chapter 7 a concept of a mechanistic model that links fluorescence with photosynthesis is presented. In Chapter 8 and 9 the findings of this study are summarized and an outlook for future improvements of fluorescence retrieval and measurements are given.

2. The process of photosynthesis and its estimation

In this chapter, an overview of the current knowledge about the photosynthetic process, its controlling mechanisms and response to environmental stress is given. The protection mechanisms of fluorescence and NPQ are described, and the state-of-the-art fluorescence retrieval methods are explained. Furthermore, a recently developed semi-mechanistically model approach to estimate GPP from fluorescence is presented, and the current knowledge of plant stress detection by fluorescence is introduced.

2.1. Photosynthesis

Photosynthesis is the process where plants assimilate carbon dioxide (CO₂) by using light energy and water (H₂O) to produce biomass in form of carbohydrates (CH₂O), and release oxygen O₂. The overall chemical reaction is defined as:



Carbohydrates are sugars that can be used by the plant to grow, for maintenance and for reproduction. Photosynthesis is controlled by three distinct processes: the light reactions, the dark reactions (Calvin-Cycle) and the stomata conductance. The light and dark reactions occur in the chloroplasts of leaves (Figure 2). The chloroplast consists of thylakoids and stroma. On the membrane of the thylakoid, the light reactions happen, while in the stroma CO₂ is converted to sugar by the dark reactions. The CO₂ needed for the dark reactions diffuses into the stroma through the stomata (Bonan, 2008).

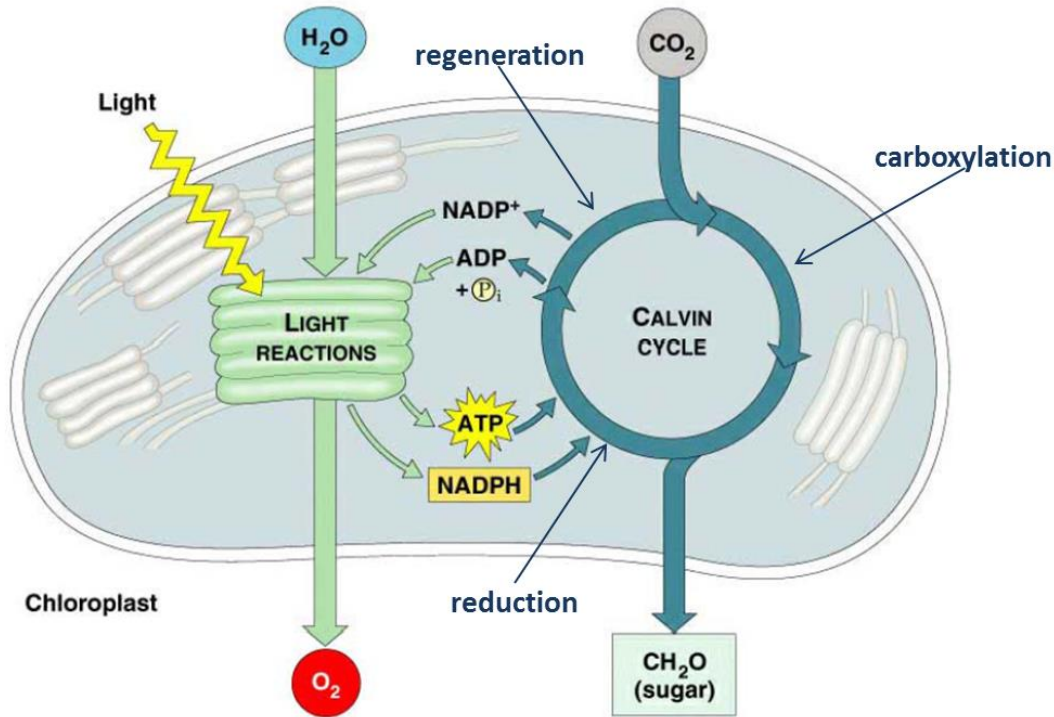


Figure 2: Light and dark reactions (Calvin-Cycle) within a chloroplast. During the light reactions water and light is used to regenerate the energy carrier $NADP^+$ (nicotinamide adenine dinucleotide phosphate) and ADP (adenosine diphosphate) to NADPH (nicotinamide adenine dinucleotide phosphate-oxidase) and ATP (adenosine triphosphate). Within the Calvin cycle NADPH and ATP are used to assimilate CO_2 and to produce carbohydrates (sugar).

Source: Pearson Education Inc. (2012)

2.1.1. Light reactions

The light reactions take place in the electron transport chain. This consists of a set of different complexes: photosystem II (PSII), cytochrome b_6f (b_6f), photosystem I (PS I), ferredoxin NADP reductase (FNR) and the ATP synthase. In addition to the complexes, mobile carriers - plastoquinone (PQ), plastocyanin (PC) and ferredoxin (FDX) - are also involved (Figure 3) (Lawlor, 2001).

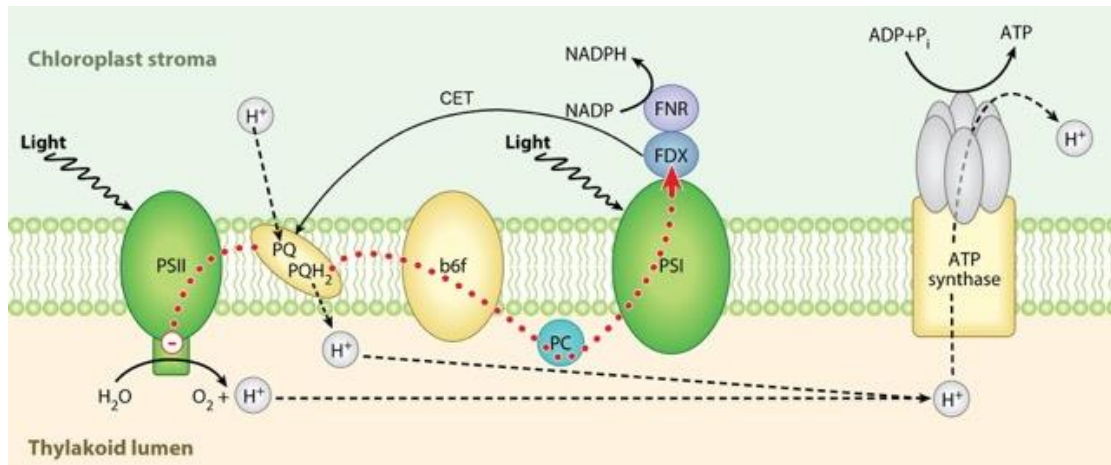


Figure 3: Electron transport chain of the thylakoid membrane. Electrons released in the oxidation of H_2O are transferred in the light along the photosynthetic electron transport chain via Photosystems I and II to Fdx which reduces NADPH via FNR. At the indicated points, protons are released into the thylakoid lumen for the synthesis of ATP via ATP synthase.

Source: adapted from Meyer et al., 2009

The membranes of the thylakoid contain chlorophyll and carotenoid pigments, which are able to absorb light energy (photons) and transfer this energy by resonance to the reaction center of PSII and PSI. The reaction centers of PSII and PSI differ in their chlorophyll *a* and *b* pigment composition. With a chlorophyll *a/b* ratio of 9, PSI has a higher chlorophyll *a* content as PSII (*a/b* ratio of 2.5). This results in slightly different absorption spectra. As a result, the electron transfer in PSII and PSI changes with the spectral properties of the incoming light. The PSII and PSI reaction centers are usually named after their red-peak absorption maximum as P680 (680 nm) and P700 (700 nm) respectively (Antal et al., 2013).

When a photon hits a chlorophyll or carotenoid molecule in Photosystem II, resonance energy is produced and transferred through neighboring chlorophyll or carotenoid molecule to the reaction center of PSII. Two electrons are subsequently released and transferred to the mobile carrier PQ. In addition to the two electrons, PQ also picks up two protons (H^+) from the stroma. The electrons lost from PSII are replaced by splitting up water (H_2O) molecules into oxygen (O_2) and protons, which are released into the thylakoid lumen. The PQ transports the two electrons to the cytochrome b_6/f complex, while the protons are released into the thylakoid lumen. By transferring the electrons to the next mobile carrier PC, the cytochrome b_6/f complex pumps two more protons into the thylakoid lumen, further increasing the electrochemical energy gradient. PC transports the electrons to PSI, where photons again energize electrons which are transferred over FDX to FNR. By being combined with the two electrons and a hydrogen ion, $NADP^+$ (oxidized nicotinamide adenine dinucleotide phosphate) can be

reduced to NADPH (reduced nicotinamide adenine dinucleotide phosphate). The electrochemical energy gradient created by the electron transport chain is utilized by the ATP synthase to create ATP (adenosine triphosphate) from ADP (adenosine diphosphate) and Pi (inorganic phosphate) (Antal et al., 2013). For extra flexibility in ATP and NADPH production, plants can utilize the cyclic electron transport (CET) (Figure 3). The CET allows to transport electrons from FDX back to the mobile carrier PQ, which transport the electron again to the cytochrome b_6/f complex where a proton is pumped into the thylakoid lumen. By reusing the electron by CET, the ATP production is increased while NADPH production decreases (Porcar-Castell et al., 2014). Several studies suggest that the energy partitioning between the photosystems by CET is a highly dynamic response to plant stress and environmental conditions (Eichelmann et al., 2005; Ivanov et al., 2001; Martin et al., 1978; Rumeau et al., 2007). Unfortunately, the seasonal and spatial dynamics of the energy partitioning by CET is still poorly understood (Porcar-Castell et al., 2014).

2.1.2. Dark reactions

During dark reactions, ATP and NADPH are used to fix CO_2 in the form of sugar. The dark reactions (or Calvin Cycle) consist of three phases: carbon fixation (carboxylation), reduction and regeneration (Figure 2 and Figure 4). In the carboxylation phase, CO_2 is fixed from an inorganic form into organic molecules. The enzyme ribulose biphosphate carboxylase (RuBisCO) catalyzes a reaction where ribulose biphosphate (RuBP) reacts with CO_2 and water to form two phosphoglycerate (PGA). In the reduction phase, two ATP and two NADPH are used to convert the two PGA to two phosphoglyceraldehyde (PGAL). In this process, each NADPH loses one electron and each ATP one phosphate, resulting in their conversion to ATP, NADP^+ . Both molecules are then reused and reenergized during the light reactions. Since only one out of six PGAL leaves the Calvin cycle, and two PGAL are formed in each turn, three turns of the cycle are needed in order to export one PGAL for plant growth, maintenance and reproduction. In the last phase of the Calvin cycle, the regeneration phase, the remaining five PGAL and tree additional ATP molecules are used to regenerate RuBP (Bonan, 2008; Lawlor, 2001). With decreasing water availability of the plant, the risk of photorespiration increases. Photorespiration describes a process where RuBisCO catalyses oxidation (uptake of O_2) instead of carboxylation (uptake of CO_2). The oxidized product can be partially recovered by releasing CO_2 which negatively affects the net ecosystem uptake of CO_2 (Porcar-Castell et al., 2014).

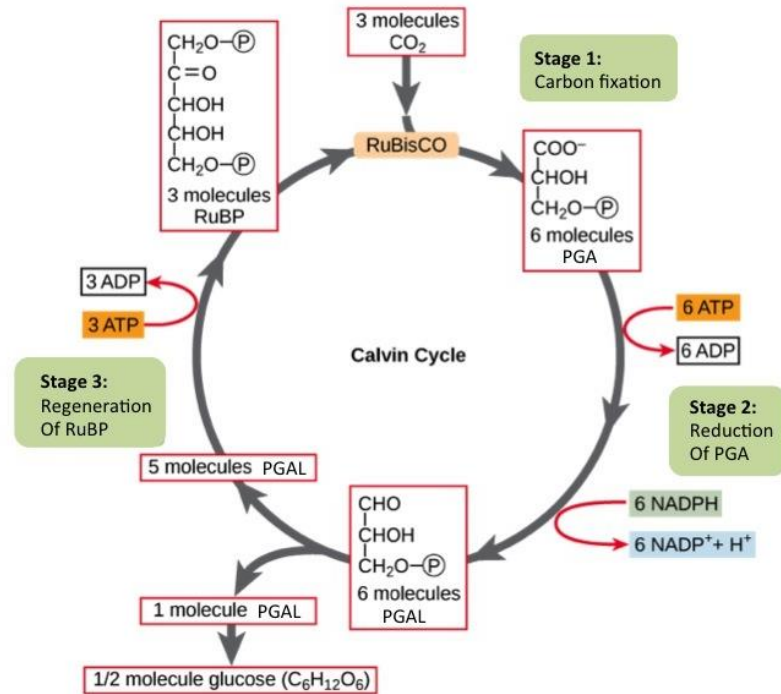


Figure 4: Dark reactions (Calvin Cycle). The Calvin cycle has three stages. In stage 1, the enzyme RuBisCO incorporates carbon dioxide into an organic molecule, 3-PGA. In stage 2, the organic molecule is reduced using electrons supplied by NADPH. In stage 3, RuBP, the molecule that starts the cycle, is regenerated so that the cycle can continue. Only one carbon dioxide molecule is incorporated at a time, so the cycle must be completed three times to produce a single three-carbon GA3P molecule, and six times to produce a six-carbon glucose molecule (OpenStax).

Source: Original by OpenStax modified by Robert A. Bear

2.1.3. Stomata conductance

Stomata are microscopic pores which regulate the uptake of CO₂ and the release of O₂ and H₂O by controlling the degree of opening and closing (Figure 5). Around 1% of a leaf area is covered by stomata. The stomata open to allow CO₂ uptake, which is needed by the photosynthesis process, and close to prevent desiccation during transpiration. Stomata conductance describes the rate of CO₂ entering and water vapor exiting the plant leaf, and is proportional to the maximum width of the stomata pores, where the upper limit of gas exchange is determined by the maximum stomata opening.

Stomata opening and closing is affected by various environmental conditions. With increasing sunlight more energy is generated by PSII and PSI, which results in higher CO₂ demand and a wide opening of the stomata. During night, the stomata close to prevent water loss (crassulacean acid metabolism (CAM) plants are an exception, but as they are not subject of this work, CAM plants will not be described here). When temperature is below or above the optimal value, stomata close. Another important

reason for stomata closure is an increase in the vapor pressure deficit. When the relative humidity of air decreases, a strong gradient in water vapor partial pressure between leaf and air creates a high potential for transpiration (Bonan, 2008). Water loss due to transpiration is closely related with high temperatures. When the loss of water cannot be counterbalanced by soil water uptake, the stomata close to prevent desiccation.

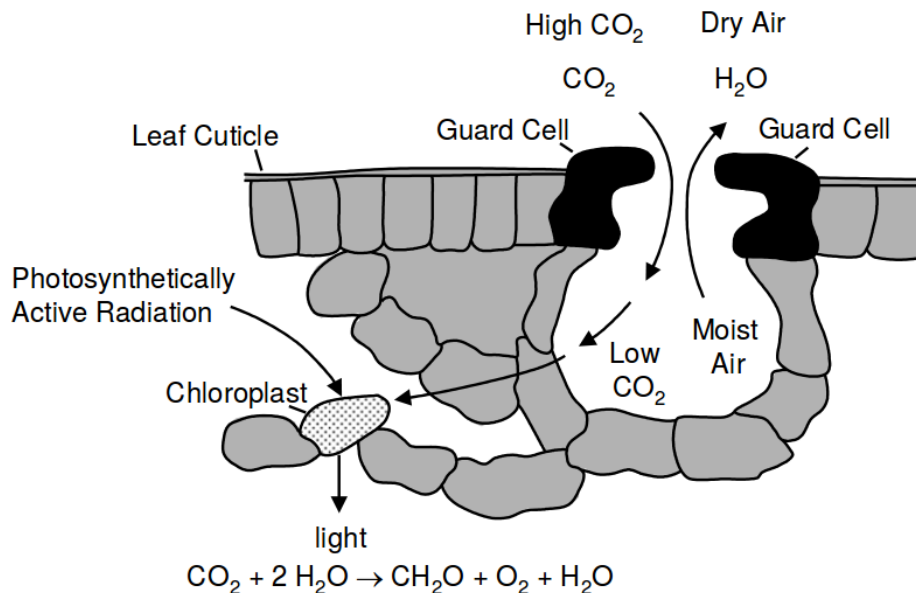


Figure 5: Stomatal gas exchange. When the stoma is open and a gradient of CO₂ between leaf and air exists, CO₂ enters the leaf and is assimilated in the chloroplast. To prevent dehydration, the stoma closes when a high gradient of H₂O between leaf and air takes place.

Source: modified after Bonan, 2008

2.1.4. Regulation mechanisms of photosynthesis

As described in the preceding chapters, the light and dark reactions are linked by the energy carriers NADPH and ATP and their depleted forms NADP⁺ and ADP, while CO₂ needed for the biomass production enters through the stomata. Because of different sensitivity to environmental conditions, the balance of the light and dark reactions does not always match. For example, closed stomata slow down the dark reactions due to the lack of CO₂, which leads to an excess supply of light within the photosystems. (Ensminger et al., 2006; Huner et al., 1996; Ögren and Öquist, 1984). When the photosystems absorb too much light energy, the photosynthetic machinery can be damaged. Damaged photosystems can recover overnight, except the plant faces other sustained environmental changes like drought or low temperatures. A severely

damaged photosystem needs from days to weeks to fully recover (Porcar-Castell et al., 2014). To prevent this damage, plants evolved regulatory mechanisms to control the energy balance between light and dark reactions (Demmig-Adams and Adams, 2006; Walters, 2005). A very effective protection mechanism is the reduction of chlorophyll pigments in the leaf, which results in a decreased light absorption. The relationship of absorbed light and chlorophyll content is not linear, since the increase of light absorption slows down with high values of chlorophyll content (Adams et al., 1990; Gitelson et al., 1998). Some species evolved protection strategies, where they increase the reflection of incoming light by changing canopy and leaf structure by adjusting leaf movement and angle (Arena et al., 2008), by leaf rolling (Kadioglu et al., 2012), by leaf pubescence (Ehleringer et al., 1976) or by changing the leaf epicuticular wax properties (Pfündel et al., 2008). In addition to the strategy of reflectance increase, plants can dissipate abundant light energy within the reaction center as heat (non-photochemical quenching; NPQ) or chlorophyll fluorescence (Figure 6).

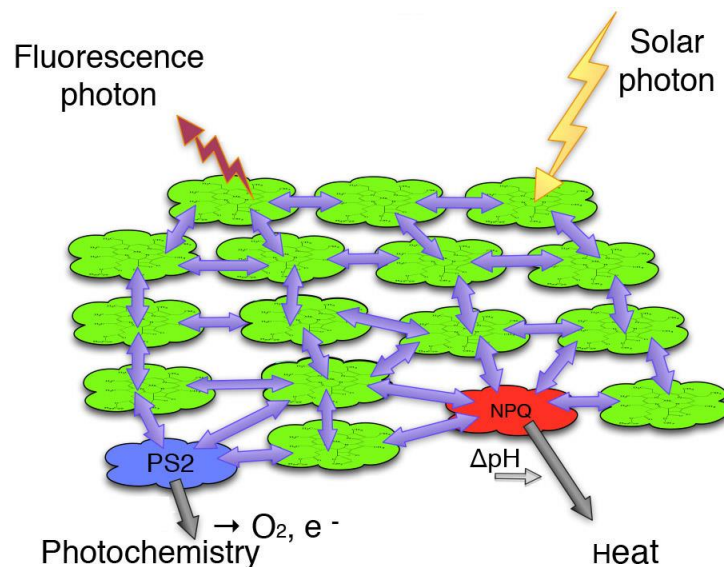


Figure 6: Concept of the light reaction center within the photosystem. Solar photons are captured by chloroplasts and transferred to light reaction centers where the absorbed photon (exciton) can be used in the photochemistry to assimilate CO₂, reemitted as fluorescence, or quenched by NPQ and released as heat.

Source: adapted from Frankenberg et al., 2013

2.1.5. Fluorescence and non-photochemical quenching

When light reaches the plant leaf, photons are reflected, absorbed or transmitted. The absorbed fraction of photons excite the chlorophyll *a* electrons to a higher energy state. At shorter wavelengths photon energy is higher and therefore excite the electrons to the energy level S₂. However, due to internal conversion the energy is rapidly lost as heat. Red photons excite electrons to energy state S₁ directly. From S₁ the electron can either relax to state S₀ as fluorescence emission, as non-radiative thermal dissipation

(NPQ), or used for photosynthetic energy transfer. It is important to note that due to the dynamic changes of NPQ, no unique relationship between fluorescence and energy used for photochemistry exists (Porcar-Castell et al., 2014).

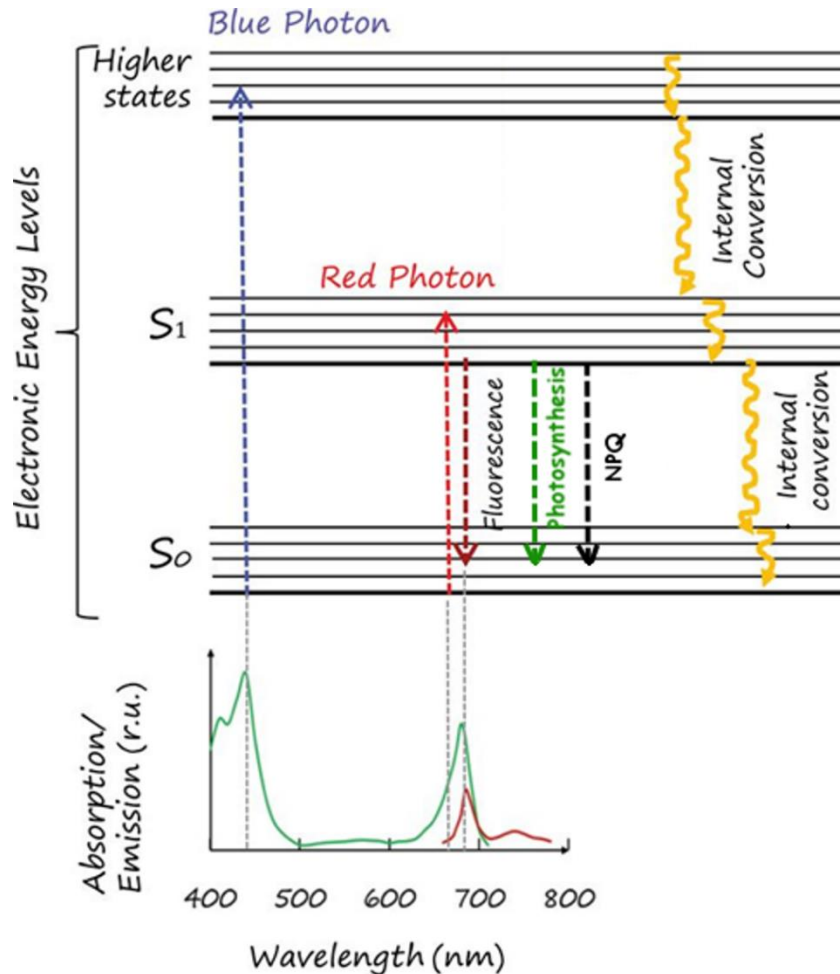


Figure 7: Jablonski diagram illustrating the energy partitioning of absorbed photons in a chlorophyll molecule. The absorption of blue light raises an electron from ground state (S_0) to higher energy states (S_2). The energy is rapidly dissipated as heat mainly by internal conversion to the first excited state (S_1). Absorption of red light produces the S_1 state directly. From the S_1 state electrons can relax to the ground state via emission of chlorophyll fluorescence photon, via non photochemical quenching (NPQ) and via photochemical quenching.

Source: adapted from Porcar-Castell et al. (2014)

The release of excessive energy as heat by NPQ is driven by two pH dependent mechanisms. When the electron transfer chain saturates, protons accumulate within the thylakoid lumen, which increases the electrochemical energy gradient and decreases the lumen pH. The protein PsbS reacts to photon increase or decrease by activating or deactivating NPQ, respectively. The second mechanism reacts to the decrease of pH

by de-epoxidation of xanthophyll cycle pigments, which results in an increase of NPQ. These two mechanisms operate on timescales of seconds to hours (Porcar-Castell et al., 2014; Verhoeven, 2014).

The activity of the xanthophyll cycle and the associated regulation of energy dissipation by NPQ generates an optical signal, which can be detected in the reflectance at around 531 nm. The photochemical reflectance index (PRI) exploits the changes in reflectance at 531 nm and a reference wavelength to assess LUE, due to its relationship to NPQ (Gamon et al., 1992). Several studies demonstrate the potential of PRI as a remote sensing proxy for LUE (Cheng et al., 2013; Damm et al., 2010a; Drolet et al., 2008; Rossini et al., 2010; Wu et al., 2010).

The F emission shows two peaks, the first peak is located in the red light (ca. 685 nm) the second peak in the far red light (ca. 740 nm). Since F contributes with a small fraction (ca. 1-5%) to the reflectance, these two signals must be separated from each other. The fluorescence peaks are located close to the atmospheric oxygen absorption bands B and A (687 nm and 760 nm respectively, Figure 8). Retrieval methods take advantage of this absorption features to decouple F from the total reflectance (Cogliati et al., 2015b; Meroni et al., 2009a) (c.f. Section 2.5).

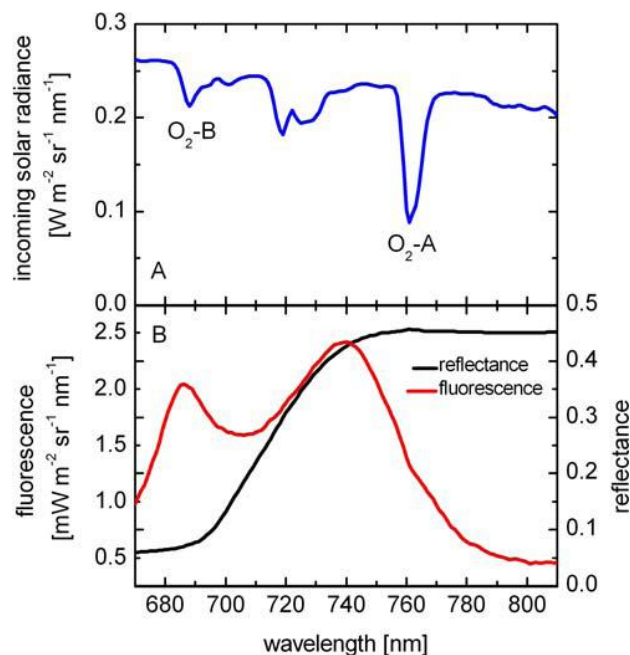


Figure 8: The upper part of the image shows the O_2B and O_2A absorption bands within the solar spectrum. The lower part of the image shows the spectral distribution of chlorophyll fluorescence emission and the reflectance of a winter wheat leaf.

Source: Schickling (2012)

2.2. Photosynthetic energy balance

Figure 9 shows a conceptualized description of the photosynthetic energy partitioning. Depending on leaf and canopy structure, only a fraction of incoming PAR is absorbed (APAR) by the plant. Absorbed photons can be reemitted as fluorescence (F_{tot}), released as heat (NPQ) or used for photochemical quenching (PQ). It is assumed that both photosystems are equally excited (PQ/2), whereby the energy available for the Calvin cycle is defined by the electron transport rate (ETR). The efficiency of the light reactions is defined as quantum use efficiency (QUE). The CO_2 assimilation rate (GPP) of the Calvin cycle depends on the stomata opening, the RuBisCO concentration and photorespiration.

The resource balancing paradigm by Field et al. (1995) hypothesizes that the plant's investment in the various resource-harvesting complexes is balanced and that plant growth can be sufficiently estimated by measuring only one growth-limiting factor. This factor is often termed as light use efficiency or LUE and can be calculated based on Eq. 1 as:

$$LUE = \frac{GPP}{APAR} \quad (2)$$

where now $\text{PAR} \cdot f_{\text{APAR}} = \text{APAR}$. While the local determination of plant specific LUE is relatively easy, the estimation of LUE on regional to global scale is problematic and connected with a high uncertainty (Running et al., 2004).

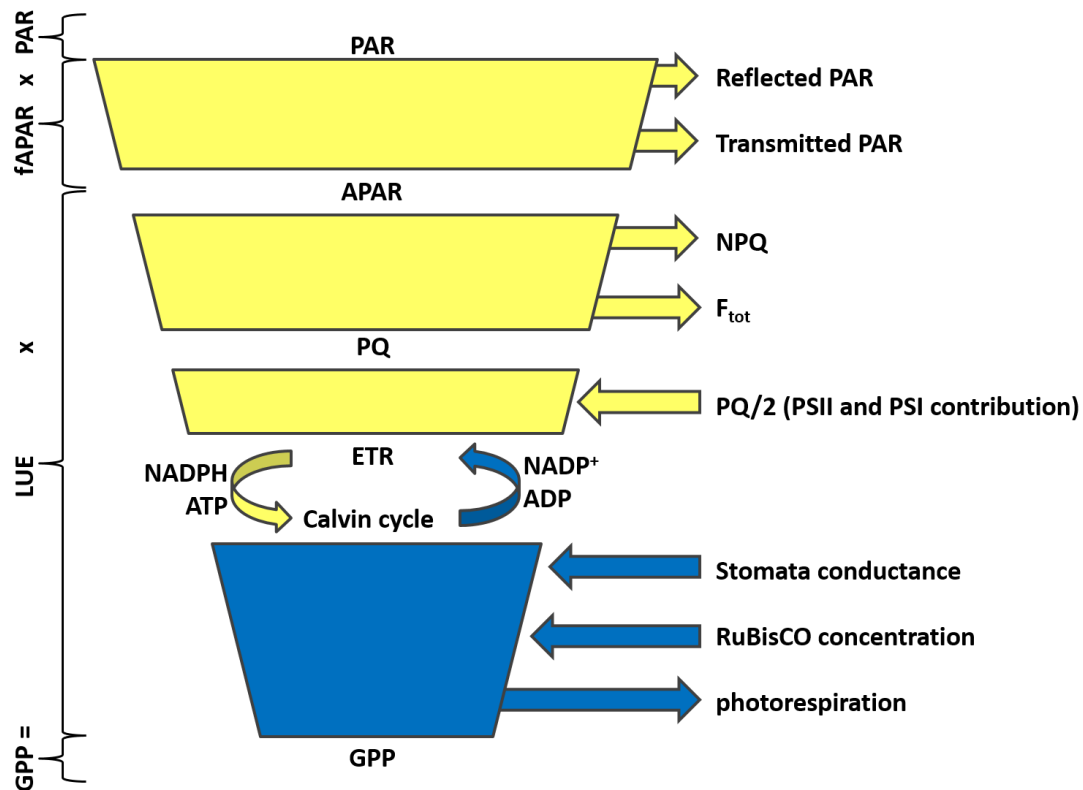


Figure 9: Photosynthesis energy balance scheme. The absolute amount of energy available for photosynthesis is APAR, which is defined on incoming PAR and canopy dependent fAPAR. APAR can be used to produce photochemical energy (photochemical quenching; PQ), or released as heat (non-photochemical quenching; NPQ) or fluorescence (F_{tot}). The electron transport rate (ETR) provides energy for the regeneration of NADP⁺ and ADP. The CO₂ assimilation efficiency by the Calvin cycle depends on the stomata conductance, the RuBisCO concentration and photorespiration.

2.3. Measuring photosynthetic activity on the leaf level

The most direct measurement of photosynthesis can be achieved by the combined use of an infrared gas analyzer and a pulse-amplitude modulation (PAM) fluorometer. The infrared gas analyzer measures the uptake of CO₂ and the release of H₂O by the leaf. By using a mass balance approach, the CO₂ assimilation and transpiration can be calculated. By additional measurement of leaf temperature, other important parameters like stomata conductance and intercellular CO₂ concentration can be calculated. The PAM fluorometer measures fluorescence yield (ϕ_F) which provides information about the quantum yield of photosystem II (ϕ_{PSII}) and electron transport rate (ETR). Since these measurements can only be obtained on leaf level, these measurements are difficult to relate to F (Cendrero-Mateo et al., 2016). Therefore, no leaf level measurements were conducted as part of this thesis.

2.4. Measurements of photosynthetic activity on the canopy level

2.4.1. Eddy covariance measurements

The exchange of matter (CO₂ and H₂O) and energy (latent- and sensible heat) between land surface and atmosphere is mainly driven by small scale turbulence caused by surface roughness induced wind shear or thermal convection. Depending on surface characteristics and atmospheric layering, the size of these turbulent eddies can range from millimeter to hundreds of meters, with their maximum height limited by the boundary layer height (Stull, 1988). The eddy covariance (EC) method measures these turbulent fluctuations (often referenced as eddies) with a high frequency of 10 to 20 Hz to determine vertical fluxes of heat, water vapor and gases. The equation for determining the fluxes are derived by simplification of the Navier-Stokes equation using the Reynolds' decomposition (Foken, 2006; Stull, 1988). The Reynolds decomposition postulates that a quantity x can be described as the sum of its mean \bar{x} and the fluctuation around its average x' :

$$x = \bar{x} + x' \quad (3)$$

With the assumption that the density fluctuation and the mean vertical flow are negligible for horizontal homogenous terrain, the net ecosystem exchange of CO₂ (NEE, in $\mu\text{mol m}^{-2} \text{s}^{-1}$) can be calculated by the determination of its covariance with the vertical wind velocity w , if CO₂ and w are measured at the same point in time and space.

$$NEE = \frac{\rho_a}{m} \cdot \overline{w' \cdot [CO_2]'} \quad (4)$$

Where ρ_a is the dry air density [kg m^{-3}], m the molar mass of CO₂ [44.01 g mol^{-1}], w the vertical wind velocity [m s^{-1}] and $[CO_2]'$ the mixing ratio of CO₂ [ppm].

In the last decade the EC method became the main technique for estimating energy and mass fluxes within an ecosystem (Baldocchi et al., 2001). With a integration time of half an hour, a temporal coverage of several years and the availability of EC measurements for different ecosystems (FLUXNET; <https://fluxnet.ornl.gov/>), EC data serves as a backbone for bottom-up estimates of continental carbon balance components (Jung et al., 2011; Papale and Valentini, 2003) and is increasingly used for land surface model parameterization and validation (Reichstein et al., 2005). EC measurements, conducted at 2 meter above canopy, cover footprints of several hundred meters and, therefore, only provide spatially discrete information about the ecosystem. Furthermore EC measurements are strongly affected by the local setup, meteorological

conditions and aerodynamic properties of the ecosystem (Baldocchi, 2008; Baldocchi et al., 2001). For instance, a sufficient large and homogenous footprint, a relatively flat land surface and turbulent conditions are needed to obtain measurements with lowest uncertainty. The uncertainty fluctuates between 5-10% respective to the environmental conditions (Foken, 2006). It is important to note that the EC method only provides NEE, which is defined as:

$$NEE = GPP - R_{plant} - R_{soil} \quad (5)$$

Where R_{plant} is the respiration by the vegetation and R_{soil} the respiration by the soil. For the calculation of GPP, R_{plant} and R_{soil} have to be known. By using the short-term temperature sensitivity of R_{plant} and R_{soil} and night time measurements ($GPP = 0$), measurement gaps can be filled and NEE separated into GPP and R_{eco} ($R_{plants} + R_{soil}$) (Reichstein et al., 2005).

2.4.2. Chamber measurements

The first practical chamber for measuring CO_2 exchange was described half a century ago by Lange (1962). Since then, the method was debated and further improved. Gas exchange chamber systems use enclosure methods, where several plants are enclosed in a transparent chamber for a short time (1-2 min). The transparency for solar radiation allows the plants to be photosynthetically active when the chamber is moved over the canopy. A ventilation system circulates the air within the chamber and allows an infrared gas analyzer to measure the changing CO_2 and H_2O concentration. The canopy net exchange of CO_2 (NEE) and evapotranspiration (ER) can be calculated from the gas exchange rates on a mass basis, the chamber volume and soil area (Livingston and Hutchinson, 1995; Reicosky, 1990). Chamber measurement systems are portable between locations, cheap, easy to operate, and still provide the only approach to measure heterogeneity of canopy gas-exchange within a field (Langensiepen et al., 2012; Livingston and Hutchinson, 1995; Steduto et al., 2002). A point of criticism against closed chamber measurements is that the microclimate within a chamber is altered during the sampling period, resulting in a distortion of the estimated CO_2 and H_2O exchange rates (Garcia et al., 1990; Burkart et al., 2007). Like the EC method, GEC (Gas-Exchange Chamber) usually only provide NEE. Since, GEC chambers normally do not measure during night, a flux partitioning like EC data is not feasible. To overcome this problem, dark chambers can be used to block the plant photosynthesis process by using non transparent material for the chambers. Resulting measurements of ecosystem respiration (R_{eco}) can then be subtracted from NEE to calculate GPP.

2.4.3. Remote sensing of sun induced chlorophyll fluorescence

The direct link of fluorescence to the photosynthetic process opens new perspectives in accessing photosynthesis at ecosystem scale (Damm et al., 2015; Frankenberg et al., 2011; Guanter et al., 2014; Wieneke et al., 2016). F is a very weak signal on top of the reflected sun light (1-5%), but advances in sensor and retrieval methodology allow the disentanglement of F and the apparent reflectance by using terrestrial and solar absorption lines (Meroni et al., 2009a). With a signal to noise ratio < 1000 the retrieval of F_{760} in the O₂A band is possible with a FWHM resolution of ca. 3nm, while the retrieval of F_{687} in the O₂B band requires a FWHM of at least 1nm (Damm et al., 2011). Recent advances in sensor technology and retrieval methods allow now the passive measurement of sun induced chlorophyll fluorescence using ground (Burkart et al., 2015; Cogliati et al., 2015a; Damm et al., 2010a), airborne (Damm et al., 2010b, 2014; Rossini et al., 2015; Rascher et al., 2015), and satellite sensors (Frankenberg et al., 2014; Guanter et al., 2012; Joiner et al., 2011). With the selection of FLEX as an Earth Explorer 8 mission, it is expected that in the next few years the availability, quality and spatiotemporal coverage of ground and airborne measurements will increase drastically. In-situ and airborne measurements are needed to: 1. improve our knowledge of the relationship between F and GPP; and 2. as calibration and validation for the FLEX satellite mission (Porcar-Castell et al., 2014; Rascher et al., 2015).

2.5. Retrieval of sun induced chlorophyll fluorescence

RS sensors developed for F estimation measure the incoming solar radiation, irradiance (I , in $W\ sr^{-1}\ m^{-2}\ nm^{-1}$), and the outgoing radiation, radiance (L , in $W\ sr^{-1}\ m^{-2}\ nm^{-1}$), with high spectral resolution. The relation of L to I describes the percentage of light reflected by the surface; reflectance (R , in %).

$$R = \frac{L}{I} \quad (6)$$

The upwelling radiance signal received at an RS sensor (\tilde{L}) comprises of two radiant fluxes: sunlight reflected by the surface (L) and the emitted F.

$$\tilde{L} = R \cdot I + F \quad (7)$$

Therefore, only an apparent radiance (\tilde{L}) can be measured and, thus, only an apparent reflectance (\tilde{R}) can be calculated. The Fraunhofer absorption lines can be utilized to disentangle F from R. Fraunhofer lines are dark features in the visible spectrum of the

sun, which are caused by the absorption of light by certain elements in a specific wavelength (Joiner et al., 2011).

All F retrieval methods base on the Fraunhofer line depth (FLD) method, developed 40 years ago by Plascyk (Plascyk, 1975; Plascyk and Gabriel, 1975). The FLD method allows the estimation of F by measuring L and I inside and outside the Fraunhofer absorption lines, or at strong terrestrial atmospheric absorption bands like the O₂ A- and B-band (760 and 687 nm respectively). In the following four commonly used retrieval methods are described.

2.5.1. Fraunhofer line depth (FLD) method

The FLD method assumes that the wavelength (λ) with highest absorption inside the absorption band (λ_{in}) and the reference wavelength outside the absorption band (λ_{out}) are close enough to each other to consider \tilde{R} and F as constant:

$$\tilde{R}_{in} = \tilde{R}_{out} ; F_{in} = F_{out} \quad (8)$$

Based on this assumption and Eq. 7, F can be expressed as:

$$F_{FLD} = \frac{I_{out} \cdot L_{in} - L_{out} \cdot I_{in}}{I_{out} - I_{in}} \quad (9)$$

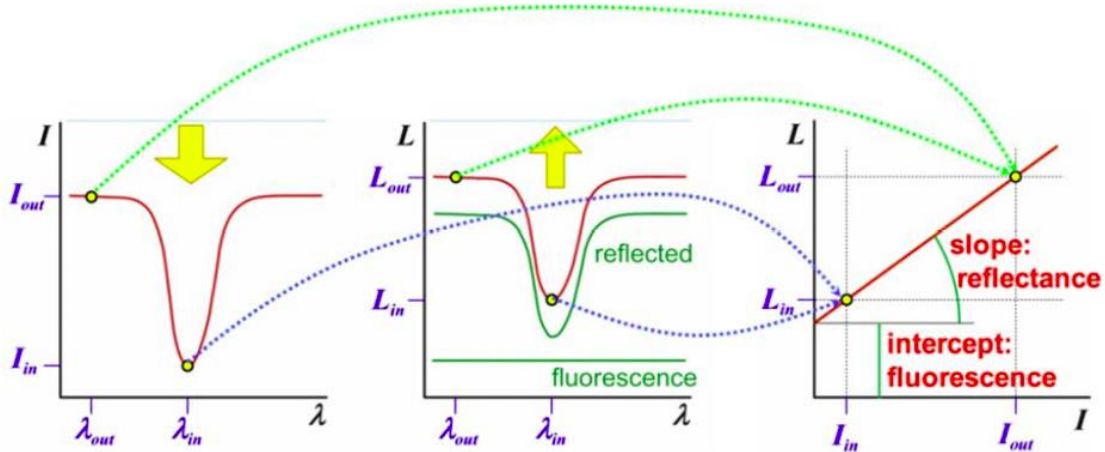


Figure 10: Principle of the FLD sun induced chlorophyll fluorescence retrieval. In the left figure the red curve symbolize the irradiance. In the middle figure the red curve symbolizes the upwelling radiance, the green curve the reflectance and the green line the fluorescence. The right Figure shows that the irradiance (I) outside and inside of the absorption band is linearly related to the radiance (L) outside and inside the absorption band. The offset of this linear relationship is the fluorescence.

Source: Rascher et al. (2015)

The FLD method is easy to use and only requires radiance measurement outside and inside of the absorption band. The main criticism against this method is the assumption that \tilde{R} and F are constant over this wavelength range which has been questioned by several studies (Alonso et al., 2008; Meroni et al., 2010; Meroni and Colombo, 2006; Moya et al., 2004).

2.5.2. Three channel Fraunhofer line depth (3FLD) method

Maier et al. (2003) proposed the use of three spectral channels to solve Eq. 9 to overcome the limitations of the FLD assumption. Instead of using a single reference channel on the left shoulder of the absorption band, a second reference channel on the right shoulder is used to calculate the average of both reference channels. By using three channels instead of two, this method assumes that \tilde{R} and F vary linearly in the considered spectral range. The 3FLD method provides an improved estimate of fluorescence in the O₂A band, but is considered to perform poorly within the O₂B band. Since the left and right shoulder of the O₂B absorption band are located far from each other, the assumption of a linear relationship between \tilde{R} and F seems to be underdetermined (Alonso et al., 2008; Meroni et al., 2009a).

2.5.3. Improved Fraunhofer line depth (iFLD) method

Based on the FLD method, Alonso et al. (2008) developed the improved Fraunhofer line depth method. The iFLD method enhanced estimations of F by incorporating correction coefficients which improve the description of reflectance and fluorescence spectral characteristics. Alonso et al. (2008) pointed out that the assumption of Eq. 8 is not valid, which results in an overestimation of the F signal. Within the absorption band, I and L decrease proportionally to each other. On the contrary, F does not decrease proportionally with I , which results in a stronger \tilde{L} (cf. Eq. 7) and, therefore, an increase of \tilde{R} within the absorption band (cf. Figure 11 blue dashed line).

$$\tilde{R} = \frac{\tilde{L}}{I} \quad (10)$$

In order to correct for the false FLD assumption of Eq. 8, the correction coefficients α_R and α_F have to be defined:

$$\tilde{R}_{out} = \alpha_R \cdot \tilde{R}_{in}; F_{out} = \alpha_F \cdot F_{in} \quad (11)$$

Since these coefficients can vary widely from one case to another (e.g. due to changes in the canopy structure), the correction coefficients are not static and can therefore not be defined generally. Figure 11 shows that the real reflectance (without F) is smooth

(black line), while the apparent reflectance shows a bump (blue dashed line) due to the relatively stronger fluorescence signal within the absorption band. The correction coefficients can now be calculated by interpolating across the absorption band. Polynomial splines of fourth order showed best interpolation results (red dashed line) (Alonso et al., 2008). Then:

$$\alpha_R = \frac{\tilde{R}_{out}}{\hat{R}_{in}} \quad (12)$$

where \hat{R}_{in} is the interpolated apparent reflectance within the absorption band. The F correction coefficient is calculated as:

$$\alpha_F = \frac{I_{out}}{\hat{I}_{in}} \cdot \alpha_R \quad (13)$$

where \hat{I}_{in} is the interpolated irradiance within the absorption band. F can now be derived as:

$$F_{iFLD} = \frac{\alpha_R \cdot I_{out} \cdot L_{in} - L_{out} \cdot I_{in}}{\alpha_R \cdot I_{out} - \alpha_F \cdot I_{in}} \quad (14)$$

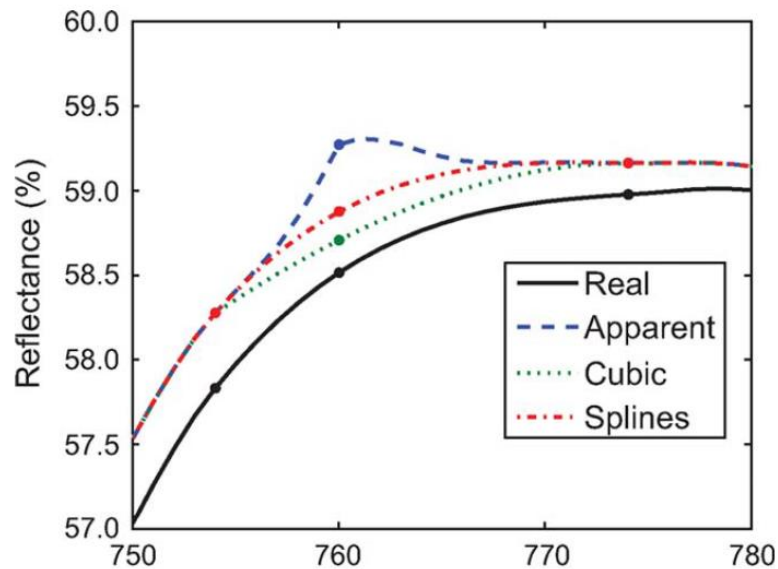


Figure 11: Concept of the iFLD method. The real reflectance (black line) cannot be measured because of the additive signal of fluorescence (blue dashed line). The bump in the fluorescence is caused by the O₂A absorption band. To correct for this bump cubic (green dotted line) or polynomial splines (red dot-dashed line) can be used. The difference between apparent reflectance and real reflectance is the fluorescence.

Source: Alonso et al. (2008)

2.5.4. Spectral fitting method (SFM and SpecFit)

Spectral fitting methods (SFM) determine the true reflectance (R) and F by adjusting mathematical functions, to describe the spectral behavior of F and R within a defined spectral window. The mathematical functions for F and R are parameterized by a least square nonlinear curve-fitting optimization technique that minimizes a cost function (Cogliati et al., 2015b; Meroni et al., 2010; Meroni and Colombo, 2006). Cogliati et al. (2015b) compared 54 different combinations of mathematical functions to describe F and R close to the O₂ absorption bands. They found that a combination of piecewise cubic spline and Voigt spectral functions provide high accuracy in the O₂A and O₂B bands. Due to their strong absorption features, the spectral fitting window of the SFM algorithms normally focus on the retrieval of F in the range of the O₂ bands. In this range, F shows a higher contribution to total radiance and is therefore less affected by instrumental noise.

Based on the SFM method Cogliati et al. (2015b) presented a new approach (SpecFit) to extend the spectral fitting window to the whole spectral region where fluorescence emission occurs (670-780 nm). Even though the idea underlying the SpecFit algorithm is the same than for the SFM, the mathematical functions used to predict total fluorescence and reflectance are more complex. While the reflectance signature in the red to far-red spectral region can be reproduced by the piecewise cubic spline, the red and far-red F emission peaks have to be estimated from different combinations of Gaussian, Lorentzian, and Voigt profiles (Cogliati et al., 2015b). Results showed that the performance of the SpecFit retrieval is comparable to those obtained with the SFM method. However, the possibility of retrieving the full spectrum of fluorescence opens new perspectives for further investigation of plant species and traits, plant reactions to changing environmental conditions and photosynthetic rates (Cogliati et al., 2015b). The downside of the SFM and SpecFit retrieval is that both require datasets with a minimum spectral resolution of 0.3 nm FWHM (full width at half maximum), which is still technically challenging.

2.6. Modeling approaches for estimating GPP using remotely sensed F

2.6.1. Simple linear scaling approach

One of the first approaches to estimate GPP from F was proposed by Frankenberg et al. (2011). It was shown that spatial and temporal patterns of satellite derived F strongly correlate linearly with GPP derived from EC-upscaling methods (Jung et al., 2011), satellite reflectance data (Zhao and Running, 2010) and climatology model data (Van Der Werf et al., 2003). In this approach, GPP can therefore be estimated as:

$$GPP = a + F \cdot b \quad [\mu\text{mol CO}_2 \text{ m}^{-2} \text{ s}^{-1}] \quad (15)$$

where a and b are the statistically derived offset and slope, respectively. Even though GPP and F are mainly driven by APAR, it is assumed that the F signal also contains information about the plant status. The problematic aspect of this assumption is that the satellite data (GOSAT, GOME-2) provides a spatial (0.5° footprint) and temporally (monthly) coarse mixed signal. This raises doubts about how much information about the plant status the GOSAT derived F really provides (Yang et al., 2015).

2.6.2. Semi-mechanistic approach

Guanter et al. (2014) recently proposed a new approach, which does not assume a linear relationship of F with GPP but is based on the relationship of APAR independent LUE and F_{yield} . GPP can therefore be expressed as:

$$GPP = F \cdot \frac{LUE}{F_{\text{yield}}} \quad (16)$$

Where the LUE is calculated from Eq. 2 and F_{yield} as:

$$F_{\text{yield}} = \frac{F}{PAR \cdot f_{APAR}} \quad (17)$$

Due to the lack of long-term field measurements, the inter- and intra-daily (i.e. between days and within a day, respectively) relationship between LUE and F_{yield} is still unclear. Yoshida et al. (2015) compared the relationship of modeled LUE with satellite derived F_{yield} (GOME) and found that under moderate light conditions in the morning, LUE and F_{yield} show a constant ratio. Since these findings are based on spatiotemporal averaged satellite derived F_{yield} and modeled LUE, these findings need to be confirmed by field measurements.

2.6.3. Using process based models

The radiative transfer and energy balance model SCOPE (Soil Canopy Observation, Photochemistry and Energy fluxes) simulates photosynthesis, fluorescence and NPQ (van der Tol et al., 2009). SCOPE became recently an important tool in F-photosynthesis studies (Damm et al., 2015; Verrelst et al., 2016; Zhang et al., 2014). Remotely sensed F can be used to parameterize SCOPE for an improved estimate of GPP, but the use of F as an input parameter is still not possible. Additionally, SCOPE has to be driven by forcing data (e.g. chlorophyll content, maximum rate of carboxylation, LAI) which are especially difficult to obtain for larger simulation areas. Furthermore, SCOPE is computationally expensive, which makes it unfeasible for global or continental simulations with higher resolution.

In another approach, process based dynamic global vegetation models (DGVMs) are used as data integration platform fluorescence observations. Parazoo et al. (2014) for example, used observations of satellite fluorescence to constrain photosynthesis estimated by an ensemble of DGVM simulations. In another approach, Lee et al. (2015) incorporated the estimation of fluorescence into the community land surface model 4.5 (CLM4.5) by assuming an empirical relationship between the relative light saturation of photosynthesis and NPQ (van der Tol et al., 2014). Remotely sensed F can then be used as an observational constrain for the CLM. Zhang et al. (2014) show that F can also be used as an estimator for DGVM sensitive parameters like the V_{cmax} , which can lead to an improved estimation of GPP by of land surface models.

Nevertheless, all of these approaches are based on empirical assumptions derived from either leaf level actively measured fluorescence or satellite derived F with coarse spatiotemporal resolution. Since long-term measurements of F in combination with simultaneous CO₂ flux measurement are rare, a characterization of the relationships between F_{tot} , NPQ, and PQ is still problematic, and a mechanistically link between F and GPP not yet possible.

2.7. Fluorescence as an estimator of plant stress

A recent meta-analysis by (Ač et al., 2015) collected 73 peer reviewed articles investigating the link between water, temperature or nutrient stress and their effect on passive and active measured leaf and canopy fluorescence. Their results suggest that water stress is associated with a decrease of red and far-red fluorescence, while the fluorescence ratio provided inconsistent results. Chilling significantly increased red and far-red fluorescence, whereas heat showed a decrease in both fluorescence peaks and in the fluorescence ratio. Nitrogen deficit decreased far-red fluorescence, which results in an increase in the fluorescence ratio. It is important to note that only five of

the reviewed articles dealt with passive canopy measurements of far-red sun induced fluorescence (F_{760}) and only one with red sun induced fluorescence (F_{687}). This means that our current knowledge of the link between fluorescence and stress is mostly based on active leaf level measurements (Ač et al., 2015; Porcar-Castell et al., 2014).

The most commonly used technique to measure active leaf level chlorophyll fluorescence is the pulse amplitude modulated (PAM) fluorometry (Genty et al., 1989; Schreiber, 2004), where a saturating light pulse is used to characterize the fluorescence quenching mechanisms and to determine the quantum use efficiency of PSII (ϕ PSII) (c.f. Section 2.3). A detailed description of this method can be found in Schreiber (2004). From active leaf level measurements, it is known that PSII and PSI differ in their contribution to the total fluorescence spectra (Buschmann, 2007; Franck et al., 2002). The contribution of PSI fluorescence fluctuates between 0 and 50% depending on environmental conditions, species and spectral region. While the contribution of PSI in the red region is lowest, the maximum is located in the near infrared. Thus, the shape of the fluorescence spectra contains information about the photosystem activity (Agati et al., 2000; Dau, 1994; Franck et al., 2002; Genty et al., 1990; Peterson et al., 2001; Pfündel, 1998), and consequently about plant stress (c.f. Section 2.1.4).

While active leaf level measurements helped understanding the link between stress and fluorescence, results cannot be easily transferred to passive canopy measurements (Cendrero-Mateo et al., 2016). The relationship of PSII and PSI contribution to total sun induced canopy fluorescence can be influenced by three different mechanisms.

- 1) Changes in the chlorophyll concentration affect the reabsorption of F_{687} . A decrease of the chlorophyll content results in lower reabsorption of red light, and consequently in an increase of the PSII fluorescence signal (F_{687}). It is known that net changes of leaf chlorophyll content happen at time scales of days (García-Plazaola and Becerril, 2001; Lu et al., 2001).
- 2) Seasonal changes of the PSII and PSI absorption spectra could equally affect the contribution of the photosystems to the fluorescence signal.
- 3) Under the assumption that sustained forms of NPQ do not operate in a similar fashion in both photosystems and that the photosystems are deeply down-regulated due to stress conditions, the contribution of PSI fluorescence to the total fluorescence would dramatically increase (Porcar-Castell et al., 2014).

Due to the lack of long term passive canopy measurements of red and far-red chlorophyll fluorescence, the diurnal and seasonal dynamics of the PSI and PSII contribution are still unclear (Ač et al., 2015; Porcar-Castell et al., 2014). In particular, the third mechanism remains controversial.

3. Observations

3.1. Study area (TR32)

The TR32 project intense study area is located in the catchment of the Rur, a river in the central western part of North Rhine-Westphalia, Germany (Figure 12 A&B). The local climate is characterized by an annual mean temperature of 11°C and an annual mean precipitation of around 700mm/year (LANUV NRW, 2014). The region is dominated by agriculture. The dominant crop type is sugar beet followed by maize, rapeseed, and potato. Two measurement campaigns were performed as part of this work. Both with the focus on sugar beet. The first measurement campaign was carried out in 2012 close to the village of Selhausen, the second in 2015 close to the village of Merzenhausen. The focus of the first measurement campaign was to explore the spatiotemporal relationship of GPP to F in the course of one day, while the second in-situ campaign aimed at studying the temporal relationship between GPP and F during a growing season.

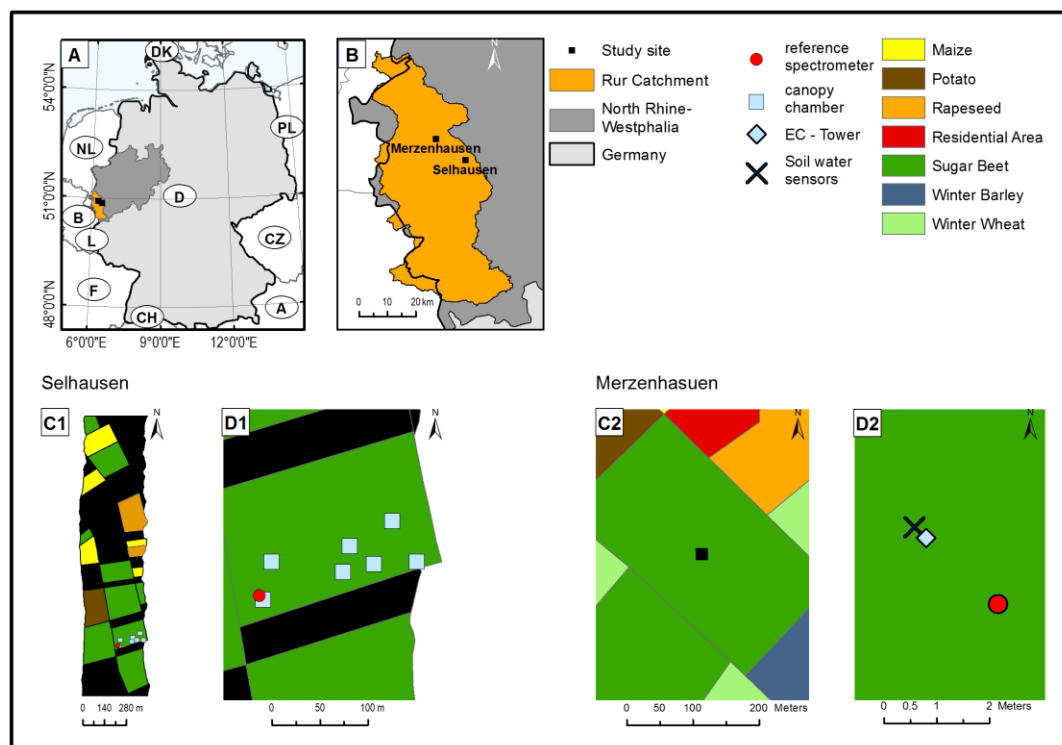


Figure 12: Study area location within Germany (A), the catchment area of the river Rur (B), land use classification of the Selhausen flight line (C1, 50.8612 N / 6.4539 E), position of the MSS reference spectrometer and the net ecosystem exchange canopy chambers in Selhausen (D1), land use classification of the Merzenhausen site (C2, 50.9297 N / 6.2969 E), position of the SIF-Sys spectrometer (red dot), the Eddy Covariance Tower and the soil water sensors in the Merzenhausen sugar beet field (D2).

3.2. Selhausen campaign 2012

The experimental site of the first measurement campaign was located close to the village of Selhausen (50.864N, 6.452E, altitude 103 m above sea level). It covers 1.4ha (200m x 70m) with a gentle slope of 4° in east-west direction. The upper part of the field is more gravelly than the lower part, resulting in a lower water-holding capacity in that area (Rudolph et al., 2015; Stadler et al., 2015). In 2012 the field was cultivated with sugar beet, which grew from March (day of year (DOY): 87) to September (DOY: 254). Ground measurements were carried out in sugar beet field G (Figure 12C) with fully developed leaves and a fractional cover of 90% (BBCH-Code: 39 – the Biologische Bundesanstalt, Bundessortenamt und Chemische Industrie (BBCH) code describes the phenological status of a plant. BBCH-Code: 39 indicate that the Rosette growth is completed and that leaves cover 90% of the ground). Imaging spectroscopy data were acquired with the *HyPlant* sensor on August 23, 2012 (DOY: 236). The observation took place under clear sky conditions. A rain event with a precipitation sum of 0.12 mm was recorded one day before the airborne data acquisition, and the maximum air temperature was 23°C. Sunrise was at 4:32 a.m., solar noon at 11:35 a.m. and sunset at 6:36 p.m. UTC (Coordinated Universal Time).

3.2.1. Field spectroscopy

During the 2012 flight campaign, the custom-made measurement setup Manual Spectrometric System (MSS) was used to continuously measure irradiance and surface-leaving radiance to eventually derive F emissions at 760 nm (F_{760}), as well as the absorbed photosynthetic active radiation ($APAR_{MSS}$) in the field. The spectrometer system was designed for high-temporal frequency sampling of radiometric measurements. Briefly, top of canopy radiances were measured using two portable spectrometers (HR4000, OceanOptics, USA) characterized by different spectral resolutions. The first instrument covered the visible and near-infrared range (400 nm to 1000 nm) with a full width at half maximum (FWHM) of 1 nm, facilitating the computation of different VIs. The second instrument covered a restricted spectral range (700 nm to 800 nm) with a finer spectral resolution (full width at half maximum; FWHM = 0.1 nm) and was specifically intended for F_{760} measurements in the oxygen absorption band O2-A. Both spectrometers were housed in a Peltier thermally regulated box (model NT-16, Magapor, Zaragoza, Spain), keeping the internal temperature at 25°C to reduce dark current drifts. Both spectrometers were spectrally and radiometrically calibrated with known standards (CAL-2000 mercury argon lamp and LS-1-CAL calibrated tungsten halogen lamp, OceanOptics, USA). The instrument's fiber optics were mounted on a horizontal rotating arm to observe alternately the canopy and a calibrated white reference panel (Labsphere, Inc., USA) and thus to measure surface irradiance. The MSS was installed on a fixed position (Figure 12D)

but the 1.5 m radial-arm was sequentially (ca. 1-3 minutes) placed over three positions and observations were averaged to cover potential field heterogeneity. Measurements started at 8:35 a.m. and finished at 4:10 p.m. UTC.

F_{760} emissions were retrieved using the spectral fitting method (described in Section 2.5.4, (Meroni et al., 2010)), assuming a linear variation of reflectance and fluorescence in the O_2 -A absorption band region (759.0 nm to 767.7 nm) (c.f. Section 2.5.4). Resulting F values are hereafter named $F_{760,MSS}$. $APAR_{MSS}$ was derived from measured radiances as the difference between incident and reflected radiance, integrated over the spectral region from 400 nm to 700 nm (Damm et al., 2010a). F_{yield} is the fluorescence use efficiency, indicating the fraction of photons that are re-emitted from the absorbed photons. We calculated $F_{760yield}$ from MSS measurements as:

$$F_{760yieldMSS} = \frac{F_{760MSS}}{APAR_{MSS}} \quad (18)$$

3.2.2. Canopy gas-exchange chambers and leaf area index

Seven connector frames at different positions were permanently installed within a sugar beet field (Figure 12D). The chamber comprised a 50cm height adapter and a 30cm height chamber top. The chamber top was equipped with a LI-COR 6400 XT IRGA (LI-COR, Lincoln Nebraska, USA) gas analyzer and was moved between the connector frames during the flight campaign to measure NEE_{CC} ($\mu\text{mol CO}_2 \text{ m}^{-2} \text{ s}^{-1}$) and PAR_{CC} ($\mu\text{mol m}^{-2} \text{ s}^{-1}$). Soil respiration ($R_{soil,CC}$, $\mu\text{mol CO}_2 \text{ m}^{-2} \text{ s}^{-1}$) was measured using a LI-8100 (LI-COR, Lincoln Nebraska, USA) soil gas analyzer within the connector frames. The measurements started around 8:10 a.m. and ended at 3:00 p.m. UTC, resulting in five measurements per chamber position. The partitioning of NEE_{CC} in GPP_{CC} and respiration fluxes can be expressed as:

$$GPP_{CC} = -NEE_{CC} + (R_{soil,CC} + R_{plant,CC}) \quad (19)$$

Since no dark chamber measurements were available, $R_{plant,CC}$ could not be obtained directly from the chamber measurements. To estimate $R_{plant,CC}$ we used measurements of an nearby EC tower positioned in a sugar beet field at the same growing stage. Assuming that field mean $R_{CC,soil}$ and $R_{EC,soil}$ are not significantly different, $R_{plant,CC}$ was calculated as:

$$R_{EC,plant} \approx R_{EC,ecosystem} - R_{CC,soil} \quad (20)$$

And:

$$R_{CC,plant} \approx \frac{R_{EC,plant}}{NEE_{EC}} \cdot NEE_{CC} \quad (21)$$

For the flux partitioning of the NEE_{EC} , the online processing tool based on Reichstein et al. (2005) was used. Because the measurement intervals were irregular, observation times were harmonized by linearly interpolating chamber data. To ensure that the chamber measurements were not significantly distorted due to microclimate alteration within the chamber, we correlated GPP_{CC} with the destructively-measured leaf area index (LAI). The LAI measurements were conducted on the day of flyovers with a leaf area meter LI-3100C (LI-COR Bioscience, Lincoln, Nebraska) at the position of the canopy chambers (Figure 12D). The significant positive relationship ($r^2 = 0.84$) between derived GPP_{CC} and measured LAI indicates that the chamber measurements captured the infield variability of GPP well. To account for measurement and interpolation errors due to the lack of $R_{CC,plant}$, we assume an uncertainty of 10% (Graf et al., 2013; Wang et al., 2013).

To calculate LUE_{CC} from chamber measurements, APAR needs to be known. PAR was measured by the individual canopy chambers and fAPAR was modeled using the radiative transfer model SCOPE version 1.51 (van der Tol et al., 2009), parameterized with *in-situ* measured LAI and half-hourly atmospheric data obtained from a nearby meteorological station. We applied an average chlorophyll *a* and *b* concentration of 80 mg cm⁻² and a maximum carboxylation rate (V_{cmax}) of 80 μmol m⁻² s⁻¹. The Ball Berry stomatal conductance parameter was set to 10 and the vegetation height was set to 0.6 m. A spherical leaf distribution of the sugar beet plants was assumed. Further details on the SCOPE model can be found in van der Tol et al., (2009).

3.2.3. Airborne (*HyPlant*) measurements 2012

Airborne images were acquired on the 23rd of August 2012 using the imaging spectrometer *HyPlant* (Specim, Oulo, Finland). *HyPlant*, which has been operated since 2012 by the research center Jülich, was developed within the framework of ESA's Fluorescence Explorer (FLEX) mission Phase A activities and is an airborne demonstrator for the FLEX satellite mission. It was specifically designed to monitor functional vegetation information, including emitted F and other important plant functional traits. The instrument is a push-broom imager consisting of two modules measuring surface radiance in the spectral ranges from 380 nm to 2500 nm (DUAL module) and from 670 nm to 780 nm (FLUO module). The high resolution FLUO module covers the red and far-red region of the electromagnetic spectrum with high spectral resolution (FWHM of 0.25 nm). This allows retrieving emitted F signals in the two atmospheric oxygen bands, O₂-A (760 nm; F_{760}) and O₂-B (687 nm; F_{687}). The

good performance of *HyPlant* enables, for the first time, F_{760} and F_{687} to be measured in high spatial resolution at field and ecosystem scale (Rascher et al., 2015; Rossini et al., 2015).

In addition to F_{760} and F_{687} , five commonly applied vegetation indices sensitive to different properties of vegetation canopies were calculated. As biomass sensitive indices, the Normalized Different Vegetation Index, NDVI, (Rouse et al., 1973), and the Enhanced Vegetation Index, EVI, (Huete et al., 2002) were evaluated. The Transformed Chlorophyll Absorption in Reflectance Index, TCARI, (Haboudane et al., 2002) and the Modified Chlorophyll Absorption Ratio Index, MCARI2, (Haboudane et al., 2004) were both tested as sensitive indices for green biomass. Furthermore, the performance of the Photochemical Reflectance Index, PRI, (Gamon et al., 1992) was investigated. The PRI is sensitive to pigment changes related to the xanthophyll cycle and frequently employed as proxy for LUE as an indicator for NPQ activity (Peguero-Pina et al., 2008; Porcar-Castell et al., 2012; Rahimzadeh-Bajgiran et al., 2012). The equations for all listed indices can be found in Table 1.

Table 1: Equations for examined spectral vegetation indices

Equation	Reference
$NDVI = \frac{R_{800} - R_{670}}{R_{800} + R_{670}}$	(Rouse, 1974)
$EVI = 2.5 \cdot \frac{R_{800} - R_{670}}{R_{800} + 6 \cdot R_{670} - 7.5 \cdot R_{400} + 1}$	(Huete et al., 2002)
$PRI = \frac{R_{570} - R_{531}}{R_{570} + R_{531}}$	(Gamon et al., 1992)
$TCARI = 3 \cdot [(R_{700} - R_{670}) - 0.2 \cdot (R_{700} - R_{550}) \cdot \left(\frac{R_{700}}{R_{670}}\right)]$	(Haboudane et al., 2002)
$MCARI2 = \frac{1.5 \cdot (2.5 \cdot (R_{800} - R_{670}) - 1.3 \cdot (R_{800} - R_{550}))}{\sqrt{2 \cdot (R_{800} + 1)^2 - (6 \cdot R_{800} - 5 \cdot \sqrt{R_{670}}) - 0.5}}$	(Haboudane et al., 2004)

3.3. Merzenhausen campaign 2015

The campaign in 2012 showed that an infield spectrometer system was needed which is able to detect F_{760} and F_{687} with high temporal and spectral resolution over several days. In the 2015 campaign, a new fluorescence measurement system was used (*SIF-Sys*), which was able to fulfill these requirements. The goal of the 2015 campaign was to track changes in the relationship of LUE, PRI, F_{760} and F_{687} under changing variable condition during growing season.

The experimental site of the second measurement campaign was located close to the village of Merzenhausen (50.930N, 6.296E, altitude 92m above sea level). The site covers a 7.2ha (200m x 300m) flat field cropped with sugar beet. Sowing was in mid of April (day of year (DOY): 103), harvest was end of October (DOY: 302). Ground measurements started end of June (DOY: 181), when leaves were fully developed (BBCH-Code: 39) and ended end of August (DOY: 243). The automated system started taking measurements at 6 a.m. UTC and stopped at 4 p.m. UTC. The field soil texture is classified as silt loam (Ahrends et al., 2014; Graf et al., 2013). Within the period of our measurements, a heat wave struck the region with temperatures up to 35° C and absent precipitation, resulting in a decrease of soil moisture from DOY: 179 to DOY: 199.

3.3.1. Field spectroscopy

The field spectrometer system (*SIF-Sys*) is a successor of earlier developments of the Forschungszentrum Jülich and the University Milano Bicocca (Cogliati et al., 2015a; Julitta et al., 2016; Rossini et al., 2010). *SIF-Sys* consists of one or more spectrometers, connected to a double fiber in a way that the vegetation and the hemispherical irradiance can be observed at the same time and by the same device. A microcontroller, running a specially developed firmware, controls the spectrometer, the optical system, and stores acquired spectral data in the SD card. The instrument performance is observed by a couple of environmental and internal sensors which read-out in parallel. To ensure stable measurements, the spectrometer is housed in a separate and actively cooled insulated chamber. The technical description and evaluation can be found in Burkart et al. (2015).

The optical path of the system is optimized for high light-throughput for a decrease in integration time and a simultaneous increase of the signal-to-noise level. With this very fast acquisition time, around 5000 measurements per day are possible. The retrieval of sun induced fluorescence is possible in the O₂A and O₂B oxygen absorption bands, allowing for insights about the photosynthetic performance of PSII and PSI. By using an active fluorescence reference (LED) within the plant canopy, the error budget of

SIF-Sys can be estimated and tracked over the whole measurement period (Burkart et al. 2015).

The error of the fluorescence retrieval is determined by fast changes in the irradiance, the optical fibers (e.g. spectral shift), the measurement system (temperature dependency) and the fitting of the retrieval itself. The newly developed LED error estimation scheme allows for a quantification of random and systematic errors of the retrieval. Two LEDs with a spectral range over the O₂A and O₂B band respectively, were placed within the field of view of the *SIF-Sys*. The LEDs are switched on around 1.2 seconds after the radiance measurement. The received signal, consists of the vegetation radiance and the LED light. The power of the LED within the respective absorption band is calculated as:

$$LED_{power} = LED_{\omega} - L_{\omega} \quad (22)$$

Where LED_{ω} is the radiance of the vegetation in addition to the LED signal and L_{ω} the radiance at the lowest point within the respective absorption band (ω). The LED_{power} is compared with a LED_{power} estimated after the iFLD retrieval where the $LED_{power,iFLD}$ is calculated as:

$$LED_{power,iFLD} = FLED_{\omega} - F_{\omega} \quad (23)$$

Where F_{ω} is the retrieved fluorescence and $FLED_{\omega}$ the retrieved fluorescence from the vegetation and LED in the respective absorption band ω . Thus the absolute retrieval error ($\delta_{retrieval}$) is:

$$\delta_{retrieval} = LED_{power,iFLD} - LED_{power} \quad (24)$$

3.3.2. Eddy- covariance tower measurements

A permanently installed EC-tower was located 3 m to the field spectrometer setup. The EC method is based on the concept that turbulent fluxes, so called eddies, transport energy and matter between surface and atmosphere, allowing estimates of surface fluxes. The vertical components of these eddies were measured with an open-path infrared gas analyzer (LI7500, LI-COR, Lincoln, NE, USA) at a measurement height of 2 m and a frequency of 20 Hz. The net CO₂ exchange or net ecosystem exchange (NEE) was estimated as:

$$NEE = \frac{\rho_a}{m_{CO_2}} \overline{w'c'} \quad (25)$$

Where ρ_a is the dry air density (kg m⁻³), m_{CO_2} is the molar mass of CO₂ (44.01 g mol⁻¹) and $\overline{w'c'}$ the covariance of w the vertical wind velocity (m s⁻¹) and c the mixing ratio of carbon dioxide (ppm). Resulting NEE is averaged to 30 minutes. Analog to chapter 3.2.2, GPP was estimated using the online flux partitioning tool based on Reichstein et al. (2005).

3.3.3. HyPlant measurements 2015

For the *HyPlant* campaign 2015 one overflight over Merzenhausen was realized at the 30th of June. Sun induced fluorescence at 760 nm and at 680 nm were mapped with a 1 m resolution at 1:02 p.m. UTC. Even though the technical specifications of the *HyPlant* sensor did not change from 2012 to 2015, hardware updates, preprocessing software developments and retrieval software updates resulted in higher image quality. For instance, a hardware updates corrected for a too wide point spread function and decreased the occurrence of temporarily detector failures (bad pixels). Preprocessing Software helped in the removal of the remaining bad pixels and in the compensation of remaining effects stemming from the point spread function. The retrieval algorithm was updated from the linear 3FLD method to the non-linear iFLD method, which allowed the retrieval of fluorescence in the O₂B Band (F₆₈₀) and reduced the noise in F₇₆₀ and F₆₈₀ maps.

3.3.4. Calculating indicators for plant stress

Plant stress can be defined as a disturbance down regulating the plant capacity for CO₂ assimilation (lowering the LUE). As explained in detail in Sections 2.1 and 2.7, plant stress can be triggered by many different environmental conditions. The most common

kinds of stress are water deficiency, low and high temperatures, lack of nutrients, illness and pest infections. Since the field used in this study was frequently fertilized and no illnesses or pest infections were noted, this work focuses on the description of heat and water stress. As heat and water stress are closely linked with each other (Seneviratne et al., 2006), it is difficult to treat them separately. In this campaign, only 2m air temperature measurements were available, while a robust interpretation of temperature stress would require knowing, in addition, the canopy temperature. Attempts to calculate canopy temperature by inverting the surface energy balance method (Jackson et al., 1987) were insufficient because of the high uncertainty of the retrieved canopy temperature. As temperature stress on plants is largely due to the increase of evaporative demand in the stomata, the vapor pressure deficit (VPD) was calculated as an indicator of stress due to high temperatures. The vapor pressure deficit is defined as the difference of the ambient water vapor pressure and the potential saturated water vapor of the air. A high VPD results in an accelerated plant transpiration because of diffusion processes (c.f. Section 2.1.3). VPD is calculated as:

$$VPD = \left(\frac{100 - RH}{100} \right) \cdot SVP \quad (26)$$

Where RH is the relative humidity, calculated from absolute humidity and temperature, and SVP (in Pa) the saturated vapor pressure calculated as:

$$SVP = 0.6108 \cdot 10^{\left(\frac{7.5 \cdot T}{T + 237.3} \right)} \quad (27)$$

and T is the temperature in Celsius. The temperature was measured with a sonic Anemometer (CSAT3, Campbell Scientific, Inc., Logan, USA) and the absolute humidity with a humidity probe (HMP45C, Vaisala Inc., Helsinki, Finland). Both were installed on the 2m-high micrometeorological station in a distance of 3m to the field spectrometer and averaged over 30min.

Drought stress can be best described by the plant available water (PAW). The PAW describes how much water (in mm) is available for the plant and was calculated as:

$$PAW = (\theta - \theta_{wp}) \cdot \left(\frac{md}{10} \right) \quad (28)$$

Where θ is the volumetric soil water content (vol %), measured with a water content reflectometer (CS616, Campbell Scientific, Inc., Logan, USA), md is the measurement depth (2.5 cm) and θ_{wp} the wilting point. The wilting point was derived on the basis of

Rawls and Brakensiek (1989) as a function of the texture, where the texture was ascertained in earlier field campaigns.

Table 2: Soil texture in four depths in Merzenhausen

	0-35 (cm)	35-47 (cm)	47- 97 (cm)	97-150 (cm)
Clay (%)	13.4	18	22.7	18
Silt (%)	81.9	78.9	74.9	79.4
Sand (%)	4.7	3.1	2.4	2.6

The most direct indicator for plant stress is the LUE. Under non stressed conditions, the LUE follows a diurnal cycle with highest values in the morning and evening and lowest values during noon because of light saturation effects of the photosystems. Under stress conditions the plant has particular adaptation strategies (c.f. Section 2.1.4) and can therefore compensate for certain levels of stress. Under severe stress however, LUE is much lower than under non-stressed conditions. The LUE was calculated as described in Eq. 2, where PAR was derived from a quantum sensor (LI-190, LI-COR, Lincoln, NE, USA) and fAPAR was calculated from the difference between incident and reflected radiance, integrated over the spectral region from 400 nm to 700 nm.

3.3.5. Data processing

To avoid errors from cloud related light scattering 17 out of 62 measurement days (DOY: 182 to DOY: 243) under clear sky conditions were selected for this study. Outliers were removed by filtering values three times the standard error. In order to harmonize the data, the dataset was resampled to the lowest temporal resolution the dataset provided (30 min from EC measurements). The 30 min dataset (306 samples) was used to analyze if short term adaptation strategies by the plant can be tracked by fluorescence and PRI. For a better understanding of the inter-daily relationship of LUE, PRI, F the dataset was resampled to daily mean (17 samples) values. Table 3 gives an overview of the parameters used by this study.

Table 3: measured and derived parameters of the Merzenhausen campaign

Parameter	Abbreviation	Unit	Data basis	Equation
Vapor pressure deficit	VPD	hPa	Temperature & absolute humidity	Eq. 26
Plant available water	PAW	mm	Soil water content	Eq. 28
light use efficiency	LUE	$\mu\text{mol CO}_2 / \mu\text{mol photons}$	NEE & APAR	Eq. 2
Photochemical reflectance indices	PRI	a.u.	radiance & irradiance	Table 1
fluorescence yield at 760nm	$F_{760\text{yield}}$	$(\text{mW}/\text{sr}/\text{nm}) / (\mu\text{mol photons}/\text{s})$	radiance & irradiance	Eq. 17
fluorescence yield at 687nm	$F_{687\text{yield}}$	$(\text{mW}/\text{sr}/\text{nm}) / (\mu\text{mol photons}/\text{s})$	radiance & irradiance	Eq. 17
fluorescence ratio	F_{ratio}	ratio	radiance & irradiance	F_{687} / F_{760}

4. Model descriptions

4.1. Data usage

For an adequate comparison and interpretation of the GPP model approaches (c.f. Section 4.2), it is necessary to understand how LUE, PRI and F are affected by changing environmental conditions. For this purpose, the ground measurements of 2015 were used to analyze the changing relationship of LUE, PRI and F in time, while the 2012 maps are used to better understand the diurnal change in spatial patterns of F_{760} , F_{680} , F_{ratio} , $F_{760yield}$ and $F_{680yield}$. Subsequently, temporal and spatial patterns of GPP are calculated by four different models. While intra- and inter-daily estimations of GPP are driven and validated by the 2015 dataset, the spatial patterns of estimated GPP are driven and validated by the 2012 dataset. Due to the lack of ground measurements of F_{687} in 2012, the performance of the multiple regression model in estimating spatial patterns of GPP had to be validated with the 2015 dataset.

4.2. Estimation of GPP

4.2.1. Reflectance based vegetation indices

The estimation of GPP by reflectance based VIs are based on the LUE approach by Monteith. In regional or global applications of the Monteith LUE approach, the LUE is normally estimated as a function of maximum LUE, minimum T and VPD (Running et al., 2004). For this study, it was decided to use measured mean LUE, which allows for a better comparison between reflectance and fluorescence based GPP models.

Intra-daily GPP_{VI} was calculated based on 30min averaged PAR derived from *SIF-Sys*, 30min averaged *fAPAR* derived from VIs and daily mean LUE derived from eddy covariance measurements. Inter-daily GPP_{VI} was calculated based on daily averaged PAR derived from *SIF-Sys*, daily averaged *fAPAR* derived from VIs and daily mean LUE derived from eddy covariance measurements. GPP derived from this approach is referenced as GPP_{VI} and expressed as:

$$GPP_{VI} = PAR_{SIF-Sys} \cdot fAPAR_{VI} \cdot \overline{LUE}_{EC} \quad (29)$$

Where $fAPAR_{VI}$ was calculated as:

$$fAPAR_{VI} = k \cdot VI_{SIF-Sys} \quad (30)$$

Where k is a linear scaling factor derived from the relationship of measured $fAPAR$ and $VI_{SIF-Sys}$. $VI_{SIF-Sys}$ was calculated from spectral measurements of $SIF-Sys$.

Maps of GPP were calculated for the three overflights by approximating $fAPAR$ from four different vegetation indices. Where GPP_{VI} can be expressed as:

$$GPP_{VI} = PAR_{CC} \cdot fAPAR_{VI} \cdot LUE_{CC} \quad (31)$$

The used diurnal cycle of PAR_{CC} corresponds to the mean of seven canopy chamber measurements. Spatial information of $fAPAR_{VI}$ was calculated as:

$$fAPAR_{VI} = k \cdot VI_{HyPlant} \quad (32)$$

With k estimated from the relationship between in-field modeled $fAPAR_{CC}$ (cf., Section 3.2.3) and all $HyPlant$ VIs for each individual flight line. Actual LUE_{CC} for sugar beet was calculated for each overflight time window as:

$$LUE_{CC} = \frac{GPP_{CC}}{APAR_{CC}} \quad (33)$$

Where GPP_{CC} corresponds to the mean of the seven canopy chambers and $APAR_{CC}$ to the averaged model results calculated in Section 3.2.2.

4.2.2. Statistical GPP-F relationship model

Based on the assumption that GPP and F scale linearly with each other, GPP can be estimated with a linear regression model. GPP derived from this approach is referenced as GPP_F and calculated as:

$$GPP_F = a + b \cdot F \quad (34)$$

Where a is the offset and b the slope of the regression. For the intra-daily estimation the regression model was derived from 30 min GPP_{EC} and $F_{760,SIF-Sys}$. GPP_{EC} was derived from eddy covariance measurements and $F_{760,SIF-Sys}$ from in situ spectrometer measurements in 2015. The derived regression model for the intra-daily dataset is:

$$GPP_F = 10.5 + 12.9 \cdot F_{760,SIF-Sys} \quad (35)$$

Where the R^2 is 0.31 and the uncertainty of the offset and of the slope is ± 1.0 for both.

The inter-daily estimation of the regression model was derived from daily averaged GPP_{EC} and $F_{760,SIF-Sys}$ measurements (Figure 31 B). The derived regression model for the inter-daily dataset is:

$$GPP_F = 15.0 + 9.7 \cdot F_{760,SIF-Sys} \quad (36)$$

The R^2 is 0.51 and the uncertainty of the offset and of the slope is ± 2.4 and 2.3 respectively.

The spatiotemporal estimation of GPP_F , based on a regression model derived from GPP_{CC} and $F_{760,MSS}$ (Figure 31 C), and GPP_{CC} is derived from the averaged seven canopy chambers and $F_{760,MSS}$ from in situ spectrometer measurements in 2012. The derived regression model for the spatiotemporal estimation of GPP_F is:

$$GPP_F = 4.72 + 13.44 \cdot F_{760,MSS} \quad (37)$$

Where the R^2 is 0.72. The uncertainty of the offset and slope of all linear regression models were calculated from the orthogonal distance of the standard error in GPP and F_{760} .

4.2.3. Statistical LUE- F_{760} relationship model

Based on the approach by Guanter et al. (2014), F can be expressed in analogy to Eq. (1) as:

$$F = PAR \cdot fAPAR \cdot F_{yield} \quad (38)$$

By rearranging Eqs. (1) and (38) GPP can be expressed as:

$$GPP_\phi = F_{760} \cdot \frac{LUE}{F_{760yield}} \quad (38)$$

GPP derived from this approach is referenced as GPP_ϕ . For the intra-daily estimation of GPP_ϕ , 30 min averaged F_{760} retrieved from $SIF-Sys$ is used. The LUE- $F_{760yield}$ ratio is based on daily averaged LUE_{EC} and $F_{760yield,SIF-Sys}$ measurements. The inter-daily

estimation of GPP_{ϕ} , relies on daily averaged $F_{760,SIF-Sys}$ and daily averaged LUE_{EC} and $F_{760yield,SIF-Sys}$ measurements.

$$GPP_{\phi} = F_{760,SIF-Sys} \cdot \frac{\overline{LUE_{EC}}}{F_{760yield,SIF-Sys}} \quad (39)$$

Diurnal spatiotemporal patterns of GPP_{ϕ} are calculated as:

$$GPP_{\phi} = F_{760,HyPlant} \cdot \frac{LUE_{CC}}{F_{760yield,MSS}} \quad (40)$$

Where $F_{760,HyPlant}$ is derived from *HyPlant* 2012 aerial images for the three different overflight times, LUE_{CC} is derived from the mean of the seven gas exchange and $F_{760yield,MSS}$ is calculated from MSS spectrometer measurements.

4.2.4. Multiple regression model

The estimation of GPP_{ϕ} by the LUE- F_{760} relationship model does not consider that excessive energy can also be released as heat by the process of non-photochemical quenching (NPQ). To overcome this limitation a multiple regression model was used for estimating intra-, inter-daily and spatial GPP_{MR} . Based on the assumption that the PRI can be used as a proxy for NPQ, the non-linear relationship between PRI, $F_{760yield} + F_{687yield}$ and LUE define a model for the intra- and inter-daily estimation of GPP_{MR} . The model makes use of PRI and the additive yields of red and far-rad F in linear and quadratic terms, where the calculation coefficients differ for the intra- and inter-daily estimations. The intra-daily model is:

$$LUE_{MR} = 0.02 - 4.91 \cdot (F_{760yield} + F_{687yield}) - 0.20 \cdot PRI + 603.33 \cdot (F_{760yield} + F_{687yield})^2 + 4.66 \cdot PRI^2 \quad (41)$$

The inter-daily model is:

$$LUE_{MR} = 0.01 + 7.79 \cdot (F_{760yield} + F_{687yield}) - 0.05 \cdot PRI - 1240.63 \cdot (F_{760yield} + F_{687yield})^2 + 5.18 \cdot PRI^2 \quad (42)$$

The relationship of intra- and inter-daily PRI, $F_{760yield} + F_{687yield}$ and LUE are described in more detail in Section 5.2.3 and 5.2.4 respectively.

Based on the Monteith LUE model, GPP_{MR} can be calculated as:

$$GPP_{MR} = PAR \cdot fAPAR \cdot LUE_{MR} \quad (43)$$

For the intra- and inter-daily estimates, PAR and fAPAR are derived from the *SIF-Sys* measurements. For the spatial estimates of GPP_{MR} , PAR was derived from *SIF-Sys* measurements and fAPAR from *HyPlant* EVI as explained with Eq. 32.

4.3. Spatio temporal changes of fAPAR_{VI} and F₇₆₀yield

The spatial patterns of greenness-based and fluorescence-based estimates of GPP are characterized by fAPAR_{VI} and F₇₆₀, both derived from *HyPlant* measurements. Since temporal changes of F₇₆₀ mainly depend on APAR, F₇₆₀yield was calculated as:

$$F_{760yield} = \frac{F_{760}}{PAR_{CC} \cdot fAPAR_{VI}} \quad (44)$$

Maps of fAPAR_{VI} and F₇₆₀yield were grouped by overflight time and crop type. Groups are separated in homogenous sugar beet fields, heterogeneous sugar beet fields, rape seed and maize. To avoid errors due to point spread, field edges were not selected.

4.4. Model validation

To validate the performance of the GPP estimations by greenness-based and fluorescence-based approaches, results were compared with in-field measurements of GPP derived from an eddy-covariance tower and gas exchange chamber. Since the estimation of intra- and inter-daily GPP is based on the measurements from Merzenhausen 2015, results were compared with available eddy covariance measurements. Except for GPP_{MR} , spatiotemporal patterns of modeled GPP were compared with gas exchange chamber measurements from Selhausen 2012. The mean of GPP_{EVI} , GPP_F and GPP_Φ within a 3 m buffer around the canopy chamber positions was calculated, in order to minimize potential errors of the canopy chamber global positioning system and errors related to the point spread function of *HyPlant*.

As F₆₈₇yield and PRI were not measured with the MSS in 2012, spatial GPP_{MR} was calculated with *HyPlant* 2015 and validated with upscaled GPP derived from an eddy-covariance tower. By analyzing wind speed and direction the footprint of the EC-Tower measurements during the 2015 *HyPlant* overflight (1p.m.) was located. The average fAPAR within the footprint was calculated from *HyPlant* as described in Eq. 32. The

relationship between fAPAR and GPP_{EC} within the footprint is then used to estimate spatial patterns of GPP.

All results were compared for their coefficient of determination (R^2), root mean square error (RMSE) and relative RMSE (rRMSE), the statistical bias (BIAS) and the slope of the regression line (slope). The R^2 is a statistical measure of how much variance of the dependent variable Y can be explained by a regression model. The difference of the measured value (Y_i) and the predicted value (\hat{Y}_i) are the residuals and the sum of all squared residuals is the variance. The coefficient of determination is given as the ratio of explained and overall variance of the model.

$$R^2 = \frac{\sum_{i=1}^n (\hat{Y}_i - \bar{Y})^2}{\sum_{i=1}^n (Y_i - \bar{Y})^2} \quad (45)$$

The RMSE is a measure of the difference between predicted and observed values:

$$RMSE = \sqrt{\frac{\sum_{i=1}^n (Y_i - \hat{Y}_i)^2}{n}} \quad (46)$$

The BIAS between predicted and observed values is calculated as:

$$BIAS = \frac{\sum_{i=1}^n (Y_i - \hat{Y}_i)}{n} \quad (47)$$

4.5. Model uncertainties

Each parameter used by the four different models was attributed with an error range. The error range of each parameter propagates to the absolute model uncertainty. The uncertainty for MSS derived PAR, fAPAR and F_{760} as well as *SIF*-Sys derived PAR, fAPAR and PRI is based on the square root of their variance (standard deviation; σ). The standard deviation was calculated as:

$$\sigma = \sqrt{\frac{1}{n} \sum_{i=1}^n (X_i - \bar{X})^2} \quad (48)$$

Where \bar{X} is the arithmetic mean of the variable X .

The uncertainty estimation for *SIF*-Sys derived F_{760} and F_{687} is based on an active light reference within the measurement footprint and is in detail described in Section 3.3.1.

GPP values derived from EC measurements were attributed with an relative error of 10% (Foken, 2006).

The random error of all *HyPlant* derived parameters was calculated from a homogeneous training area within the maps, while systematic error in the $F_{760,HyPlant}$ retrieval method were considered as described in Damm et al. (2011). Uncertainties of the linear regression models were calculated from the error of the dependent and independent variables. The absolute uncertainty of each model depends on the propagation of the error for each parameter.

5. Results

For a better understanding of diurnal plant adaptation strategies under excessive heat and water scarcity, the diurnal measurements of 2012 and the seasonal measurements of 2015 are described first. The 30-min averaged and daily averaged data of the 2015 campaign are then used to describe the intra- and inter-daily relationships of LUE, PRI, $F_{760\text{yield}}$ & $F_{687\text{yield}}$ and F_{ratio} to VPD and PWD, as well as between each other. Fluorescence maps of the 2012 *HyPlant* campaign were used to analyze and compare spatiotemporal patterns of EVI, F_{760} , F_{687} , F_{ratio} , $F_{760\text{yield}}$ and $F_{687\text{yield}}$. After a quantification of the *SIF-Sys* measurement uncertainty, intra- and inter-daily, as well as spatiotemporal estimates of GPP are presented and compared with each other.

5.1. In situ measurements

Since the ground-based measurements of 2012 are the basis of the spatiotemporal GPP estimation, the diurnal dynamics of the variables on the airborne campaign day (23rd of August 2012) are analyzed here in more detail. Field averaged APAR_{CC} , used for the LUE_{CC} calculation, increased to a maximum of $1300 \mu\text{mol m}^{-2}\text{s}^{-1}$ at solar noon. The field average GPP_{CC} sharply increased from sunrise to a maximum CO_2 uptake of $35 \mu\text{mol CO}_2 \text{ m}^{-2}\text{s}^{-1}$ at 9.20 a.m. UTC. Afterwards, the uptake slowly decreased until 3.00 p.m. UTC, when the measurements stopped (Figure 13A). During the morning hours, a decrease of field averaged LUE_{CC} from 0.037 to a minimum of 0.024 after solar noon and a subsequent increase to 0.029 until the end of measurements at 3 p.m. (Figure 13C) can be observed.

MSS measurements started at 8:35 a.m. with APAR_{MSS} values of 255 W m^{-2} and F_{760} values of $1.48 \text{ mW m}^{-2}\text{sr}^{-1}\text{nm}^{-1}$. APAR_{MSS} and F_{760} followed a typical diurnal cycle for clear sky conditions, albeit with F_{760} fluctuating more strongly. The maxima of APAR_{MSS} and F_{760} were reached around 11 a.m. with 350 W m^{-2} and $2.4 \text{ mW m}^{-2}\text{sr}^{-1}\text{nm}^{-1}$, respectively. Both values decreased ($\text{APAR}_{\text{MSS}} = 220 \text{ W m}^{-2}\text{s}^{-1}$ and $F_{760} = 1.3 \text{ mW m}^{-2}\text{sr}^{-1}\text{nm}^{-1}$) until 3:00 p.m. (Figure 13B). To reduce the noise of the F_{760} signal, a moving average of 30 m was calculated for the $F_{760\text{yield,MSS}}$. From 8:35 a.m. to 12:40 p.m., $F_{760\text{yield,MSS}}$ showed a steady decrease from 0.0066 to 0.0056. Afterwards, it steadily increased to 0.0070 at 3:00 p.m. (Figure 13C).

The resulting relationship between LUE_{CC} and $F_{760\text{yield,MSS}}$ changed over the measurement day resulting in a relative low coefficient of determination ($R^2 = 0.17$). From 8:35 a.m. to solar noon, the ratio between LUE_{CC} and $F_{760\text{yield,MSS}}$ showed a strong decrease, followed by a more or less constant relationship by the end of measurements (Figure 13D).

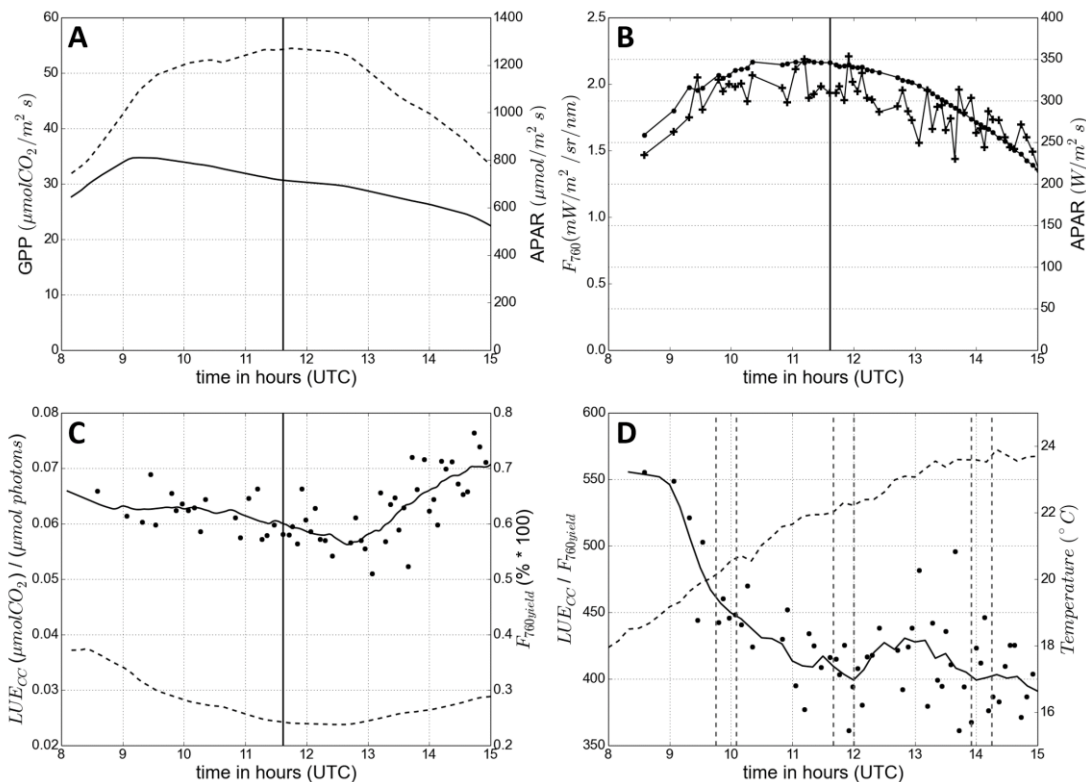


Figure 13: Interpolated diurnal cycle of gross primary production (GPP; solid line) and absorbed photosynthetic active radiation (APAR; dashed line) averaged over seven net ecosystem exchange (NEE) chambers within a sugar beet field. Vertical line marks local solar noon (A). Diurnal sun-induced chlorophyll fluorescence (F_{760} ; crosses) and APAR (dots) measured by Manual Spectrometric System (MSS). Vertical line marks local solar noon (B). Interpolated diurnal light use efficiency (LUE_{cc} ; dashed line) derived from canopy chambers, $F_{760yield}$ (points) and moving average of $F_{760yield}$ (solid line) derived from MSS. Vertical line marks local solar noon (C). Diurnal relationship of LUE_{cc} to $F_{760yield}$ (points), 30 m moving averaged (solid line), diurnal course of temperature (dashed horizontal line) and flight windows (dashed vertical lines) (D).

From the 15 days of measurements with clear sky conditions in Merzenhausen during 2015, four exemplary days were chosen to describe the diurnal behavior of the key parameters (c.f. Table 3) in detail. The four chosen days represent high temperature (noon T over 30 °C, PAW over zero mm; red squares, DOY: 242), water scarcity (noon T under 25 °C, PAW under zero mm; blue triangles, DOY: 187), high temperature in combination with drought (noon T over 30 °C, PAW under zero mm; black stars, DOY: 182) and moderate temperature with sufficient water (noon T under 25 °C, PAW over zero mm; green dots, DOY: 238) conditions (Figure 14). Because of the known temperature-moisture feedback (Seneviratne et al., 2006), VPD is highest on days with high temperature and water scarcity. The LUE shows, for all four cases, a decrease until solar noon and a subsequent rise to the same- or higher LUE level. However,

during the days affected by water scarcity or by a combination of water scarcity and high temperature, the light-use is by 50 to 100% less efficient than under sole high temperature or moderate conditions. Especially after solar noon, the LUE increases under high temperature or moderate conditions much faster than under conditions of water scarcity or a combination of water scarcity and high temperature. No significant difference in LUE can be found between days under moderate or high temperature conditions. Under water scarcity only, the LUE is slightly higher than for days affected by both water scarcity and high temperature.

The PRI follows a diurnal cycle with the highest values during solar noon and the lowest values in the morning and evening. Highest absolute values were measured on days affected by water scarcity. On days with sufficient soil water, the PRI is lower and less variable. Overall, the PRI inversely follows the LUE.

Under water scarcity or water scarcity and high temperature conditions, $F_{760\text{yield}}$ followed a diurnal cycle with lowest values during solar noon and highest values in the morning and evening. Under high temperature and moderate conditions, $F_{760\text{yield}}$ steadily decreased from 7 a.m. to 4 p.m. by 35-50%. Under sole water scarcity, values of $F_{760\text{yield}}$ were nearly as low as under water scarcity combined with high temperature conditions, when the lowest values were found. Nevertheless, after solar noon $F_{760\text{yield}}$ rose to the same intensity as under high temperature or moderate conditions.

The $F_{687\text{yield}}$ showed lowest values under water scarcity conditions before solar noon, and highest values under water scarcity & high temperature conditions. Under sole high temperature and moderate water conditions, $F_{687\text{yield}}$ was quite stable over the day. In general, after solar noon $F_{687\text{yield}}$ values did not vary strongly under any condition. Under water scarcity and water scarcity & high temperature conditions, the ratio between F_{687} and F_{760} strongly increased until noon and subsequently decreased until the evening. The days under sole high temperature and moderate conditions show a much slower and not as strong increase of the F_{ratio} during the day, both being very similar to each other.

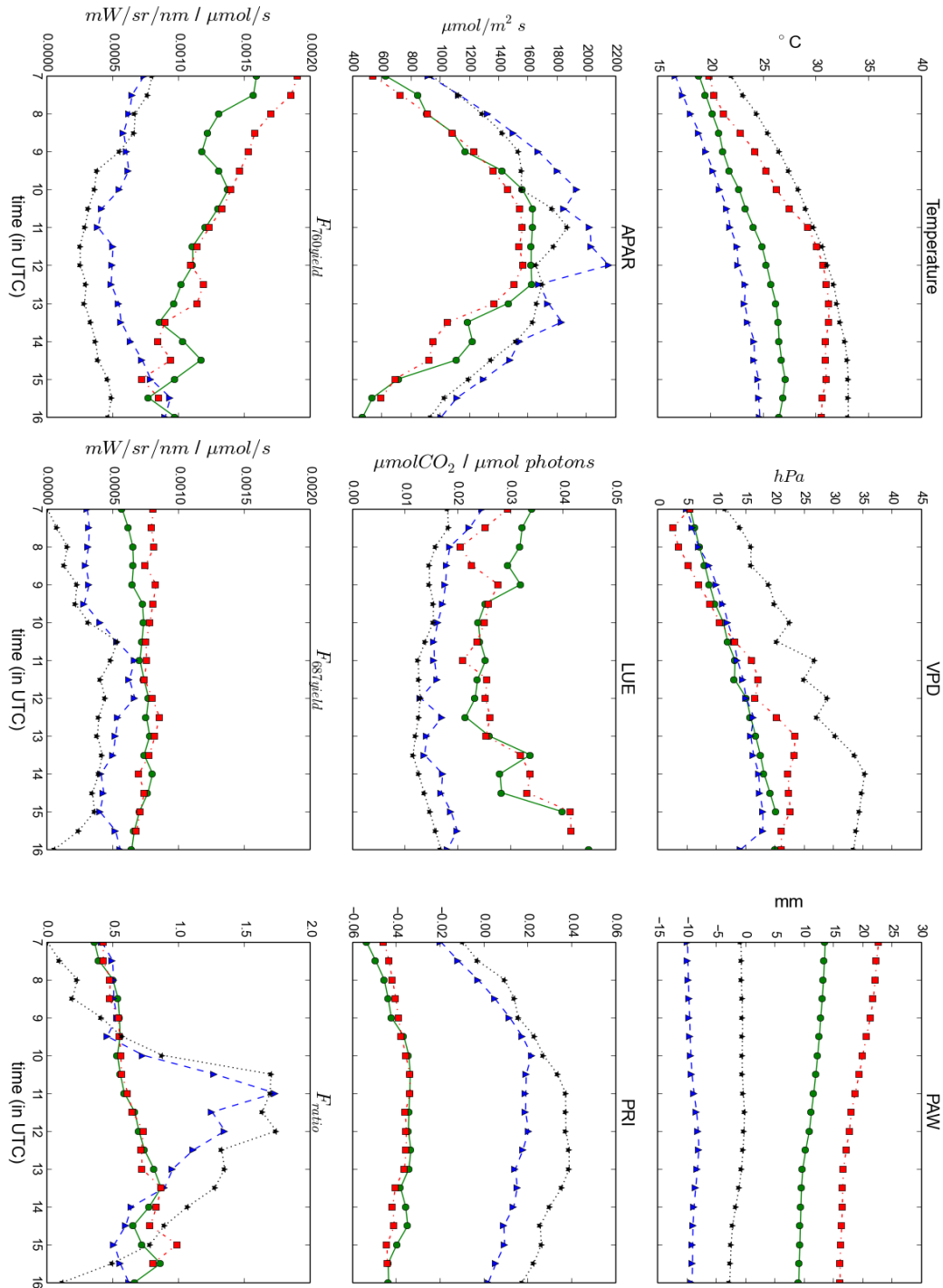


Figure 14: Diurnal evolution of absorbed photosynthetically active radiation (APAR), temperature, plant available water (PAW), light use efficiency (LUE), Photochemical Reflectance Indices (PRI), fluorescence yield in the O₂A- and O₂B-Band (F_{760}^{yield} and F_{687}^{yield}) and the ratio of red to far red fluorescence (F_{687}/F_{760}) for four representative days in 2015 within a sugar beet field located in Merzenhausen, Germany. The four chosen days represent high temperature (noon T over 30°C, PAW over zero mm; red squares, DOY: 242), water scarcity (noon T under 25°C, PAW under zero mm; blue triangles, DOY: 187), high temperature in combination with drought (noon T over 30°C, PAW under zero mm; black stars, DOY: 182) and moderate temperature with sufficient water (noon T under 25°C, PAW over zero mm; green dots, DOY: 238) conditions.

For the 2012 dataset, the diurnal relationship between LUE_{CC} and the averaged $F_{760yield,MSS}$ was evaluated separately for data acquired before and after LUE_{CC} and $F_{760yield,MSS}$ are lowest (one hour after solar noon) (Figure 15). From morning to afternoon (12:45 p.m.) the relationship between LUE_{CC} and $F_{760yield,MSS}$ shows an exponential decrease with an R^2 of 0.8. After 12:45 p.m. $F_{760yield,MSS}$ values are characterized by a wider range than the LUE_{CC} values, leading to a steep slope coefficient of the linear regression fit and a higher coefficient of determination ($R^2 = 0.95$).

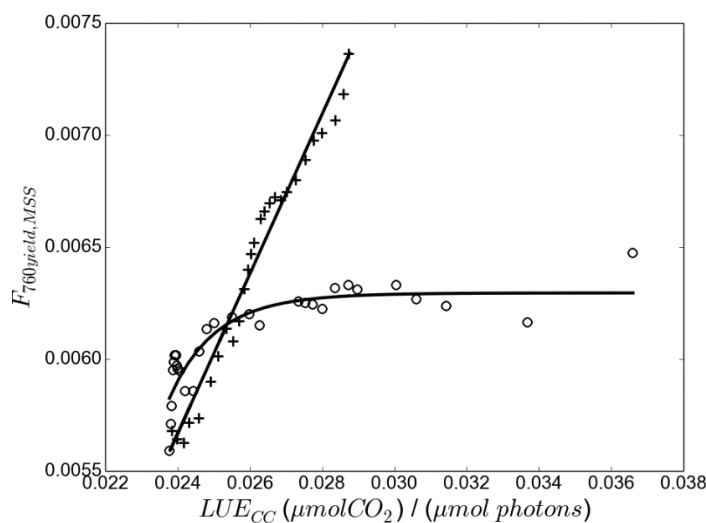


Figure 15: Relationship of LUE_{CC} estimated from canopy gas-exchange chamber measurements and averaged $F_{760yield,MSS}$ from MSS fluorescence ground measurements. Points symbolize measurements until 12:45 p.m. UTC, cross markers symbolize measurements from 12:45 p.m. UTC to 3:00 p.m. UTC. The lines show the best fit of the relationship. The coefficient of determination (R^2) for before noon- and after 12:45 p.m. UTC are 0.80 and 0.95 respectively.

To further investigate the diurnal evolution of LUE to $F_{760yield}$, the four exemplary days (Figure 16) and the full dataset (Figure A52) of the 2015 Merzenhausen campaign were analyzed. All days in Figure 16 show a strong decrease of $F_{760yield}$ until solar noon with a weak decrease in LUE. After solar noon, the relationship evolves differently for each day. Under normal environmental conditions, as well as under high VPD conditions, the LUE strongly increases while $F_{760yield}$ stays relatively constant. Under water scarcity or water scarcity with high VPD, both LUE and $F_{760yield}$ increase, showing thereby a stronger relationship of LUE and $F_{760yield}$ under environmental stress.

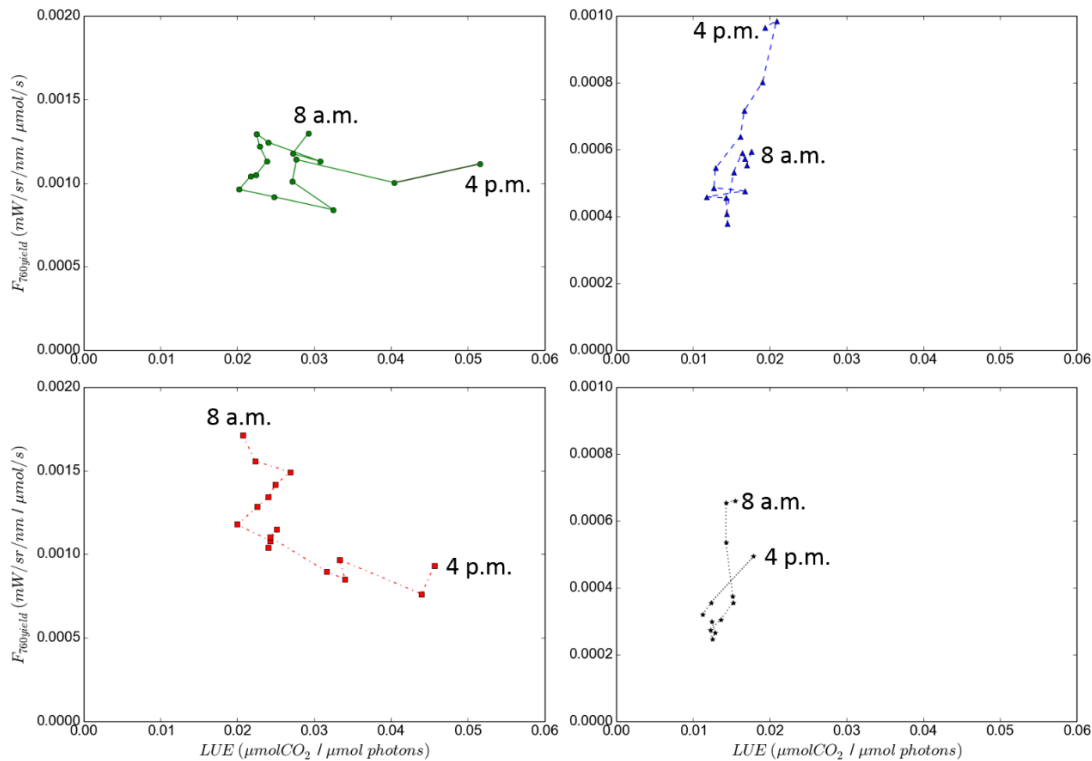


Figure 16: Diurnal change of LUE and $F_{760yield}$ relationship during an unstressed day (green line, top left, DOY: 238), a day under water scarcity (blue line, top right, DOY: 187), a day of excessive temperature (red line, bottom left, DOY: 242) and a day of high temperature and water scarcity (black line, bottom right, DOY: 182).

The full dataset (Figure A52) supports these findings. As shown in Figure A49 the full dataset can be grouped into days which are affected by water scarcity or water scarcity in combination with high VPD (DOY: 181-213) and days which were not affected by water scarcity (DOY: 213-242). Figure 17 demonstrates that under non-stressed conditions, no significant relationship of LUE to $F_{760yield}$ was found (Figure 17 left plot), while under water scarcity the relationship is stronger but not linear (Figure 17 right plot). A further separation of the water scarcity affected data points into before and after solar noon revealed that the parabolic shape of the distribution is not solely connected to the time of day, but also observed between single days with strong variations in LUE but low variations in $F_{760yield}$ (DOY: 183, 185). Figure 18 shows the relationship of $F_{687yield}$ to LUE under normal- and water-stressed conditions. Under non-water scarcity conditions the relationship of LUE to $F_{687yield}$ shows a moderate positive correlation ($R = 0.46$), while under water scarcity the relationship is weak and negative ($R = -0.16$). When affected by water scarcity, $F_{687yield}$ is highly variable ($0.0001-0.0010 \text{ mWm}^{-2}\text{sr}^{-1}\text{nm}^{-1}$) while the LUE is relatively low ($0.01-0.025 \text{ } \mu\text{molCO}_2\text{m}^{-2}\text{s}^{-1}$).

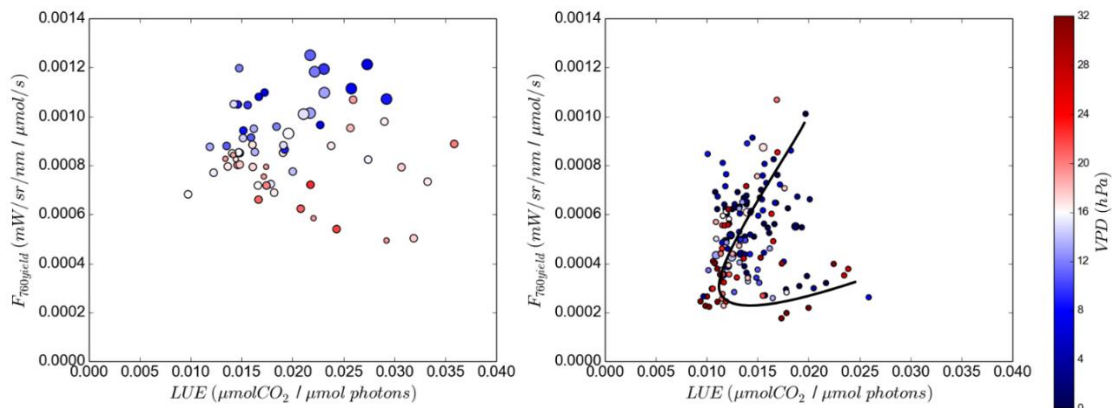


Figure 17: Relationship of LUE_{EC} derived from eddy covariance tower and $F_{760yield}$ derived from SIF-Sys under stressed- (left plot) and unstressed (right plot) environmental conditions. Data was collected in 2015 Merzenhausen within a sugar beet field. The data represent 15 clear sky measurement days collected over 2 month. Small circles indicate: $PAW < 0$ mm; medium circles: $0 \text{ mm} < PAW < 10$ mm; big circles: $PAW > 10$ mm. Color gradient indicates the vapor pressure deficit. Black line was drawn by hand to indicate the similarity to Figure 15.

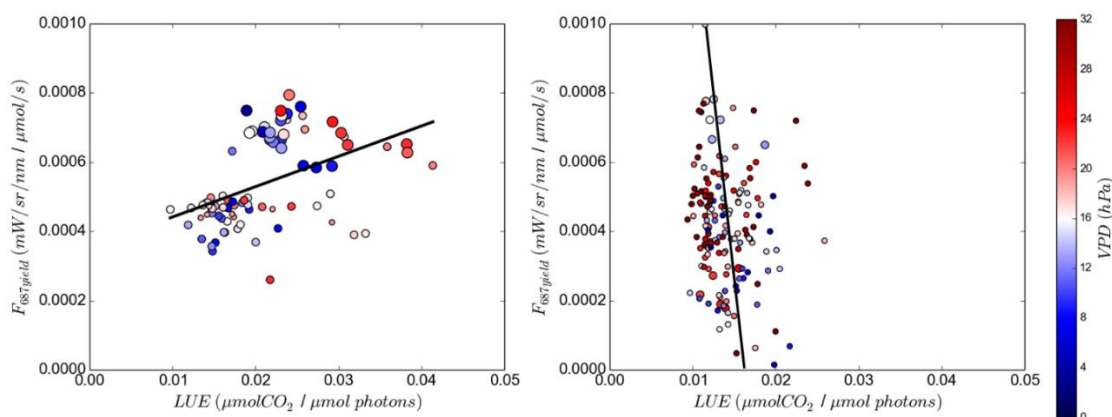


Figure 18: Relationship of LUE_{EC} derived from eddy covariance tower and $F_{687yield}$ derived from SIF-Sys under unstressed- (left plot, $R = 0.46$) and water scarcity (right plot; $R = -0.16$) conditions. Data was collected in 2015 Merzenhausen within a sugar beet field. The data represent 15 clear sky measurement days collected over 2 month. Small circles indicate: $PAW = 0$ mm; medium circles: $0 \text{ mm} < PAW < 10$ mm; big circles: $PAW > 10$ mm. Color gradient indicates the vapor pressure deficit.

5.2. Plant adaptation strategies in time and space

As described in Chapter 2, light energy absorbed by plants can be released as heat (NPQ), fluorescence (F_{tot}) or used for photosynthesis (PQ). Although none of these parameters can be measured/retrieved with currently available technique on canopy scale, proxies can be used to better understand the relationships between the three energy pathways. In this Section the PRI (as a proxy for NPQ), $F_{760\text{yield}}$ & $F_{687\text{yield}}$ (a proxy for APAR relative F_{tot} emission) and LUE (a proxy for APAR relative PQ) are used to describe their relationship under changing environmental conditions (excessive heat and water scarcity). Furthermore, fluorescence maps taken in 2012 by the *HyPlant* sensor are used to analyze and compare spatiotemporal changes of EVI, F_{760} , F_{687} , $F_{760\text{yield}}$ and $F_{687\text{yield}}$.

5.2.1. Limiting effects on LUE

For a better interpretation of the link between LUE, PRI and F, limiting environmental conditions like heat or water scarcity have to be described beforehand. Figure 19 describes the relationship of plant available water (PAW) to LUE and the connection to vapor pressure deficit. To reduce the noise due to diurnal fluctuations, the daily mean values (7 a.m. to 4 p.m.) of LUE, PAW and VPD were calculated for the 15 days of measurements. Lowest values of LUE were found when PAW is negative, i.e. the sugar beet has no access to soil water. With increasing available water, the LUE increases linearly, resulting in a strong positive relationship between PAW and LUE ($R = 0.8$). High VPD only results in reduced LUE when soil water is limited.

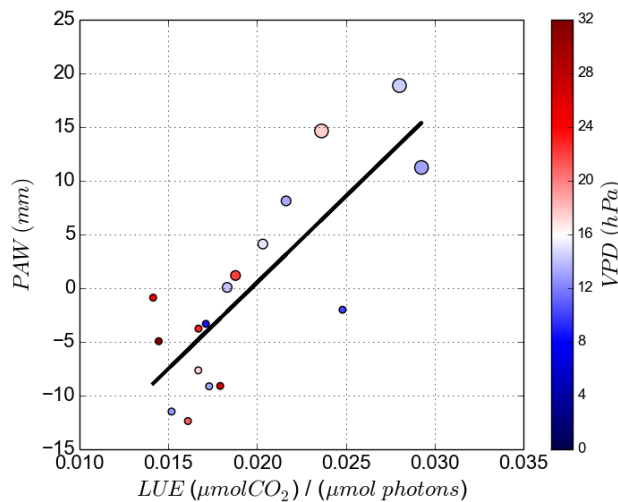


Figure 19: Light use efficiency (LUE) versus plant available water (PAW) under changing vapor pressure deficit (VPD). Data was collected within a sugar beet field, in 2015 Merzenhausen, Germany. Small circles indicate: $\text{PAW} < 0 \text{ mm}$; medium circles: $0 \text{ mm} < \text{PAW} < 10 \text{ mm}$; large circles: $\text{PAW} > 10 \text{ mm}$. The color gradient indicates the vapor pressure deficit. LUE shows a strong positive correlation with PAW. The correlation coefficient (R) is 0.8.

5.2.2. Limiting and amplifying effects on F and PRI

In this Section, the intra- and inter-daily datasets of fluorescence and PRI are described in terms of their relationship with heat and water stress.

The F_{ratio} showed a strong positive relationship with intra- and inter-daily VPD ($R = 0.63$ and 0.73 respectively), explaining 40% of the intra- and 53% of the inter-daily variation in VPD (Figure 20 and Figure 21). It has to be noted that the variance of F_{ratio} and VPD strongly increases with $PAW < 0$ mm. The PRI only showed a moderate positive relationship with intra- and inter-daily VPD ($R = 0.53$ and 0.58 respectively), explaining only 28% of the intra- and 33% of the inter-daily variation in VPD. The PRI showed a strong negative relationship with intra- and inter-daily PAW ($R = 0.74$ and 0.78 respectively), while explaining 55% of intra- and 61% of inter-daily variation in PAW. A strong positive relationship was also found between the additive yields of F_{760} and F_{687} ($F_{760yield} + F_{687yield}$) and intra- and inter-daily PAW ($R = 0.73$ and 0.82 respectively), explaining 53% of the intra- and 67% of the inter-daily variance in PAW. In general, the averaged inter-daily fluorescence and PRI shows stronger relationship towards PAW and VPD than the 30 min dataset.

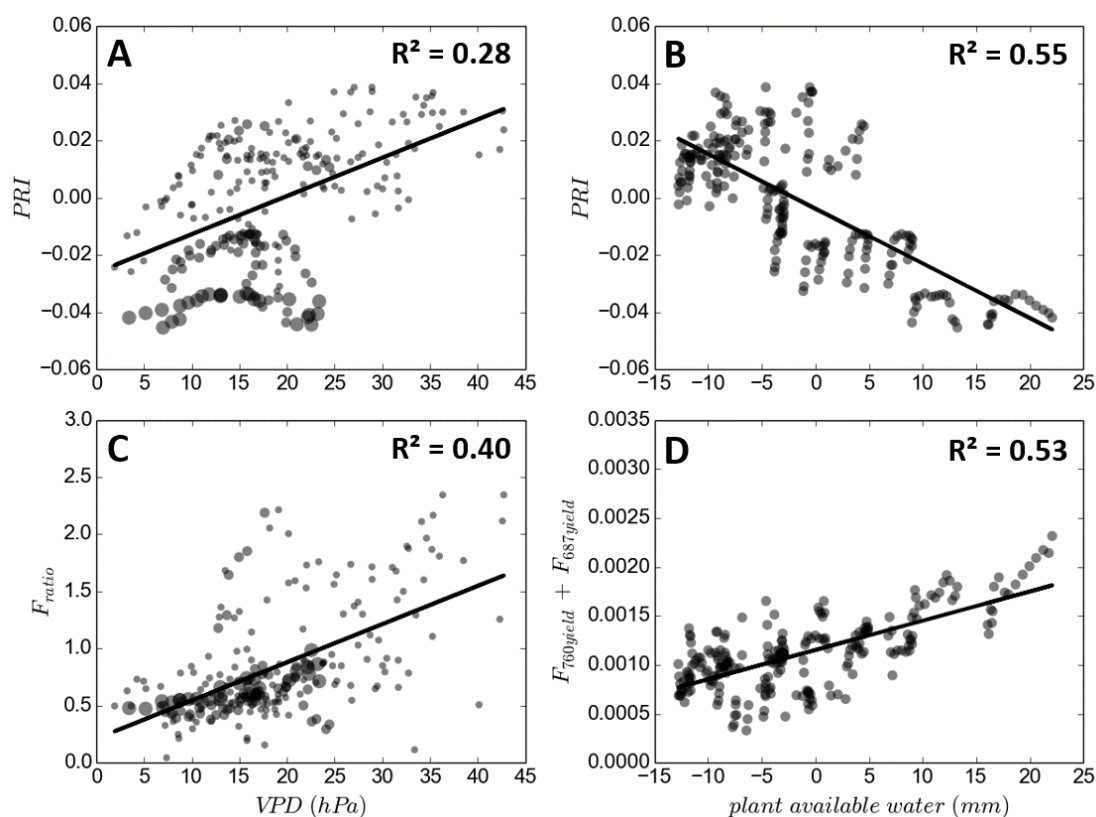


Figure 20: Relationship of 30-min PRI, F_{ratio} and $F_{760} + F_{687}$ to vapor pressure deficit (VPD) and plant available water (PAW) within a sugar beet field, in 2015 Merzenhausen, Germany. Small circles indicate: $PAW < 0$ mm; medium circles: $0 \text{ mm} < PAW < 10 \text{ mm}$; big circles: $PAW > 10 \text{ mm}$. Black line represent best linear model fit. A full overview of all tested parameters can be found in Figure A54 in the Appendix.

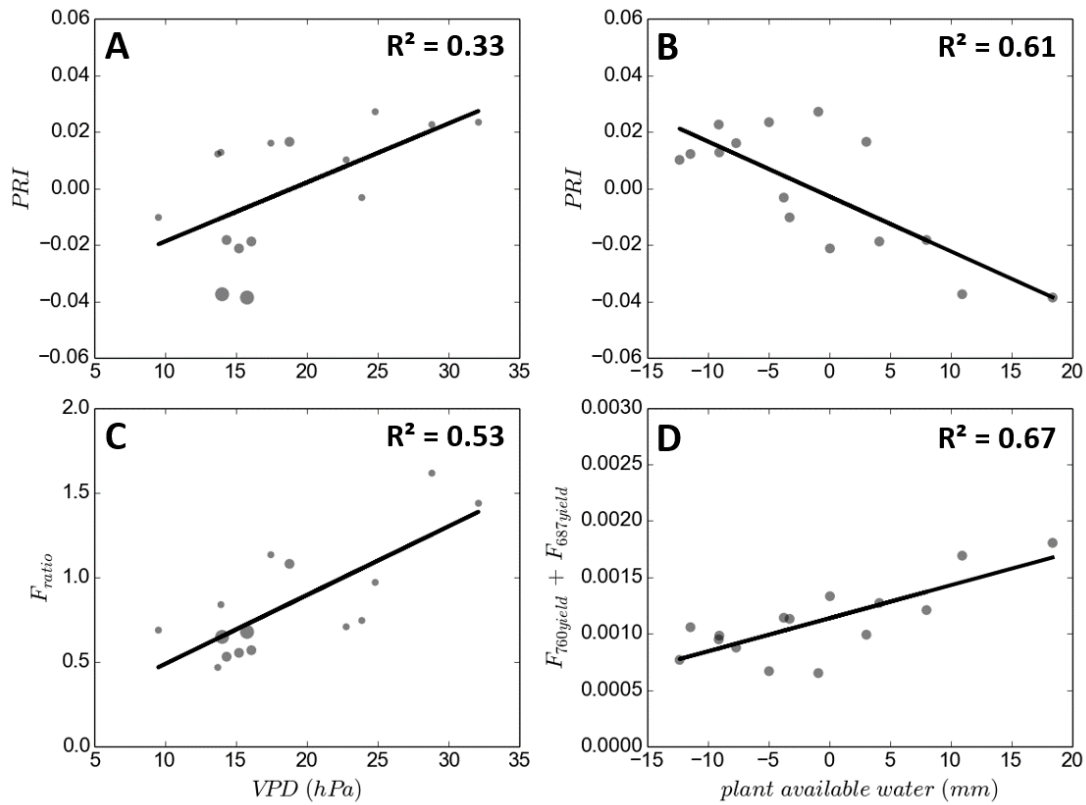


Figure 21: Relationship of daily PRI, F_{ratio} and $F_{760+687yield}$ to vapor pressure deficit (VPD) and plant available water (PAW) within a sugar beet field, in 2015 Merzenhausen, Germany. Small circles indicate: PAW < 0 mm; medium circles: 0 mm < PAW < 10 mm; big circles: PAW > 10 mm. Black line represent best linear model fit. A full overview of all tested parameters can be found in Figure A55 in the Appendix.

5.2.3. PRI, F and LUE under changing environmental conditions

In Section 5.1, results showed that the relationship of $F_{760\text{yield}}$ and $F_{687\text{yield}}$ with LUE changes with stress and time of the day. For a better understanding of the relationship between intra- and inter daily values of F_{yield} , F_{ratio} , PRI and LUE under changing environmental conditions their relationships are assessed in this Section.

Despite the finding from Section 5.1 the best fitting models describing the relationship of $F_{760\text{yield}}$ and $F_{687\text{yield}}$ with LUE are linear. While the correlation between $F_{760\text{yield}}$ and $F_{687\text{yield}}$ to LUE is moderate ($R = 0.45$ and 0.33 respectively), the additive signal of $F_{760\text{yield}}$ and $F_{687\text{yield}}$ improves the correlation coefficient to 0.52 (Figure 22 A-C). On the contrary, the daily mean variance of LUE can be very well explained by $F_{760\text{yield}}$, $F_{687\text{yield}}$ and $F_{760+687\text{yield}}$ ($R = 0.82$, $R = 0.77$ and $R = 0.9$ respectively) (Figure 21 A-C). It is worth mentioning that the additive signal of $F_{760\text{yield}}$ and $F_{687\text{yield}}$ explains more variance in LUE, than each variable alone.

The relationship between PRI (30-min and daily mean) and LUE is found to be best explained by a power law ($R^2 = 0.55$ and $R^2 = 0.76$ respectively, shown in Figure 22 and Figure 23). Interestingly, the 30-min mean variance in PRI can be best described by the F_{ratio} ($R^2 = 0.53$), while the daily mean variance in PRI shows a strong negative linear relationship towards $F_{760+687\text{yield}}$ ($R^2 = 0.87$).

The relationship of 30-min F_{ratio} and LUE (Figure 22C) shows clusters of extreme VPD and PAW values. Low VPD values for example cluster around a F_{ratio} of 0.5 with strongly varying LUE (0.010 to $0.04 \mu\text{mol CO}_2 / \mu\text{mol photons}$). At a slightly higher F_{ratio} (0.7), high VPD values with sufficient PAW aggregate along the LUE axis (0.010 - $0.040 \mu\text{mol CO}_2 / \mu\text{mol photons}$). At low LUE ($< 0.015 \mu\text{mol CO}_2 / \mu\text{mol photons}$), values are distributed along the F_{ratio} axis (0.7 - 2.4). These values are characterized by insufficient PAW and high VPD (Figure 22 D). The PRI shows a strong discrimination of PAW and a weaker discrimination of VPD (c.f. Section 5.2.3).

The relationship of F_{ratio} and PRI combines the information of both signals and show clusters of low VPD with positive PAW ($F_{\text{ratio}} < 0.6$ and $\text{PRI} < -0.01$), high VPD in combination with positive PAW ($F_{\text{ratio}} > 0.6$ and $\text{PRI} < -0.01$), low VPD with negative PAW ($F_{\text{ratio}} 0.3$ - 0.7 and $\text{PRI} 0.0$ - 0.03) and high VPD in combination with negative PAW ($F_{\text{ratio}} > 0.8$ and $\text{PRI} > 0.02$). These results are also reflected in the inter-daily dataset, but due to the much lower sample size, they are difficult to identify (c.f. Figure 23 D- F).

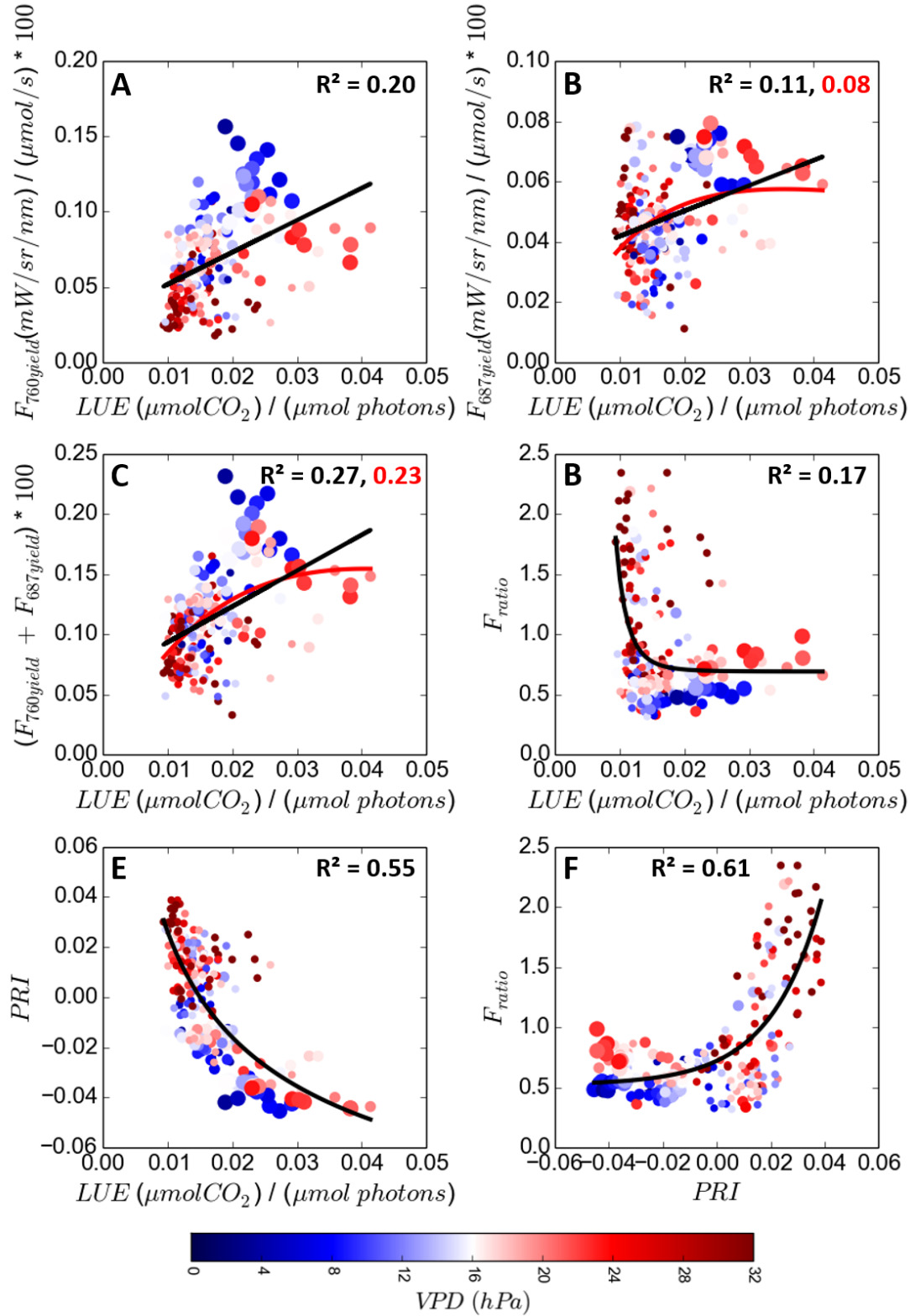


Figure 22: Relationship of 30-min $F_{760yield}$, $F_{687yield}$, $F_{760+687yield}$, F_{ratio} and PRI to LUE (A-E) and F_{ratio} to PRI (F) within a sugar beet field, in 2015 Merzenhausen, Germany. Small circles indicate: $PAW < 0$ mm; medium circles: $0 \text{ mm} < PAW < 10$ mm; big circles: $PAW > 10$ mm. Color gradient indicates the vapor pressure deficit. Black line represent best model fit, red line represent non-linear model fit of the $F_{760yield}$ and $F_{687yield}$ relationship to LUE .

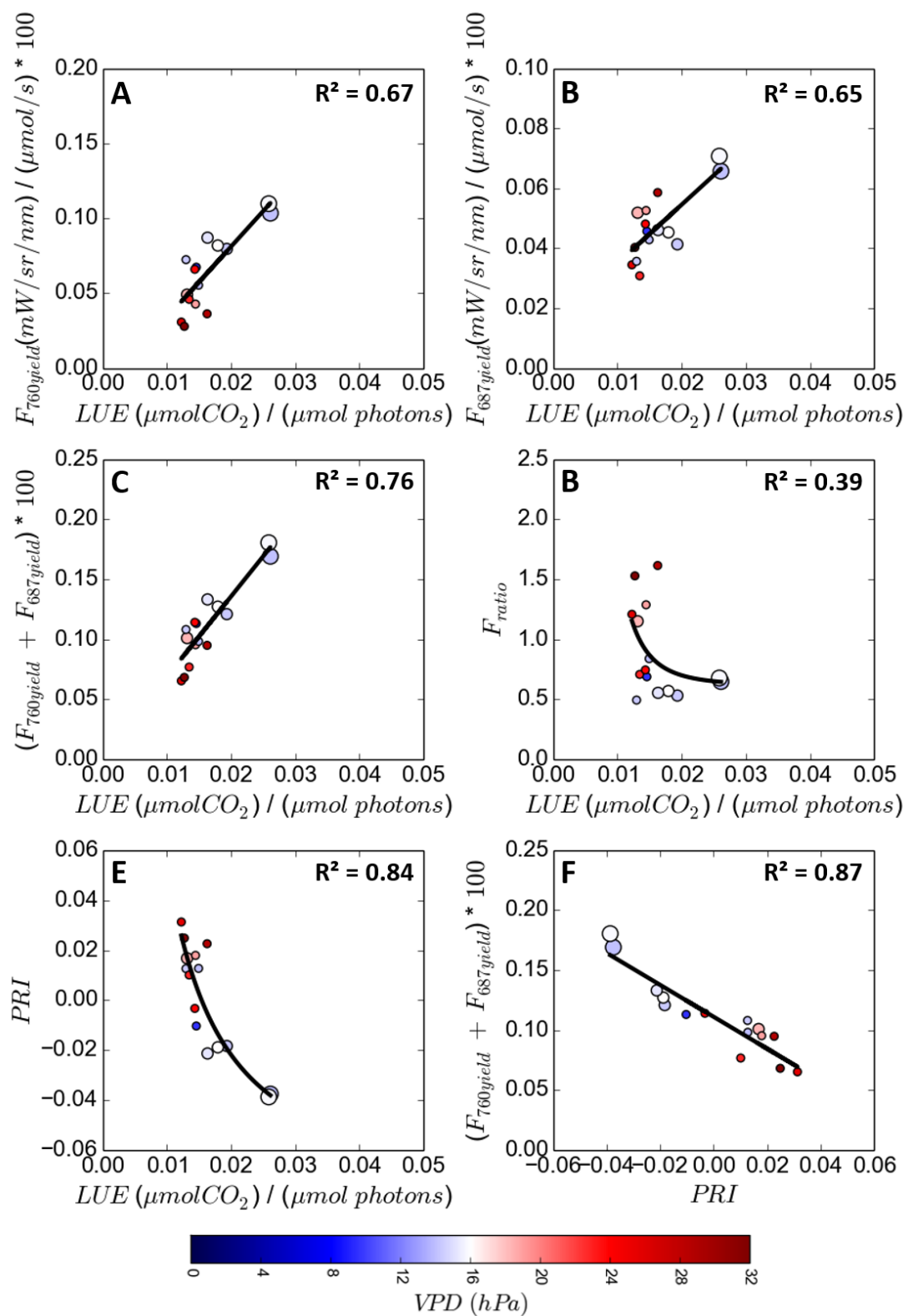


Figure 23: Relationship of daily $F_{760yield}$, $F_{687yield}$, $F_{760+687yield}$, F_{ratio} and PRI to LUE (A-E) and F_{ratio} to PRI (F) within a sugar beet field, in 2015 Merzenhausen, Germany. Small circles indicate: $PAW < 0$ mm; medium circles: $0 \text{ mm} < PAW < 10$ mm; big circles: $PAW > 10$ mm. Color gradient indicates the vapor pressure deficit. Black line represent best model fit.

5.2.4. Analyzing dynamic changes in LUE by PRI and F_{ratio}

Results of Section 5.2.2 and 5.2.3 showed the potential of PRI and F_{ratio} to describe plant short term adaptation to high VPD and water scarcity. This Section intends to evaluate whether dynamic changes in LUE can be explained by PRI and F_{ratio} . Figure 24 shows the complex non-linear relationship between intra-daily PRI, F_{ratio} , and LUE under changing environmental conditions (3D animation: http://gop.meteo.uni-koeln.de/~swieneke/3D_plot_F_ratio_30min.gif). The color gradient describes the strength of VPD, the size of the circles indicates PAW. As in the previous Figures, the size of the circles reflects PAW.

LUE is lowest when VPD is high and water not accessible to the sugar beet. Under these conditions, PRI and F_{ratio} are highest. With increasing water availability, LUE increases while PRI and F_{ratio} decrease, with F_{ratio} presenting higher sensitivity to low LUE values and PRI a high sensitivity to medium LUE values. PRI and F_{ratio} are less sensitive to highest values of LUE. This relationship results in a helix shaped curve. It must be noted that especially in the lower range of PRI and upper range of F_{ratio} several outliers with high LUE values occur.

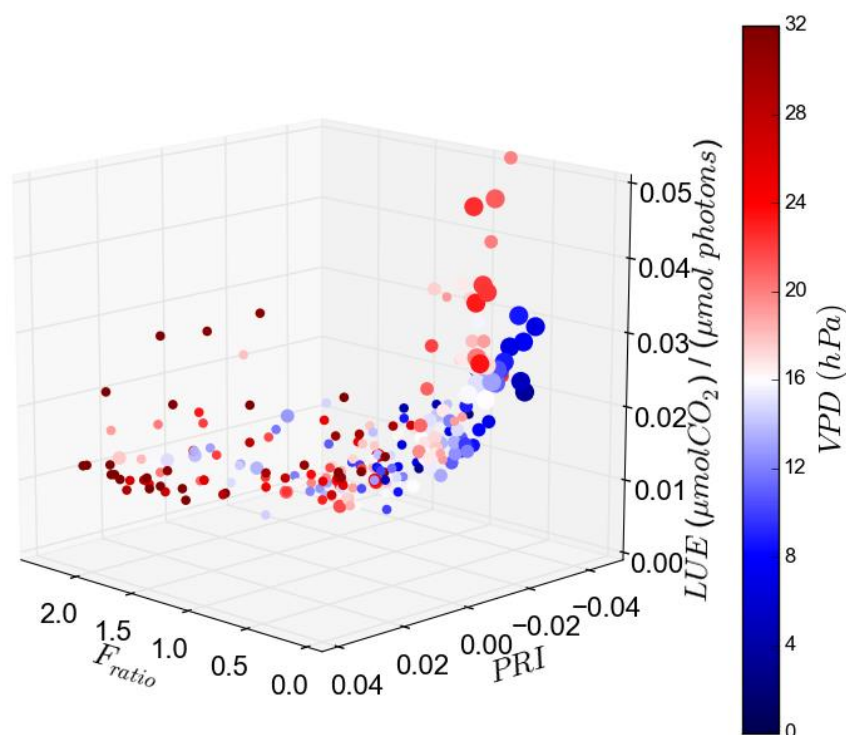


Figure 24: 3 Dimensional plot of intra-daily F_{ratio} , PRI and LUE relationship under changing plant available water (PAW) and vapor pressure deficit (VPD) within a sugar beet field, in 2015 Merzenhausen, Germany. Small circles indicate: $PAW < 0$ mm; medium circles: $0 \text{ mm} < PAW < 10$ mm; big circles: $PAW > 10$ mm. Color gradient indicates the strength of the VPD.

5.2.5. Analyzing intra-daily changes in LUE by PRI and F_{yield}

Results of Section 5.2.2 and 5.2.3 showed that in contrast to the intra-daily dataset, the inter-daily F_{yield} has a strong relationship with LUE. The Section intends to evaluate if inter-daily changes in LUE can be better explained by a combination of PRI and F_{ratio} than sole PRI. Figure 25 shows the non-linear relationship of inter-daily PRI, $F_{760\text{yield}+687\text{yield}}$, and LUE under changing environmental conditions (3D animation: http://gop.meteo.uni-koeln.de/~swieneke/3D_plot_interdaily.gif). The color gradient describes the strength of VPD, the size of the circles indicates PAW (small PAW < 0mm, medium 0 < PAW < 10mm, big PAW > 10mm). The black lines indicate the least-squares regression model describing best the relationship between PRI and F_{ratio} with LUE.

The lowest values of LUE correspond to high values of PRI and low values of $F_{760\text{yield}+687\text{yield}}$, while the highest values of LUE correspond to low values of PRI and high values of $F_{760\text{yield}+687\text{yield}}$. The best fitting non-linear regression model (c.f. Eqs. 42) explains 89% ($R^2 = 0.89$) of the variability in LUE, which is slightly higher than the R^2 (0.84) for the PRI to LUE relationship found in Section 5.2.3. This model is used to calculate inter-daily and spatial GPP_{MR} (c.f. Sections 4.2.4 and 5.5.4).

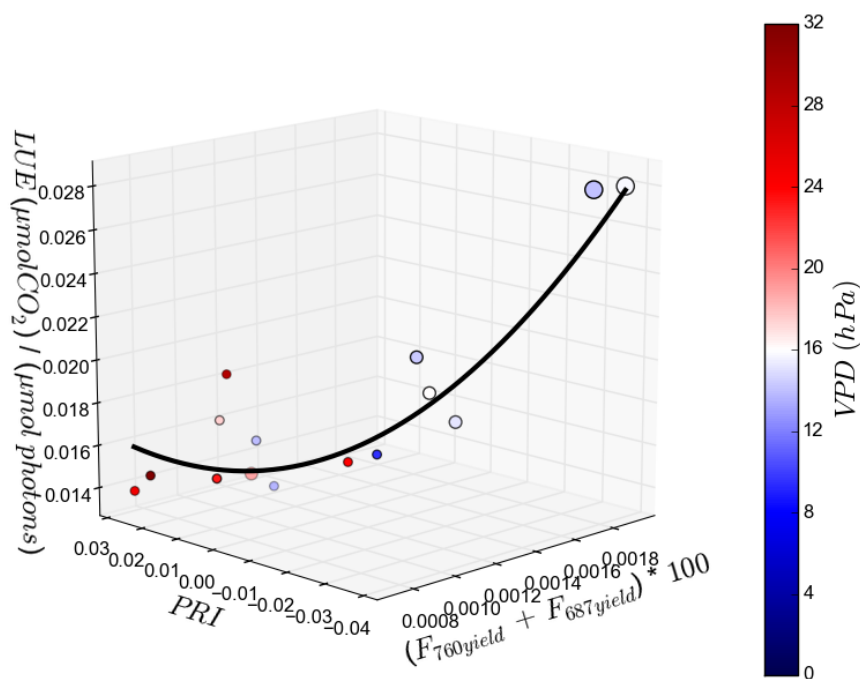


Figure 25: 3 Dimensional plot of the inter-daily $F_{760+687\text{yield}}$, PRI and LUE relationship under changing plant available water (PAW) and vapor pressure deficit (VPD) within a sugar beet field, in 2015 Merzenhausen, Germany. Small circles indicate: PAW < 0 mm; medium circles: 0 mm < PAW < 10 mm; big circles: PAW > 10mm. Color gradient indicates the strength of the VPD.

5.2.6. Spatiotemporal dynamics of F_{760} , F_{687} and their ratio

HyPlant's first fluorescence maps demonstrating diurnal changes in both fluorescence peaks are shown in Figure 26. Maps of F_{760} and F_{687} show the highest fluorescence values during solar noon and lower values in the morning and afternoon. The highest values of F_{760} and F_{687} were measured within the sugar beet fields and especially in the field centers. The F_{760} maps show spatial patterns similar to the reflectance-based EVI, with a gradient of F_{760} values from the field borders to the field center. The F_{687} maps are noisier and, for most fields, present lower (around twofold) values than average F_{760} , which is in agreement with findings by Rossini et al. (2016) who found that for various plant species red fluorescence values are lower than far-red fluorescence values. In contrast, during solar noon F_{687} in sugar beet field B and rapeseed field C show higher values than F_{760} , consequently resulting in a positive F_{ratio} (Figure 27). In general, sugar beet field B shows higher heterogeneity than sugar beet fields D to H. A fundamental difference can be seen in all maize fields, where F_{760} and F_{687} values are very low and stable over the day, while the high EVI indicate a dense canopy structure (Figure 26).

Figure 27 shows the ratio between red and far-red fluorescence (F_{ratio}). Highest values of F_{ratio} are found in parts of sugar beet field B where plants undergo a severe drought stress due to low water holding capacity of the gravely soil, originating from sediments of a fossil river bed of the Rur river (Rudolph et al., 2015; Weihermüller et al., 2007). Pictures in Figure 28 show stressed and less stressed sugar beet plants located in field B. The sugar beet affected by strong water stress were located in the lower left corner, where high F_{ratio} values were observed, while the lower stressed sugar beet plants were located in the field center, where lower F_{ratio} values were observed.

All rapeseed fields, which were in early growing stage at the time of the campaign, show increased F_{ratio} values, while the maize fields, which were in late growing stage, showed lowest F_{ratio} values. The F_{ratio} in sugar beet field B is highest during noon, while F_{ratio} in the rapeseed fields reaches maximum values in the afternoon. Sugar beet fields D, E, F, G and H show little change in the F_{ratio} except for areas with low EVI where plants again suffer from severe drought stress (eastern field boarder of D, E and G, Figure 27).

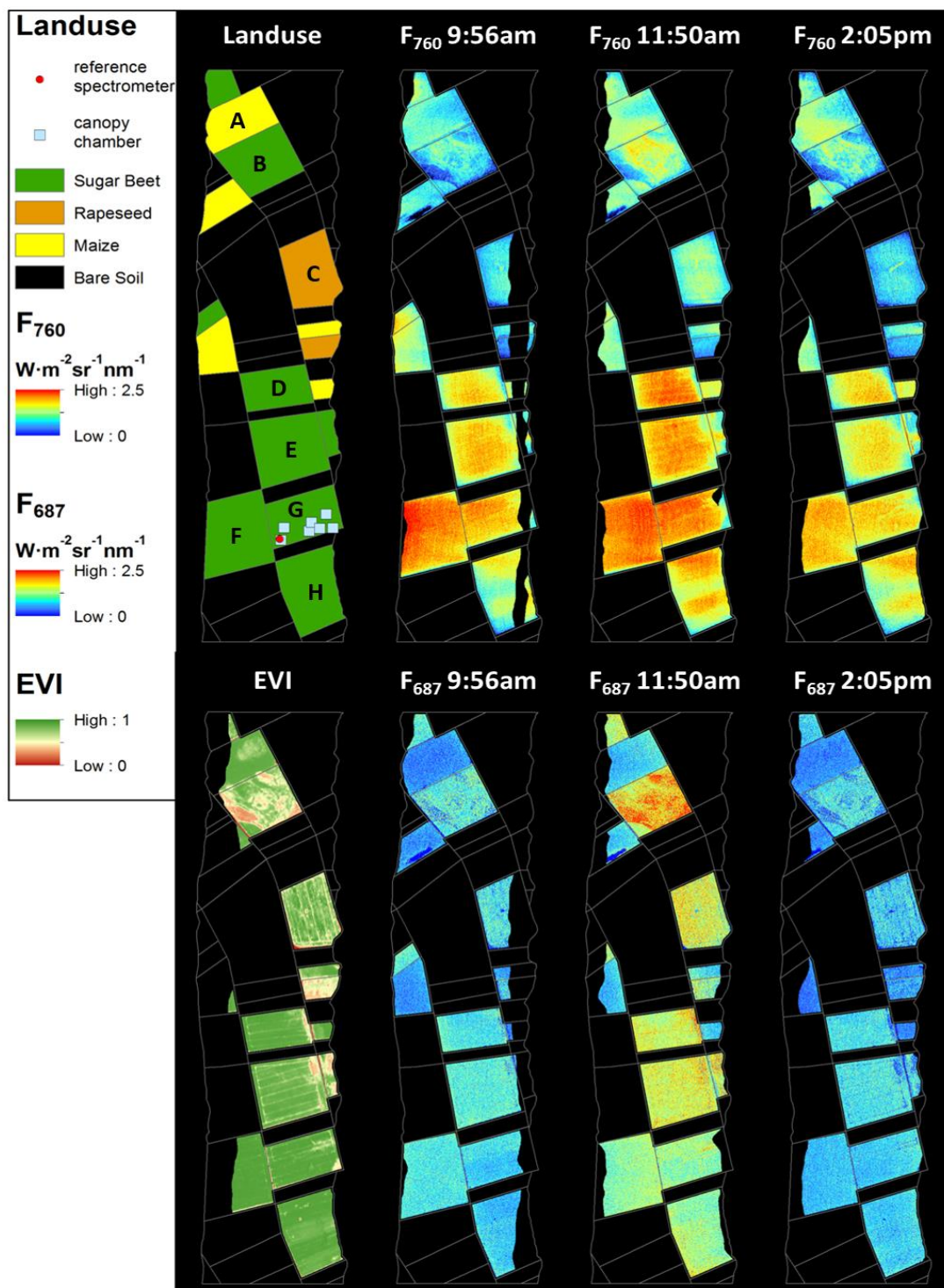


Figure 26: Maps of fluorescence at 760 nm (F_{760}) and 687 nm (F_{687}) recorded at 9:56 a.m., 11:50 a.m. and 2:05 p.m. on 23 of August 2012, Selhausen, Germany. Only the F_{760} maps were validated with ground measurements. Upper left map shows the land use of the flight line, the position of the reference spectrometer (MSS) and the location of the canopy chambers used to derive GPP_{cc} . Lower left map shows the enhanced vegetation index (EVI).

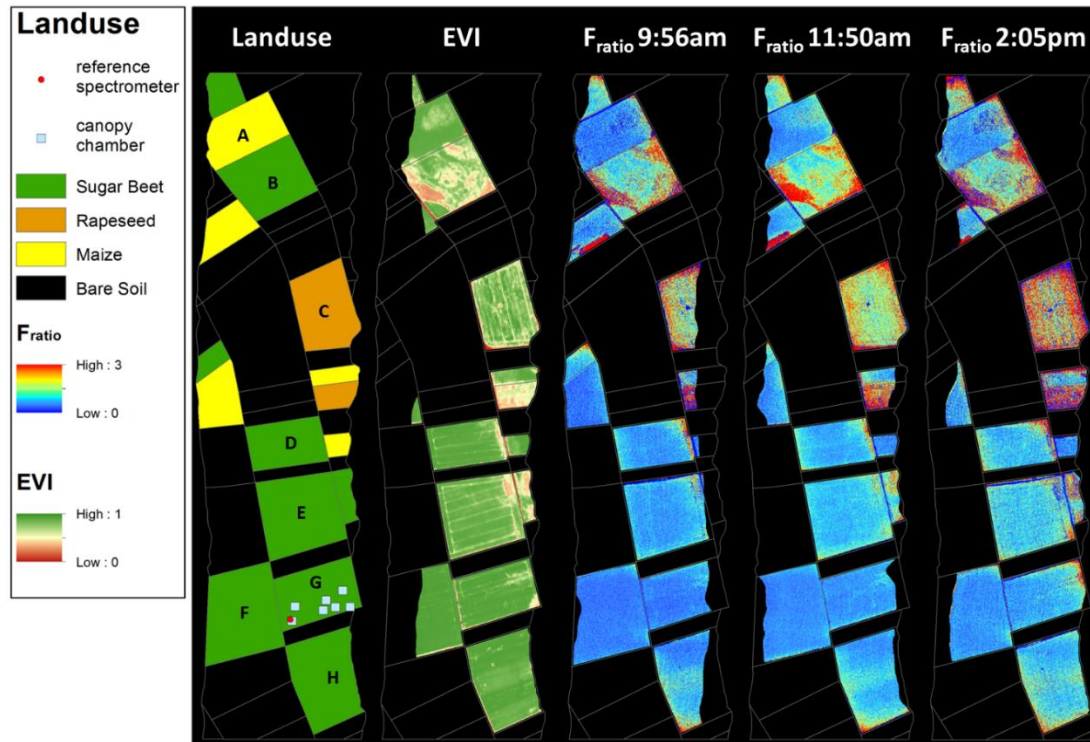


Figure 27: Maps of F_{687} to F_{760} ratio (F_{ratio}) calculated for 9:56 a.m., 11:50 a.m. and 2:05 p.m. on 23 of August in 2012 Selhausen, Germany. Left map shows the land use of the flight line, the position of the reference spectrometer (MSS) and the location of the canopy chambers used to derive GPP_{cc} . The map second from the left shows the enhanced vegetation index (EVI).



Figure 28: Left picture shows less stressed sugar beet in the center of field B. Right picture shows sugar beet under severe water stress located in the west corner of field B. Both pictures were taken on the 23. August 2012 around solar noon.

Source: Alexander Damm

5.3. Fluorescence measurement uncertainty

As described in Section 3.3.1, a novel uncertainty estimation method was implemented with the *SIF-Sys*. Because of their different magnitudes and for better comparability, the absolute error of the F_{760} and F_{687} iFLD retrieval was recalculated to relative error (Figure 29 and Figure 30). The cross markers represent the relative error of each measurement, while the red line describes the relative error of the 30-min average. The variance of the F_{760} and F_{687} error is strongest during the first week (DOY 182 to 187), but reduces during the measurement campaign (discussed in Section 6.7). The 30-min averaged F_{760} error is close to zero, with a small underestimation (from -0.7 up to -9.1% daily average error), over the whole measurement period. However, the 30-min average of the F_{687} error shows an offset with a strong overestimation (up to 64% daily average error), especially at the beginning of the measurement campaign (DOY: 182 to 198). Like the random error, the systematic error is reduced during the process of the measurement campaign. F_{760} and F_{687} were corrected by subtracting the 30-min average of the variance (red line in Figure 29 and Figure 30) from the absolute F_{760} and F_{687} values. Resulting diurnal fluorescence is shown in Figure A50 and Figure A51 in the Appendix.

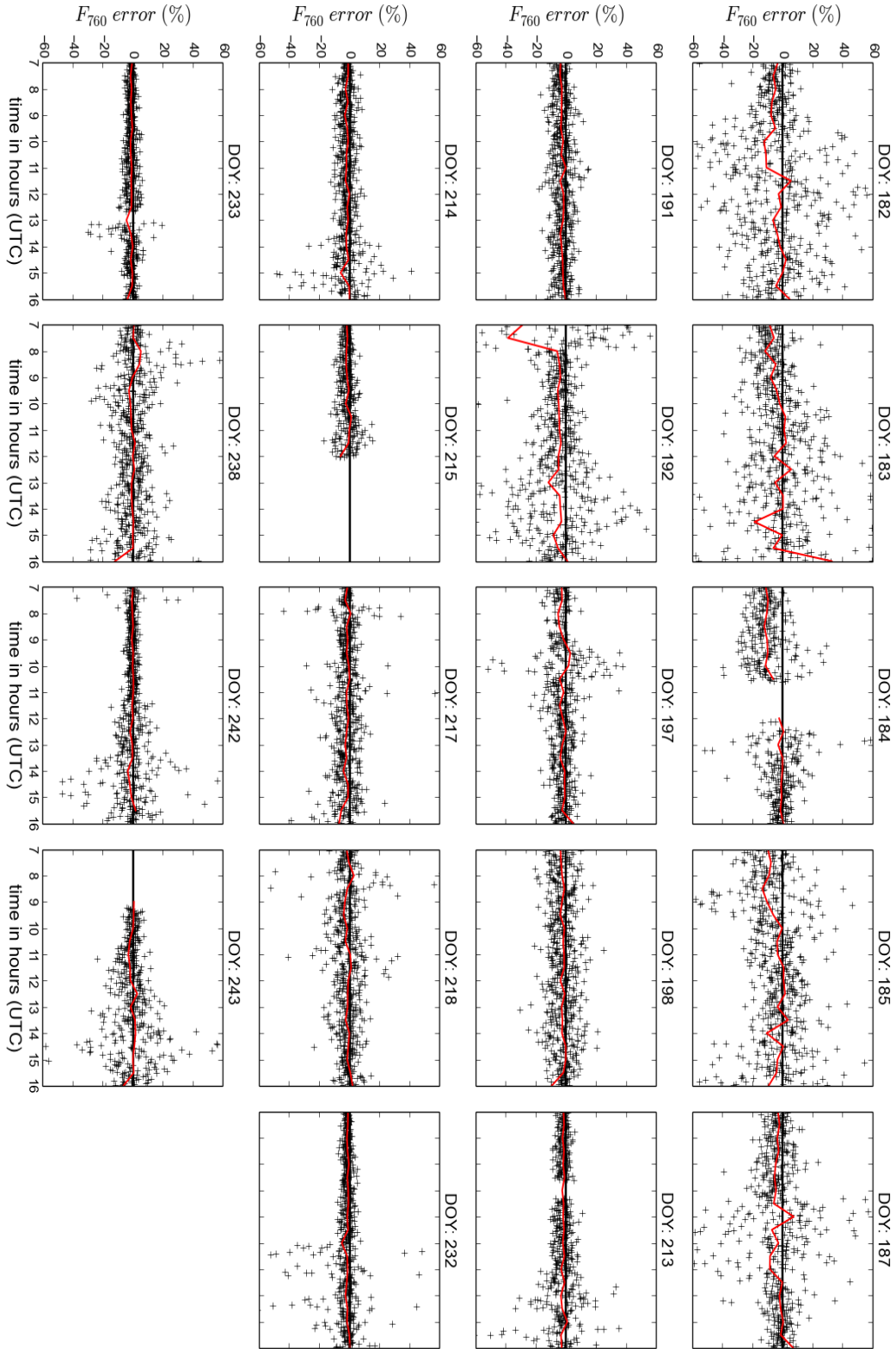


Figure 29: Relative error of F_{760} measurements estimated from LED reference light. Crosses symbolize measurements, while the red line represent the 30 minute average. Measurements were taken within a sugar beet field in 2015 Merzenhausen, Germany.

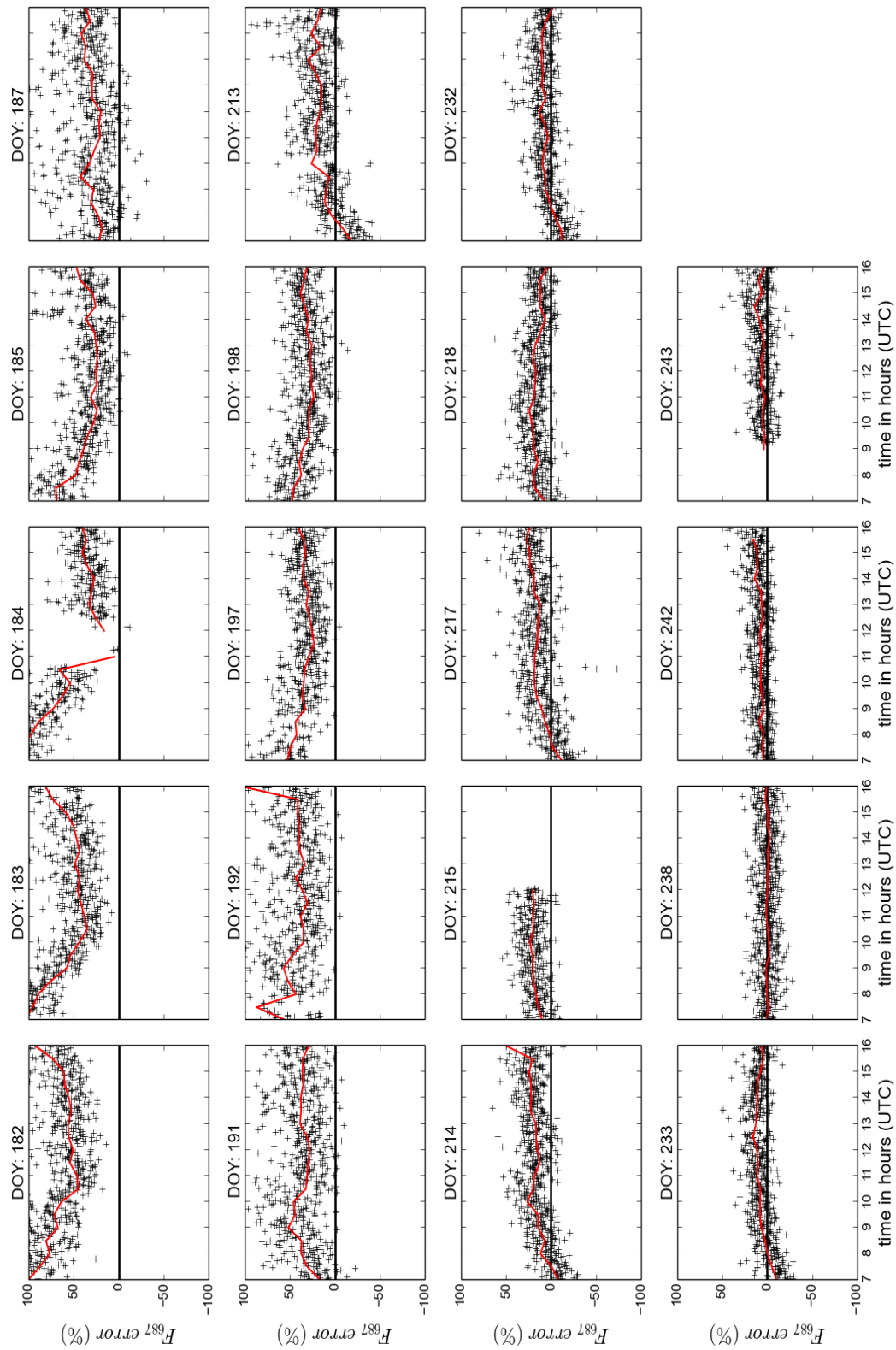


Figure 30: Relative error of F_{687} measurements estimated from LED reference light. Crosses symbolize measurements, while the red line represent the 30 minute average. Measurements were taken within a sugar beet field in 2015 Merzenhausen, Germany.

5.4. The correlation between GPP and F

Based on the assumption that F_{760} is not only related to the absorbed radiation (APAR), but also to the LUE, GPP should be predictable by F_{760} . Results show that intra-, inter-daily and spatially-averaged GPP strongly correlate with F_{760} ($R = 0.56, 0.71, 0.85$ respectively, shown in Figure 31). The intra-daily regression (Figure 31 A) presents the highest variation in the relationship between GPP to F_{760} , while the spatiotemporal regression (Figure 31 C) shows a relative low variance. This implies that with increased smoothing (intra- to inter-daily and plot size to field average) the relationship between GPP and F_{760} strengthens. The regression models used here are described in Section 4.2.2 and further used for the estimation of GPP by F_{760} in Sections 5.5.2 and 5.6.2.

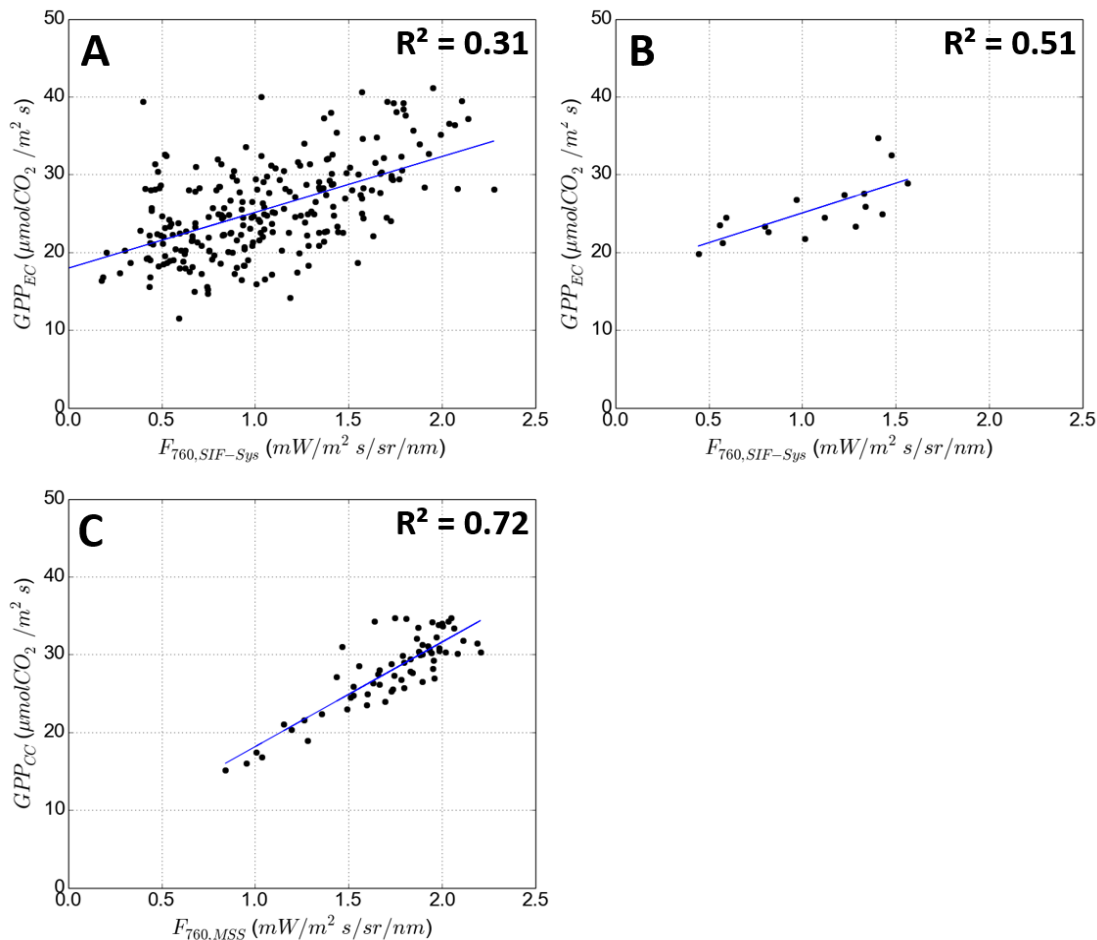


Figure 31: Relationship of intra- (A), inter-daily (B) and spatiotemporal GPP to F_{760} . GPP_{EC} was derived from an eddy covariance tower and $F_{760, SIF-Sys}$ from the SIF-Sys spectrometer in 2015, Merzenhausen. GPP_{CC} was derived from field averaged canopy chamber measurements and $F_{760, MSS}$ from the MSS spectrometer in 2012, Selhausen. The blue line shows the intercept and slope of the regression model. The model best describing the intra-daily relationship is $GPP_F = 10.5 + 12.9 * F_{760, SIF-Sys}$. The model best describing the inter-daily relationship is $GPP_F = 15 + 9.7 * F_{760, SIF-Sys}$. The model best describing the spatiotemporal relationship is $GPP_F = 4.72 + 13.44 * F_{760, MSS}$.

5.5. Intra- and inter-daily estimation of GPP

In this Section, GPP is calculated from four different models described in Section 4.2. The color gradient of the figures of this Section describes the strength of vapor pressure deficit (VPD), the size of the circles indicate the plant available water (PAW). Small circles represent a PAW lower than 0 mm, medium circles a PAW between 0 mm and 10 mm and the biggest circles correspond to a PAW higher than 10 mm. Results are shown for the full intra- and inter-daily dataset. The black lines indicate the identity line, while the blue line describes the correlation line between estimated and EC derived GPP. All models provide a statistically significant fit at the 95% confidence level. For a better interpretation of model estimates under environmental stress, the intra-daily dataset was separated between low environmental stress (VPD < 14 hPa and PAW > 0 mm) and stronger environmental stress (VPD ≥ 14 hPa and PAW ≤ 0 mm). Because of the lack of data points the inter-daily dataset was analyzed in its full size.

5.5.1. Using reflectance based vegetation indices

Five different VIs (NDVI, EVI, PRI, MCARI2I and TCARI) were used to find the best representation for fAPAR used by the LUE model (c.f. Section 4.2.1). Best results were found for the enhanced vegetation Index (EVI).

Figure 32 A shows EVI based modeled and EC derived GPP for the 30-min Merzenhausen dataset. Results show that all data points are distributed along the identity line with a stronger variance at medium level GPP and an underestimation of GPP_{EC} in the upper data range. This results in an overall underestimation of GPP_{EC} (BIAS = -6.83 %). The coefficient of determination (R^2) provides a moderate result of 0.48 while the root mean square error (RMSE) is relatively high (5.25 $\mu\text{mol CO}_2/\text{m}^2\text{s}$, i.e. 20.74 %). The differentiation of the dataset resulted in an improved estimation of GPP_{EVI} under low environmental stress factors ($R^2 = 0.57$, BIAS = -6.18 % and RMSE = 4.69 $\mu\text{mol CO}_2/\text{m}^2\text{s}$ (16.04 %)) compared to a worsened estimation of GPP_{EVI} affected by higher VPD and negative PAW ($R^2 = 0.42$, BIAS = -6.14 % and RMSE = 5.51 $\mu\text{mol CO}_2/\text{m}^2\text{s}$ (22.51 %)).

Figure 32 B shows EVI-based modeled and EC-derived GPP for the daily mean Merzenhausen dataset. With a slope of 0.69, the correlation line shows an underestimation of GPP_{EC} in the upper data range where VPD is low and PAW high. While the overall BIAS increased to -7.93 %, the RMSE decreased (2.54 $\mu\text{mol CO}_2/\text{m}^2\text{s}$ (10.07 %)) and the R^2 significantly improved (0.82) in comparison to the intra-daily analysis.

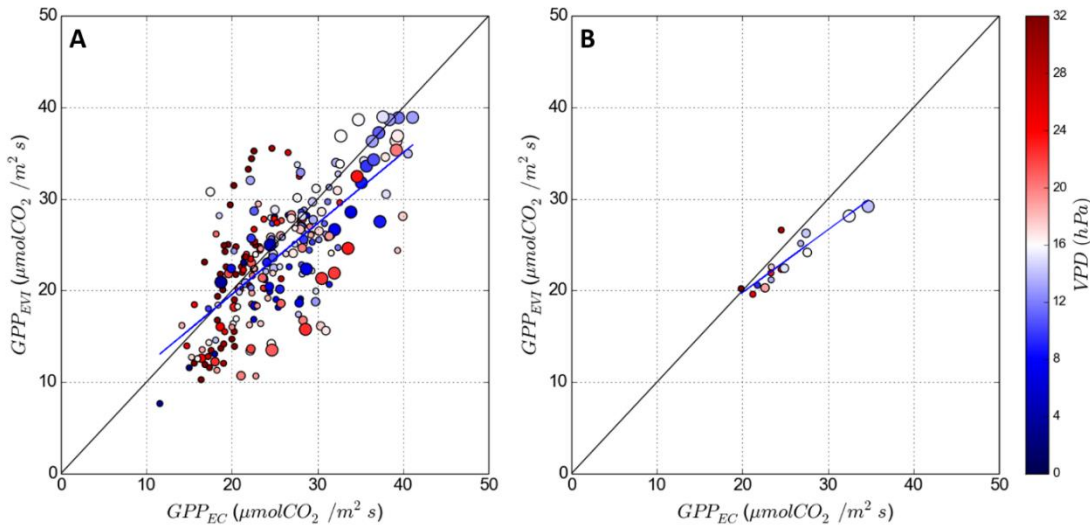


Figure 32: Scatter plot of estimated (GPP_{EVI}) and measured (GPP_{EC}) intra- and inter-daily gross primary production (GPP) of sugar beet. Points represent 30-min (A) and daily (B) average values of 15 days under clear sky conditions between July and August 2015, Merzenhausen. Small circles indicate: $PAW < 0$ mm; medium circles: $0 \text{ mm} < PAW < 10$ mm; big circles: $PAW > 10$ mm. Color gradient indicates the vapor pressure deficit. Modeled GPP based on Monteith LUE model driven by EVI as an estimator for $fAPAR$. For plot A the coefficient of determination (R^2) is 0.48, the overall BIAS is -6.83 %, the RMSE is $5.25 \mu\text{mol CO}_2 / \text{m}^2 \text{ s}$ (20.74 %) and the slope 0.77. For plot B the coefficient of determination (R^2) is 0.82, the overall BIAS is -7.93 %, the RMSE is $2.54 \mu\text{mol CO}_2 / \text{m}^2 \text{ s}$ (10.07 %) and the slope 0.69).

5.5.2. Using a statistical GPP-F relationship model

Based on the model best describing the relationship between F_{760} and GPP_{EC} , GPP_{F760} was estimated for the intra- and inter-daily dataset (c.f. Sections 4.2.3 and 5.4). Figure 33 A shows that modeled GPP_{F760} underestimates GPP_{EC} in the high value range, resulting in a negative BIAS of 6.55%, a slope of 0.55, a low R^2 of 0.32 and a relatively high RMSE ($5.72 \mu\text{mol CO}_2 / \text{m}^2 \text{ s}$, 22.59 %). Since a clear horizontal distribution between high and low VPD is visible, the separation of the dataset does not significantly improve the estimation of GPP_{EVI} . Under low or no stress conditions the R^2 stays at 0.32 while the BIAS turns positive (5.83 %). Under increased VPD and negative PAW, the R^2 slightly decreases to 0.3, while the BIAS is -9.2%.

Figure 33 B shows F_{760} based modeled and EC derived GPP for the daily averaged Merzenhausen dataset. Like for the intra-daily prediction of GPP_{F760} , the inter-daily prediction underestimates GPP in the high value range, where VPD is low and PAW high. In the lower value range however the inter-daily prediction performs better, resulting in a higher regression line slope (0.52) and coefficient of determination (0.52). The BIAS and the RMSE decreases to -1.73 and $2.8 \mu\text{mol CO}_2 / \text{m}^2 \text{ s}$ (11.1 %), respectively. However, an overestimation in the higher value range is still visible.

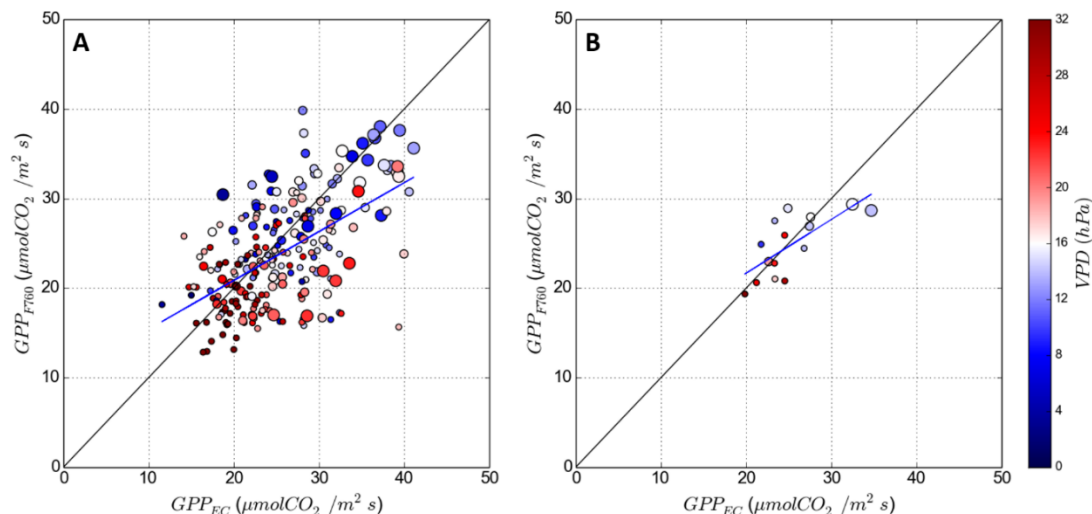


Figure 33: Scatter plot of estimated (GPP_{F760}) and measured (GPP_{EC}) intra- and inter-daily gross primary production (GPP) of sugar beet. Points represent 30-min (A) and daily (B) average values of 15 days under clear sky conditions between July and August 2015, Merzenhausen. Small circles indicate: $PAW < 0$ mm; medium circles: $0 \text{ mm} < PAW < 10$ mm; big circles: $PAW > 10$ mm. Color gradient indicates the vapor pressure deficit. Modeled GPP based on GPP-F correlation model. For plot A the coefficient of determination (R^2) is 0.32, the overall BIAS is -6.55 %, the RMSE is $5.72 \mu\text{mol CO}_2/\text{m}^2\text{s}$ (22.59 %) and the slope 0.55). For plot B the coefficient of determination (R^2) is 0.52, the BIAS is 0 %, the RMSE is $2.73 \mu\text{mol CO}_2/\text{m}^2\text{s}$ (10.82 %) and the slope 0.52).

5.5.3. Using LUE-F_{760yield} relationship model

Figure 34 A shows modeled intra-daily GPP_{Φ} based on the $F_{760yield}$ to LUE ratio approach proposed by Guanter et al. (2014) and GPP_{EC} derived from eddy-covariance measurements. Results indicate that modeled intra-daily GPP_{Φ} varies strongly around the identity line with a wider range of estimated GPP_{F760} than GPP_{EC} . While GPP_{F760} underestimates for lower plant productivity, it tends to overestimate high plant productivity, and presents an overall BIAS of 2.92%. Due to a strong accumulation of data points around 18-25 $\mu\text{mol CO}_2/\text{m}^2\text{s}$ and above the identity line, the resulting slope is 0.81. The overall coefficient of determination is with 0.29 low and the RMSE with 7.63 $\mu\text{mol CO}_2/\text{m}^2\text{s}$ (30.15 %) high. The segmentation of the dataset shows an improved R^2 (0.60), but very high BIAS (17.57 %) and RMSE (9.23 $\text{CO}_2/\text{m}^2\text{s}$ (31.56 %)) for low/none stress condition. Under higher VPD and PAW deficit the R^2 decrease to 0.19, the BIAS improves to 1.44% and the RMSE stays at 7.63 $\mu\text{mol CO}_2/\text{m}^2$.

Figure 34 B compares modeled inter-daily GPP_{Φ} with derived inter-daily GPP_{EC} . Results show that data points are distributed close to the identity line with higher variance in the medium range of GPP. The slope of the correlation line is very close to one (1.04) and the coefficient of determination is much stronger than for the intra-daily result (0.78). Interestingly, data points affected by stronger environmental stressors are closely distributed around the identity line and therefore much better represented than

in the intra-daily analysis. The overall BIAS (1.78 %) and the RMSE (2.23 $\mu\text{mol CO}_2/\text{m}^2\text{s}$ or 8.84 %) are relatively low.

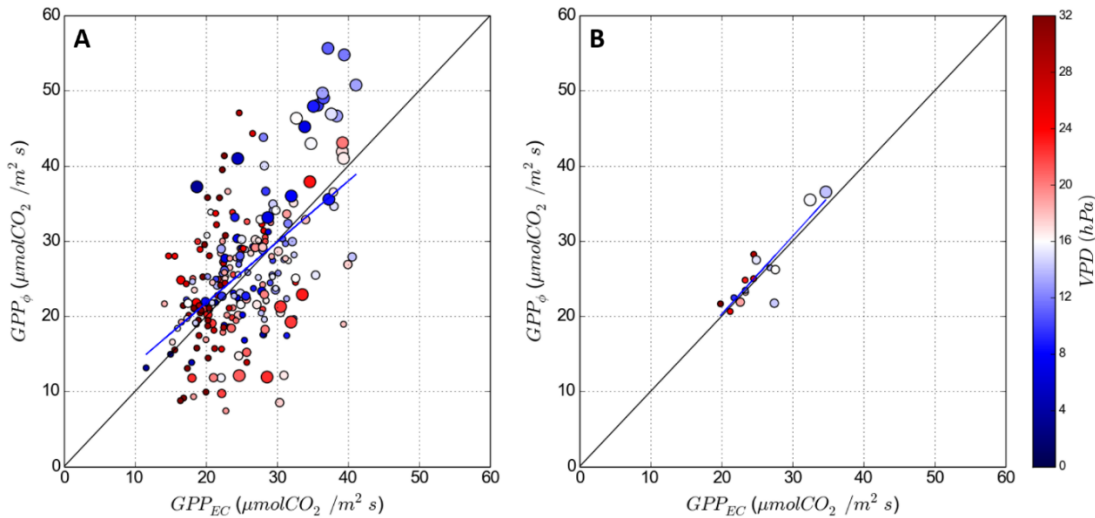


Figure 34: Scatter plot of estimated (GPP_{ϕ}) and measured (GPP_{EC}) intra- and inter-daily gross primary production (GPP) of sugar beet. Points represent 30-min (A) and daily (B) average values of 15 days under clear sky conditions between July and August 2015, Merzenhausen. Small circles indicate: $PAW < 0$ mm; medium circles: $0 \text{ mm} < PAW < 10$ mm; big circles: $PAW > 10$ mm. Color gradient indicates the vapor pressure deficit. Modeled GPP based on GPP-F correlation model. For plot A the coefficient of determination (R^2) is 0.29, the BIAS is 2.92 %, the RMSE is $7.63 \mu\text{mol CO}_2/\text{m}^2\text{s}$ (30.15 %) and the slope 0.81. For Plot B the coefficient of determination (R^2) is 0.78, the BIAS is 1.78 %, the RMSE is $2.23 \mu\text{mol CO}_2/\text{m}^2\text{s}$ (8.84 %) and the slope 1.04).

5.5.4. Using multiple regression model

Based on the best fitting non-linear multiple regression model described in Section 5.2.4 GPP_{MR} was calculated and compared with GPP_{EC} . Figure 35 A shows that data points are distributed around the identity line where low GPP values are underestimated whereas mid to high GPP values, and in particular values with low VPD, are slightly overestimated. The resulting slope is close to the identity line (0.94) and the BIAS is, with 4.34 %, relatively low. The R^2 is the highest (0.55) of all intra-daily models and the RMSE of $5.25 \mu\text{mol CO}_2/\text{m}^2\text{s}$ (20.74 %) is similar to the intra-daily GPP_{EVI} and GPP_{F760} models. GPP values affected by weak environmental stressors showed higher R^2 (0.64), a stronger positive BIAS (11.42 %) and a slight increase in RMSE ($5.39 \mu\text{mol CO}_2/\text{m}^2\text{s}$, 18.43%). Under higher VPD and PAW deficit, the R^2 decreases to 0.53, the BIAS improves to 2.62 % while the RMSE stays at $5.28 \mu\text{mol CO}_2/\text{m}^2$.

Based on the best fitting non-linear multiple regression model described in Section 4.2.4, GPP_{MR} was calculated and compared with GPP_{EC} . Figure 35 B shows that the points closely align along the identity line with a slope of 0.94 and a slight

overestimation of 4.35%. The R^2 is, with 0.79, comparatively high and the RMSE low, with $2.26 \mu\text{mol CO}_2 / \text{m}^2\text{s}$ (8.96%). Neither the VPD nor the PAW seem to have no particular effect on the estimation quality.

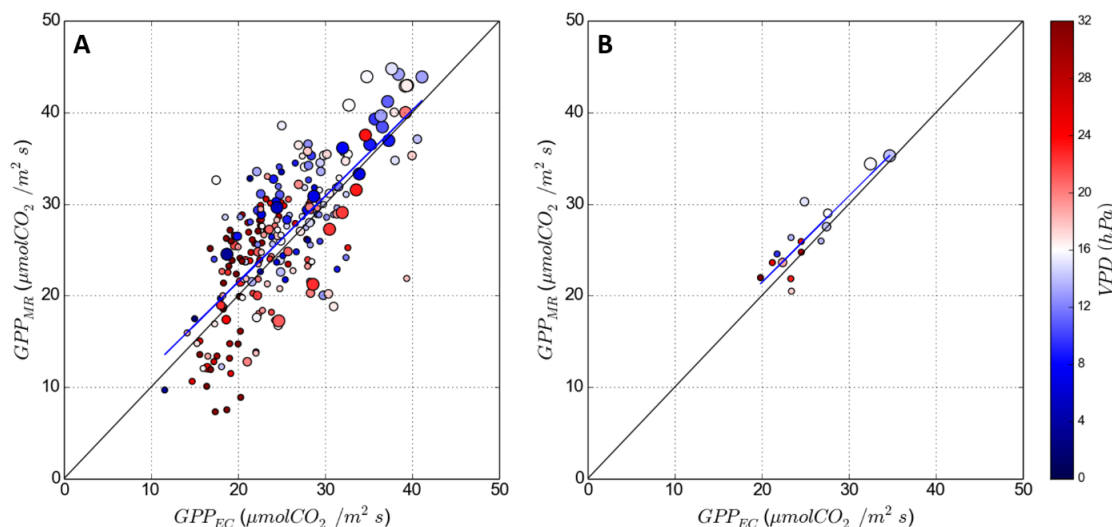


Figure 35: Scatter plots of estimated (GPP_{MR}) and measured (GPP_{EC}) intra- (A) and inter-daily (B) gross primary production (GPP) of sugar beet. Points represent 30-min (A) and daily (B) average values of 15 days under clear sky conditions between July and August 2015, Merzenhausen. Small circles indicate: $PAW < 0 \text{ mm}$; medium circles: $0 \text{ mm} < PAW < 10 \text{ mm}$; big circles: $PAW > 10 \text{ mm}$. Color gradient indicates the vapor pressure deficit. Modeled GPP based on GPP-F correlation model. For plot A the coefficient of determination (R^2) is 0.55, the BIAS is 4.34 %, the RMSE is $5.25 \mu\text{mol CO}_2 / \text{m}^2\text{s}$ (20.74 %) and the slope 0.94). For plot B the coefficient of determination (R^2) is 0.79, the BIAS is 4.35 %, the RMSE is $2.26 \mu\text{mol CO}_2 / \text{m}^2\text{s}$ (8.96 %) and the slope 0.95).

5.5.5. Summary of intra- and inter-daily GPP estimation

Table 4 shows an overview of intra-daily estimated GPP relative to the eddy-covariance derived GPP. The multiple regression model showed the highest coefficient of determination ($R^2 = 0.55$) and a correlation line slope close to one (0.94). The root mean square error (RMSE) and the relative RMSE are lowest for the GPP_{EVI} and GPP_{MR} model: $5.25 \mu\text{mol CO}_2 / \text{m}^2\text{s}$ and 20.74 %, respectively. All models tend to perform better for GPP values during lower VPD and sufficient PAW conditions (Figure 32, Figure 33, Figure 34 and Figure 35). Except of the multiple regression model, all models perform worse for GPP values affected by higher VPD values and negative PAW. Altogether, the GPP_{MR} model performed best for the intra-daily dataset.

Table 4: Results of intra-daily estimation of GPP from four different models (GPP_{EVI} , GPP_{F760} , GPP_{ϕ} and GPP_{MR}) correlated with eddy-covariance derived GPP_{EC} . Best results are marked in bold numbers.

intra-daily models				
	GPP_{EVI}	GPP_{F760}	GPP_{ϕ}	GPP_{MR}
R^2	0.48	0.32	0.29	0.55
slope	0.77	0.55	0.81	0.94
RMSE ($\mu\text{mol CO}_2 / \text{m}^2\text{s}$)	5.25	5.72	7.63	5.25
relative RMSE (%)	20.74	22.59	30.15	20.74
BIAS (%)	-6.83	-6.55	2.92	4.34
Mean uncertainty (%)	10.22	8.28	46.63	8.27

Figure 36 summarizes the 15 diurnal cycles of estimated and EC derived GPP and their respective coefficient of determination, where the colored area defines the uncertainty of the respective models. In most days (9 out of 15) the GPP_{EVI} and GPP_{MR} perform well with an R^2 at least over 0.5 and relative low uncertainty. However, five days (DOY: 181, 183, 184, 184, 185) in the first week of the measurement campaign coincide with the 2015 summer heat wave, showing lower R^2 and higher uncertainty than other days. The models estimating GPP_{F760} and GPP_{ϕ} perform worse than the GPP_{EVI} and GPP_{MR} models. Particularly noticeable is the high uncertainty of GPP_{ϕ} and the identical R^2 values for GPP_{F760} and GPP_{ϕ} , which will be further explained in Section 6.4.

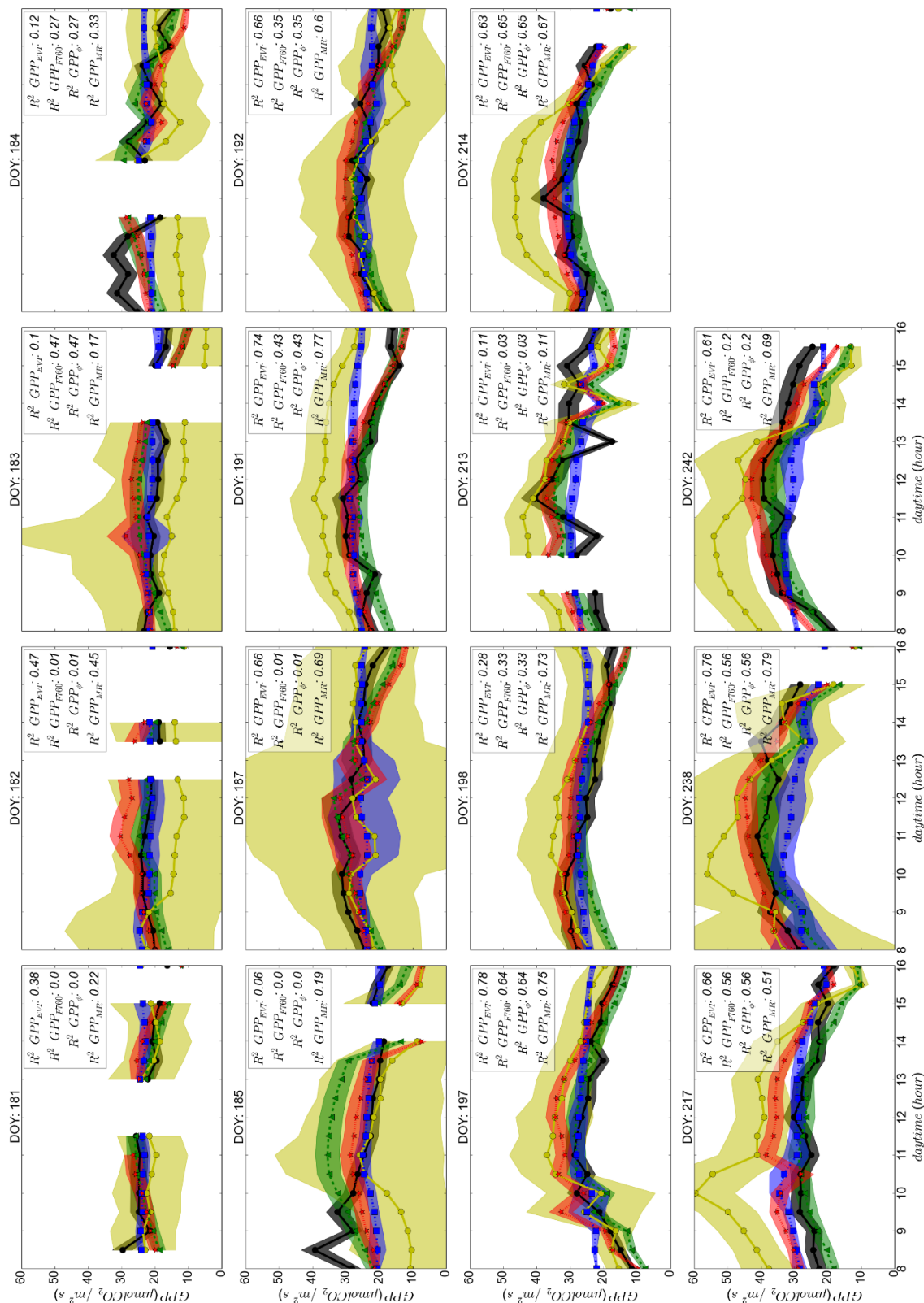


Figure 36: Diurnal cycle of estimated GPP_{EVI} (green dashed line and triangles), GPP_{F760} (red dotted line and stars), GPP_{ϕ} (yellow solid line and cycles), GPP_{MR} (blue dotted line and squares) and reference GPP_{EC} (black solid line and cycles) for sugar beet in 2015 Merzenhausen. Shaded areas illustrate the respective model uncertainty.

An overview of inter-daily estimated GPP relative to the eddy-covariance derived GPP is shown in Table 5. The GPP_{EVI} model showed the highest coefficient of determination ($R^2 = 0.82$), closely followed by the GPP_{MR} (0.79) and GPP_{Φ} (0.78) model. All models present low RMSE and relative RMSE. Interestingly, the GPP_{Φ} model, which performed as the worst predictor of the intra-daily dataset, shows for the inter-daily dataset the best results, with RMSE of $2.23 \mu\text{mol CO}_2 / \text{m}^2$ (8.84 %) and a slope close to one (1.04), closely followed by the GPP_{MR} model with an RMSE of $2.26 \mu\text{mol CO}_2 / \text{m}^2$ (8.96%) and an slope of 0.95. In general, the values of VPD and PAW did not significantly influence the performance of the model.

Table 5: Results of inter-daily estimation of GPP from four different models (GPP_{EVI} , GPP_{F760} , GPP_{Φ} and GPP_{MR}) relative to eddy-covariance derived GPP_{EC} . Best results are marked in bold numbers.

inter-daily models				
	GPP_{EVI}	GPP_{F760}	GPP_{Φ}	GPP_{MR}
R^2	0.82	0.52	0.78	0.79
slope	0.69	0.60	1.04	0.95
RMSE ($\mu\text{mol CO}_2 / \text{m}^2\text{s}$)	2.54	2.80	2.23	2.26
relative RMSE (%)	10.07	11.1	8.84	8.96
BIAS (%)	-7.93	-1.73	1.78	4.35
Mean uncertainty (%)	10.11	16.16	38.77	9.51

Figure 37 shows the daily relative deviation of modeled GPP from GPP_{EC} . As shown in Table 5 the RMSE is similar for all models with best results for GPP_{Φ} . The relatively strong negative BIAS of GPP_{EVI} (-7.93%), indicates a systematic underestimation of the reflectance based model. The GPP_{Φ} and the GPP_{MR} model showed a small overestimation with 1.78 % and 4.35 % respectively. Figure 38 shows the relative model uncertainty. The highest uncertainty is given by the GPP_{Φ} model (38.77 %), followed by the GPP_{F760} model (16.16 %) and the GPP_{EVI} and GPP_{MR} model with 10.11 % and 9.51 % respectively. In general, the uncertainty is highest (especially for the GPP_{Φ} model) in the first week of measurements (DOY: 181-187), which is very likely related to higher temperatures in the measurement system.

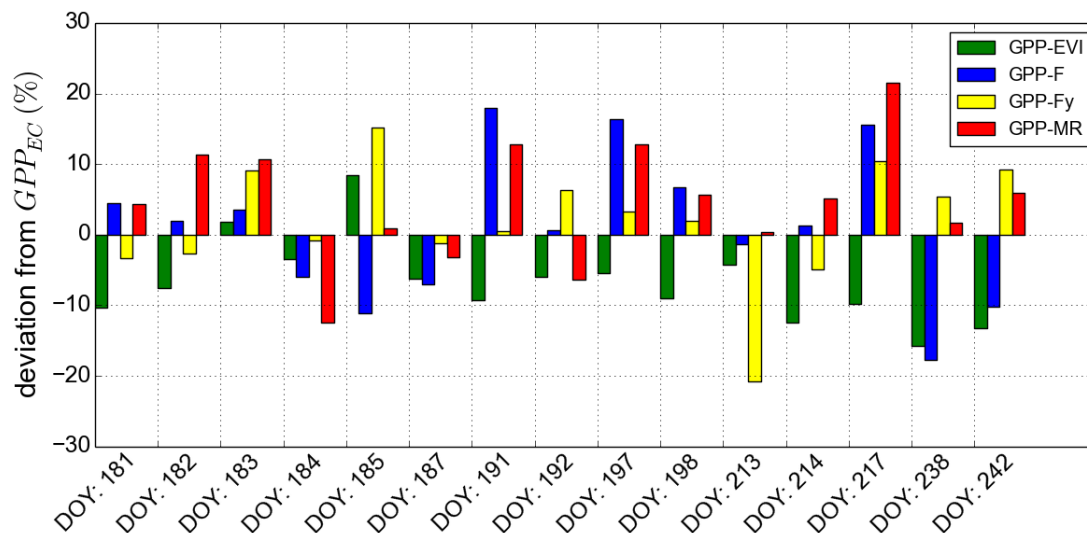


Figure 37: Deviation of modeled GPP (GPP_{EVI} : green bar, GPP_{F760} : blue bar, GPP_{ϕ} : yellow bar and GPP_{MR} : red bar) from eddy covariance derived GPP for sugar beet, where estimates based on 2015 measurements in Merzenhausen. The mean bias is -6.85 % for GPP_{EVI} , 0.99 % for GPP_{F760} , 1.84 % for GPP_{ϕ} and 4.73 % for GPP_{MR} .

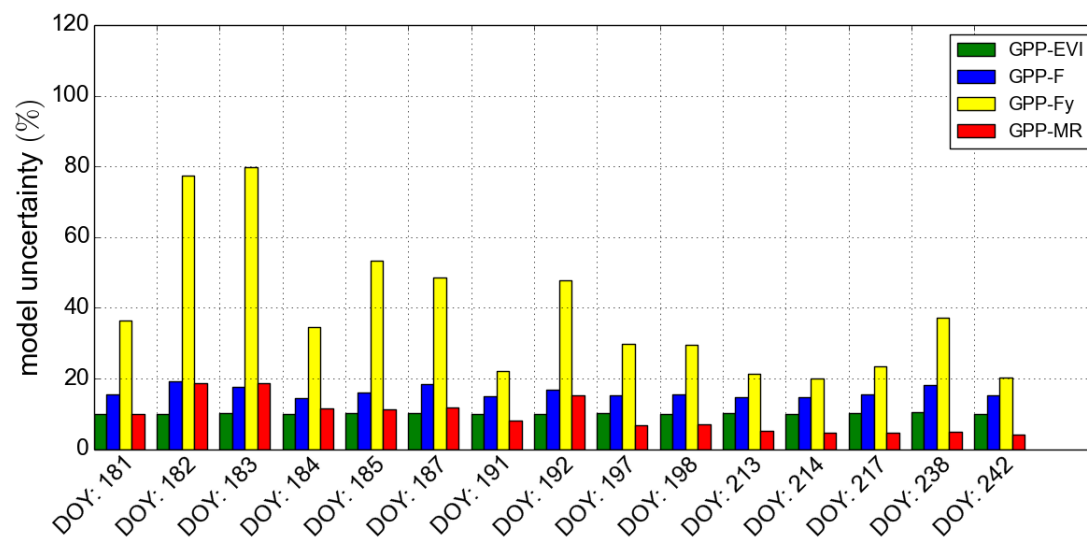


Figure 38: Model uncertainty in percent (GPP_{EVI} : green bar, GPP_{F760} : blue bar, GPP_{ϕ} : yellow bar and GPP_{MR} : red bar). The mean uncertainty is for GPP_{EVI} 10.11 %, for GPP_{F760} 16.16 %, for GPP_{ϕ} 38.77% and for GPP_{MR} 9.52 %. GPP estimates based on 2015 measurements within a sugar beet field located in Merzenhausen, Germany.

5.6. Estimation of spatiotemporal GPP

In this Section, estimates of the GPP_{EVI} , GPP_{F760} and GPP_{Φ} models are compared with infield measured GPP derived from ecosystem canopy chambers of the 2012 Selhausen campaign. Since the GPP_{MR} model needed additional in-situ measurements of PRI and $F_{687yield}$, which were not available for the 2012 campaign, this model was compared with maps of GPP upscaled from GPP_{EC} and $EVI_{HyPlant}$ measured in 2015 (c.f. Section 4.4). All models provide a statistically significant fit at the 95% confidence level. In Section 5.6.5 spatial patterns of the best fitting fluorescence based model and the best fitting reflectance based model of the 2012 *HyPlant* campaign are analyzed and compared with each other. Furthermore, GPP maps calculated with the multiple regression model are shown and compared with GPP maps upscaled from EC measurements and *HyPlant*-derived EVI.

5.6.1. Using reflectance based vegetation indices

Five different VIs (NDVI, EVI, PRI, MCARI2I and TCARI) were used to find the best representation for fAPAR used by the LUE model (c.f. Section 4.2.1). Best results were found for the enhanced vegetation Index (EVI). Figure 39-A shows EVI-based modeled and EC-derived GPP for the spatiotemporal Selhausen dataset. Results present high agreement between the GPP_{CC} and GPP_{EVI} values at medium levels of ca. 25-35 $\mu\text{mol CO}_2 \text{ m}^{-2}\text{s}^{-1}$. However, for the lower (upper) data range, GPP_{EVI} calculations tend to overestimate (underestimate) GPP_{CC} , resulting in a low slope of 0.49. Overall, the R^2 is high (0.8), mostly because of the concentrated data points for low GPP, however, for higher GPP there is a bigger spread. Due to over- and under estimations, the overall BIAS is -4.28 % relatively small, while the RMSE is, with 5.86 $\mu\text{mol CO}_2 / \text{m}^2\text{s}$ (19.35 %), relatively high. The uncertainty for GPP_{EVI} sums up to 12.26% while the uncertainty for GPP_{CC} is assumed to be 8% following Norman et al. (1997).

5.6.2. Using GPP-F₇₆₀ relationship model

Based on the linear regression model between $GPP_{CC,MSS}$ and $F_{760,MSS}$ (c.f. Section 4.2.2), GPP_{F760} was calculated (Figure 39 B). Results show a high agreement between the GPP_{CC} and GPP_{EVI} values at medium levels of ca. 25-35 $\mu\text{mol CO}_2 \text{ m}^{-2}\text{s}^{-1}$. However, in the lower data range GPP_{F760} is slightly overestimated, while in the upper data range it is strongly underestimated. This results in a slope of 0.54 and a strong negative BIAS of -16.23 %. Despite a strong R^2 of 0.8, the RMSE and the uncertainty are, with 6.71 $\mu\text{mol CO}_2 / \text{m}^2\text{s}$ (22.14 %) and 24.38% respectively, high.

5.6.3. Using LUE- F_{yield} relationship model

Figure 39-C shows modeled spatiotemporal GPP_{Φ} , based on the $F_{760\text{yield}}$ to LUE ratio approach proposed by Guanter et al. (2014), compared to GPP_{CC} derived from ecosystem canopy chamber measurements. While GPP_{Φ} in the lower data range is close to the identity line, values in the upper data range are underestimated. This results in a slope of 0.71 and in a negative BIAS of -11.43%. The R^2 is higher (0.84) and the RMSE lower ($5.23 \mu\text{mol CO}_2 / \text{m}^2\text{s}$, 17.26 %) than for the GPP_{EVI} and GPP_{F760} models. The uncertainty is high, but not as high as for GPP_{F760} (17.26% against 24.38%).

5.6.4. Using a multiple regression model

Based on the best fitting non-linear multiple regression model described in Section 4.2.4, GPP_{MR} was calculated and compared with upscaled GPP_{EC} (Figure 39 D). In contrast to the results shown previously, the GPP_{MR} model systematically overestimates GPP with values approaching the identity line at high value range ($20 - 24 \mu\text{mol CO}_2 / \text{m}^2\text{s}$). This results in a slope of the distribution fit of 0.75 and a positive BIAS of 7.36 %. The RMSE is very low, $1.48 \mu\text{mol CO}_2 / \text{m}^2\text{s}$ (6.62 %), while the R^2 is 0.83. The mean uncertainty values of GPP_{MR} and upscaled GPP_{EC} are 15.31 % and 11.15 % respectively.

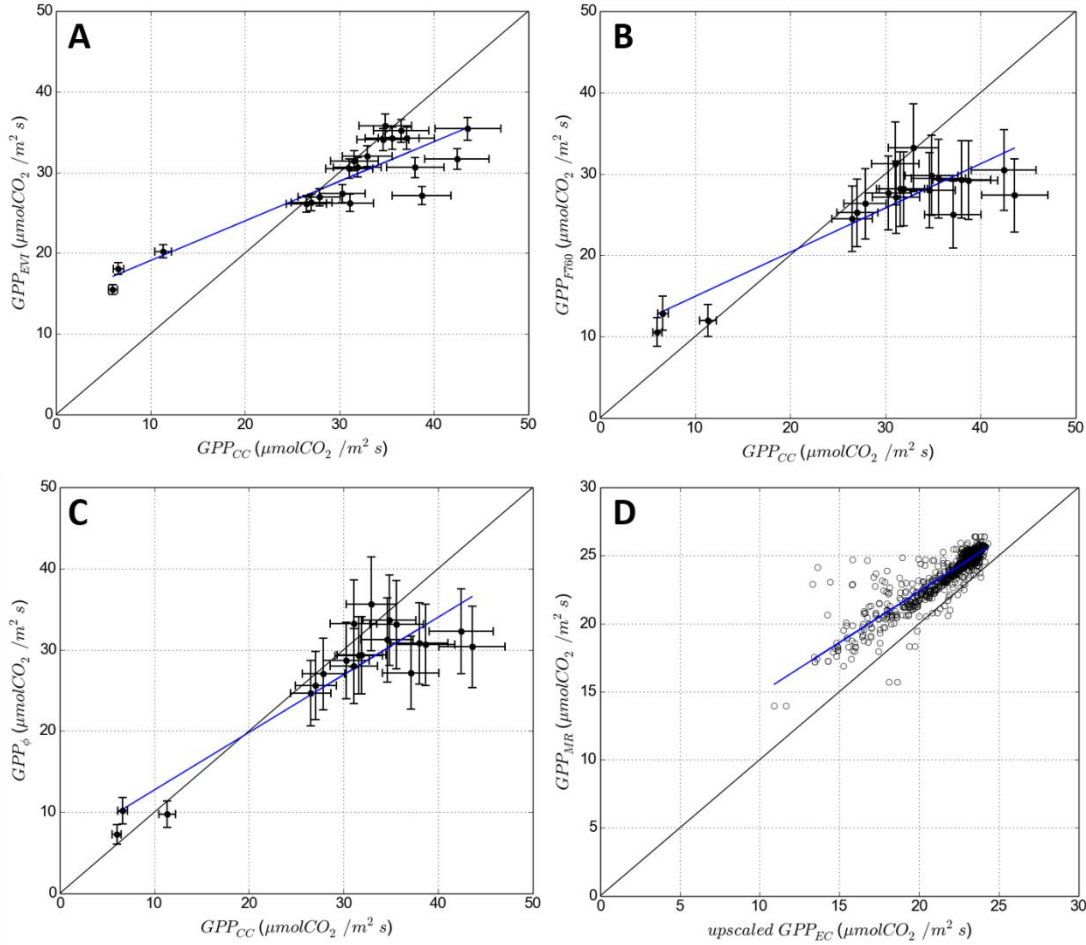


Figure 39: Scatter plot of spatio-temporal estimated (GPP_{EVI} , GPP_{F760} , GPP_{ϕ} , GPP_{MR}) and measured (GPP_{CC}) gross primary production (GPP) of a sugar beet field in 2012, Selhausen, Germany (A-C) and a sugar beet field in 2015, Merzenhausen, Germany. Modeled GPP_{EVI} based on Monteith LUE model driven by EVI as an estimator for $fAPAR$, GPP_{F760} based on a linear regression model between GPP_{CC} and $F_{760,MSS}$, GPP_{ϕ} based on LUE- F_{yield} model (Guanter et al., 2014) and GPP_{MR} based on a multiple regression model of LUE, $F_{760,yield}$, $F_{687,yield}$ and PRI. The coefficient of determination (R^2) for GPP_{EVI} , GPP_{F760} , GPP_{ϕ} and GPP_{MR} is 0.8, 0.8, 0.84 and 0.83 respectively. The BIAS for GPP_{EVI} , GPP_{F760} , GPP_{ϕ} and GPP_{MR} is -4.28%, -16.23%, -11.43% and 7.36% respectively. The relative RMSE for GPP_{EVI} , GPP_{F760} , GPP_{ϕ} and GPP_{MR} is 19.35%, 22.14%, 17.26% and 6.62% respectively. The slope for GPP_{EVI} , GPP_{F760} , GPP_{ϕ} and GPP_{MR} is 0.49, 0.54, 0.71 and 0.75 respectively.

5.6.5. Maps of reflectance- and fluorescence based GPP

Since GPP_{F760} and GPP_{ϕ} show very similar patterns, only the better performing fluorescence based GPP_{ϕ} is compared with the reflectance based GPP_{EVI} . GPP_{EVI} and GPP_{ϕ} maps (Figure 40) indicate that highest productivity levels are reached before solar noon and lowest values can be observed in the afternoon. For homogenous fields with high plant coverage like D, F and G (Figure 40) there are similar spatial patterns in the GPP_{EVI} and GPP_{ϕ} maps. Contrastingly, heterogeneous fields with areas of lower plant density (E, H and especially B) demonstrate the differences between GPP_{EVI} and

GPP_{ϕ} . While field B and H have lower values in the GPP_{ϕ} maps, higher values of GPP_{ϕ} in field E compared with the GPP_{EVI} values are observed. In general, GPP_{EVI} maps indicate a more homogenous productivity level within the fields and are more sharply contoured compared with GPP_{ϕ} (e.g., tractor tracks are clearly visible in fields D, E, and G).

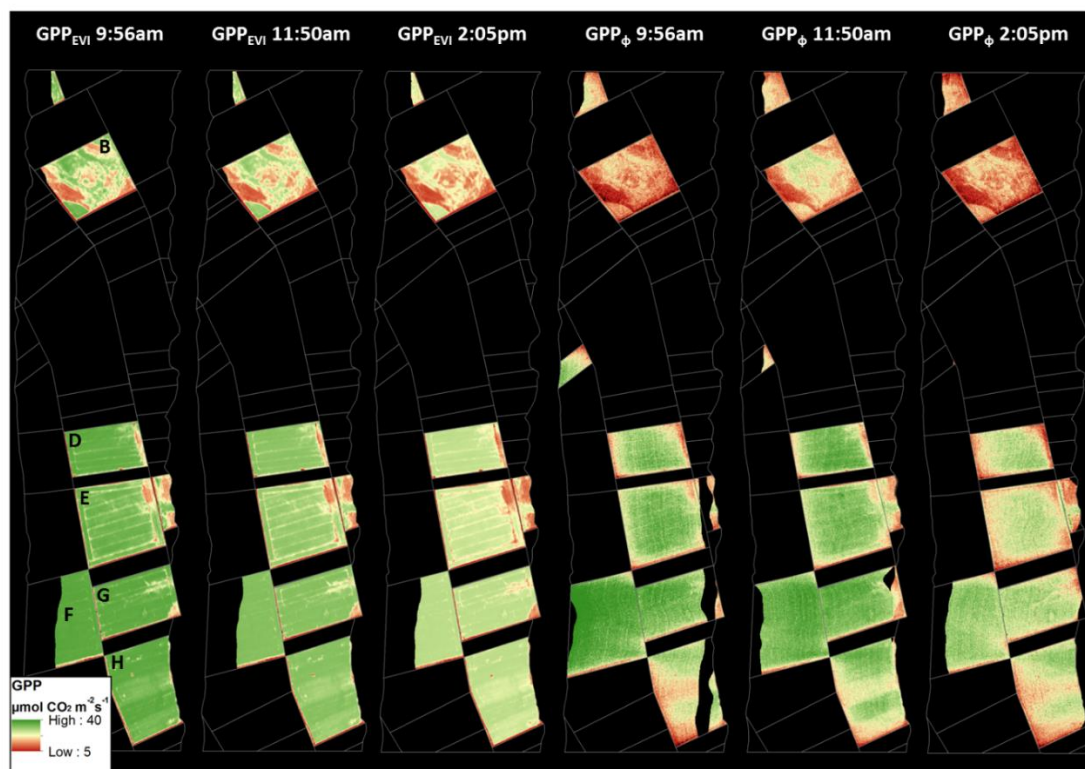


Figure 40: Maps of estimated GPP for sugar beet based on EVI and F_{760} at 9:56 a.m., 11:50 a.m. and 2:05 p.m. UTC in 2012 Selhausen, Germany.

$FAPAR_{EVI}$ and $F_{760yield}$ characterize the spatial patterns of the reflectance and fluorescence based models, respectively. Therefore, these two parameters were compared regarding their spatiotemporal changes during the measurement day. In general lowest $F_{760yield}$ values were detected for rapeseed field C and maize field A and highest values for sugar beet field D, E, F and G. $F_{760yield}$ increases from 9:56 a.m. to 11:50 a.m. within all agricultural fields (Figure 41). Especially for field B, a strong increase of $F_{760yield}$ was observed during morning hours and, interestingly, the formation of a distinctive diurnal course with maximum values during solar noon and a decrease towards the afternoon. In contrast, $F_{760yield}$ in the maize field (A in Figure 41) constantly increased throughout the day and maximum values were measured in the afternoon.

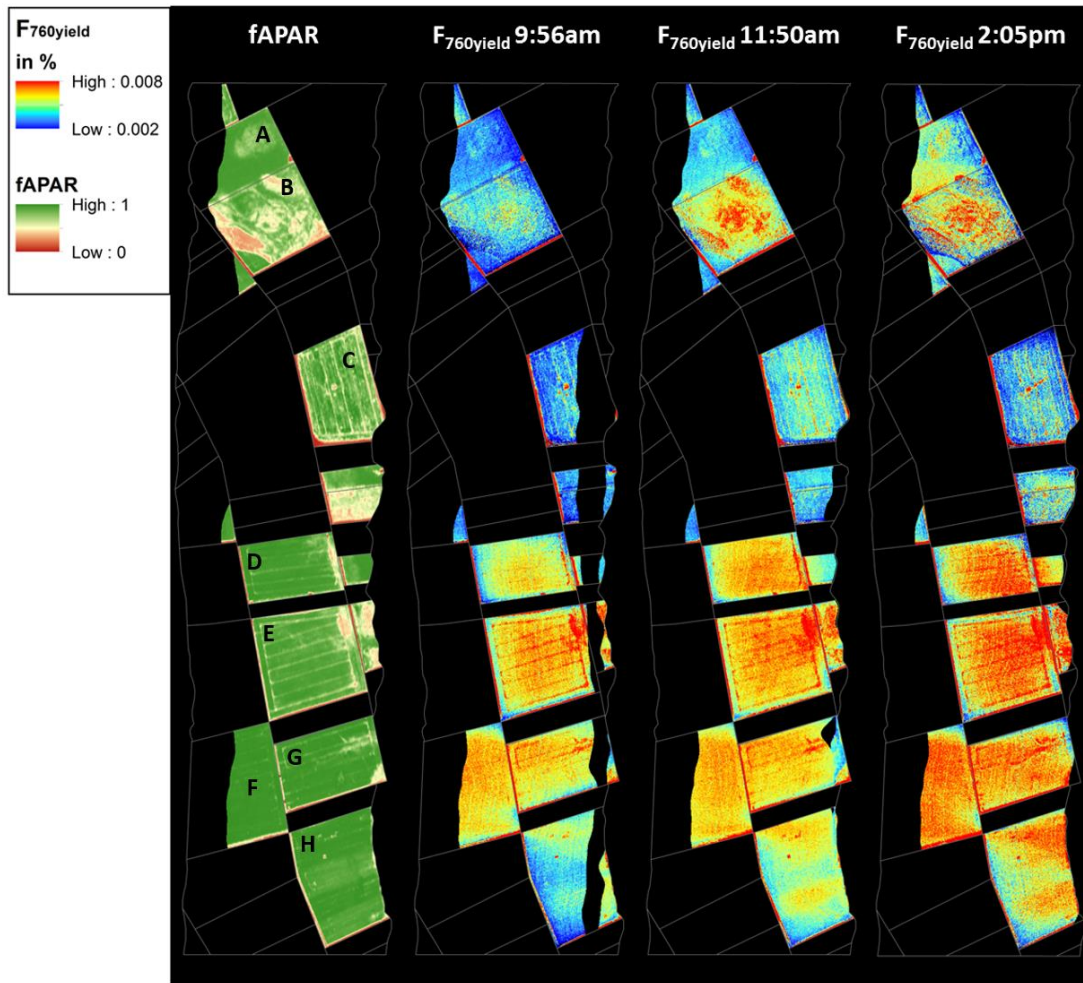


Figure 41: Spatial patterns of $fAPAR$ and $F_{760yield}$ for different local times. The maps are, from left to right, $fAPAR$ estimated by EVI; $F_{760yield}$ at 9:56 a.m.; 11:50 a.m.; 2:05 p.m. UTC in 2012 Selhausen, Germany.

The histogram in Figure 42 illustrate the changes in $fAPAR$ and $F_{760yield}$ that occur in the course of one day. While $fAPAR_{EVI}$ changes only slightly, the distribution of $F_{760yield}$ values, on the contrary, changes depending on overflight time and land use. For the more homogeneous sugar beet fields D to H, $F_{760yield}$ constantly increases over the day (Figure 42B), while $F_{760yield}$ of the heterogeneous sugar beet field B decreases in the 2:05 p.m. overflight (Figure 42D). Maize field A shows a constant increase of $F_{760yield}$ over the day with a proportionally stronger increase in the 2:05 p.m. overflight (Figure 42F). During the first two overflights, rapeseed field C showed an increase in $F_{760yield}$ and a decrease for the 2:05 p.m. overflight. Overall the sugar beet fields start and end with higher $F_{760yield}$ values than the maize and rapeseed fields in the morning and the afternoon.

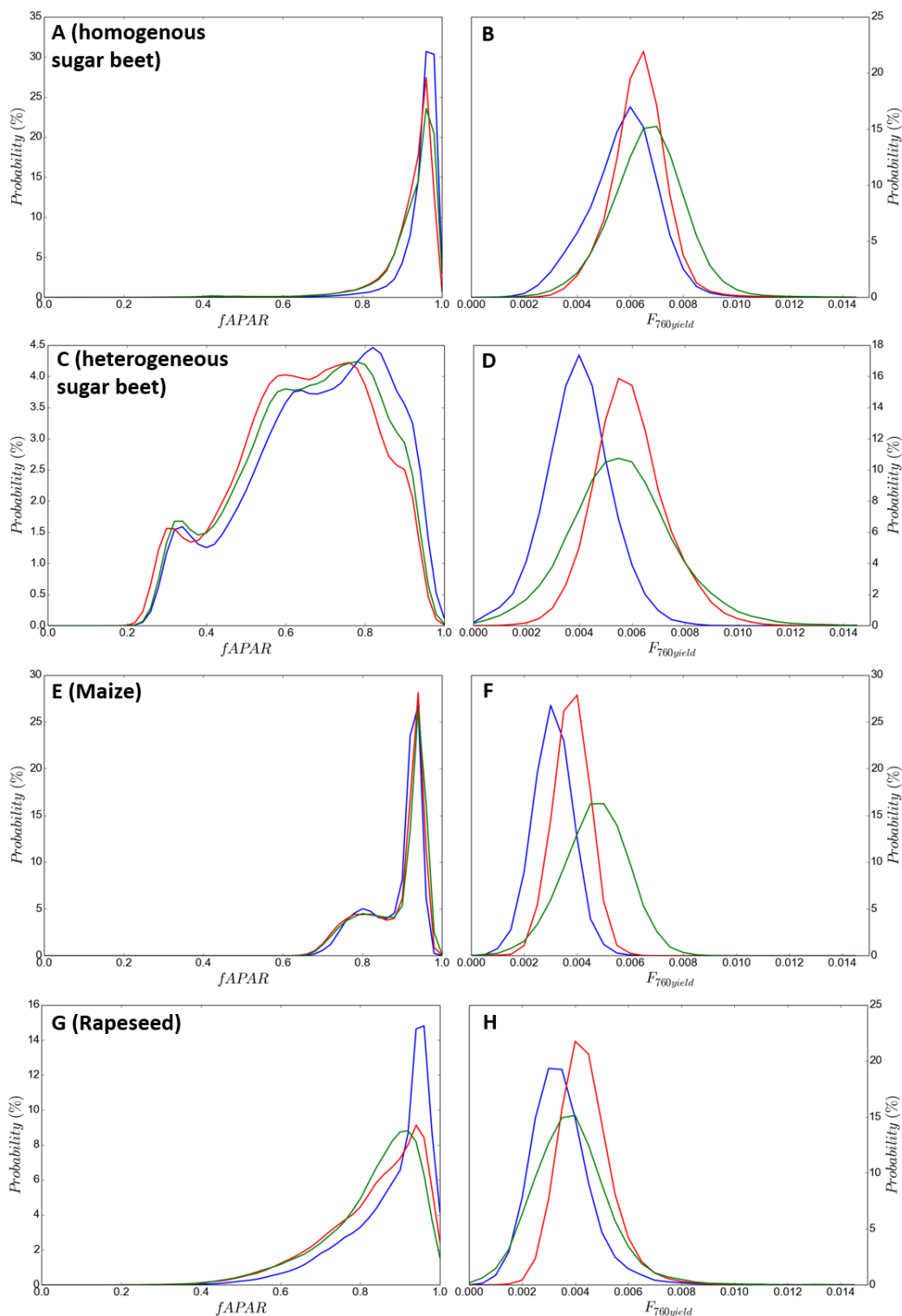


Figure 42: Probability density function of $fAPAR$ (left) and $F_{760yield}$ (right) for the overflights at 9:56 a.m. (blue), 11:50 a.m. (red) and 2:05 p.m. (green). Figures A and B show the probability distribution of sugar beet fields D-H. Figures C and D show the probability distribution of sugar beet fields B. Figures E and F show the probability distribution of maize field A. Figures G and H show the probability distribution of rapeseed field C.

Figure 43 shows the land use classification, the spectral vegetation indices EVI and PRI and the fluorescence yield at 760 and 680nm. The PRI and both fluorescence yields were used to drive the multiple regression model described in Section 4.2.4. Due to improvements in the signal to noise ratio and detector sensitivity, the 2015 *HyPlant* data appear much less noisy than the 2012 fluorescence maps. The PRI shows higher values for less dense canopies (lower EVI) which could be related to the sensitivity of PRI to canopy structure and to slow changes in leaf pigments during the growing season (Stylinski et al., 2002). The $F_{760\text{yield}}$ is highest in the northern winter barley field and for the southern sugar beet field. High values of F_{yield} within the tractor tracks can be explained by the different noise levels in F and EVI (F_{yield} is calculated from EVI derived fAPAR). While the $F_{760\text{yield}}$ clearly discriminates between different land uses, the $F_{680\text{yield}}$ is much more homogenous. Figure 44 shows GPP_{EC} upscaled from EC measurements by EVI (c.f. Section 4.2.4) and GPP_{MR} estimated by the multiple regression model. The maps show nearly identical patterns of GPP although GPP_{MR} shows slightly higher values, especially within the tractor tracks.

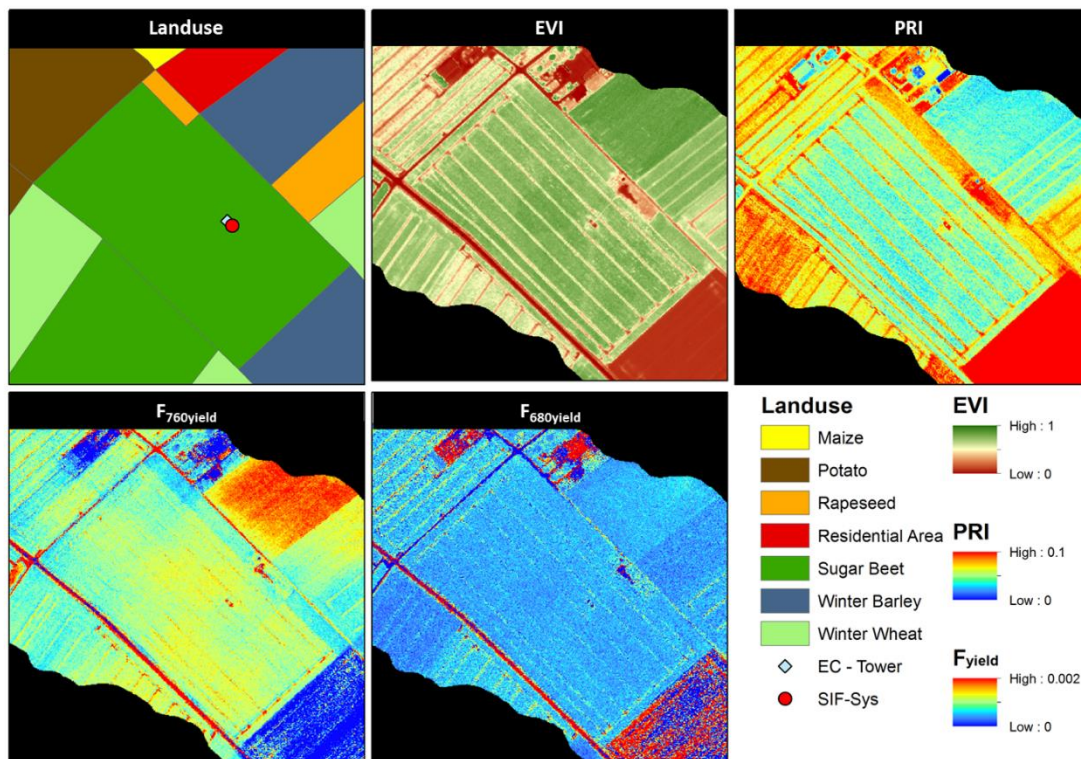


Figure 43: Maps of the land use, enhanced vegetation index (EVI), photochemical reflectance index (PRI) and fluorescence yield at 760 and 680 nm ($F_{760\text{yield}}$ and $F_{680\text{yield}}$) measured by *HyPlant* on the 30.06.2015 in Merzenhausen, Germany.

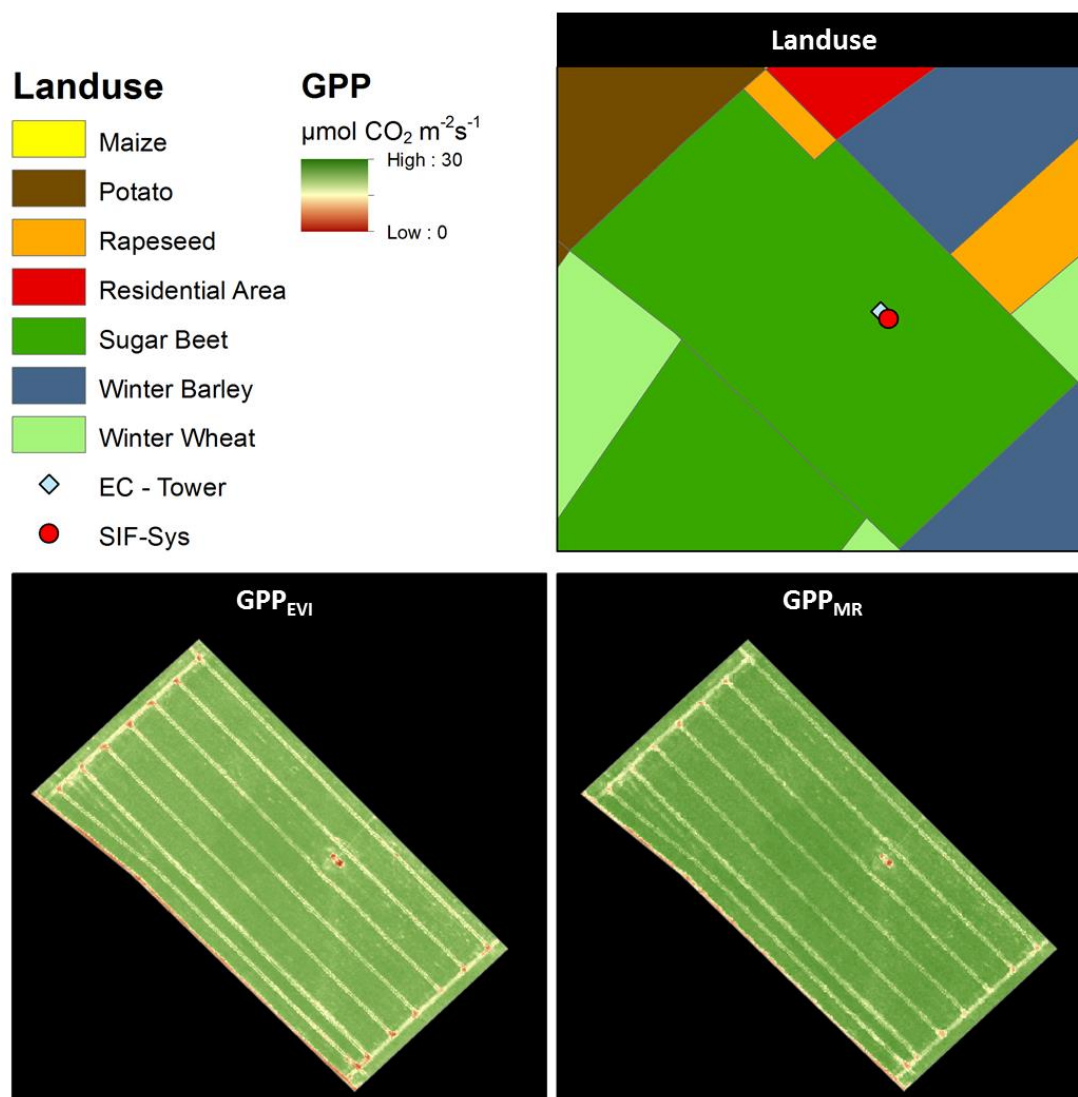


Figure 44: GPP maps upscaled from EC by EVI (GPP_{EC}) and estimated by the multiple regression model (GPP_{MR}) based on HyPlant $F_{760yield}$, $F_{687yield}$ and PRI observed on the 30.06.2015 in Merzenhausen, Germany.

5.6.6. Summary of spatiotemporal GPP estimation

Table 6 shows the performance overview of the GPP_{EVI} , GPP_{F760} and GPP_{Φ} models in estimating spatiotemporal GPP and the performance of the GPP_{MR} model in estimating spatial GPP. Since the GPP_{MR} is compared with a different dataset (Merzenhausen 2015), a direct comparison of the results from Selhausen 2012 is not feasible. The GPP_{EVI} , GPP_{F760} and GPP_{Φ} models all show a high coefficients of determination, which is mainly given by one chamber measurement located over sugar beet plants with low

leaf area index (LAI: 1.46), resulting in lowest measured and estimated GPP values. The GPP_{ϕ} model performs here as the best predictor with estimated GPP_{ϕ} closer to the identity line. All models underestimate high values of canopy chamber derived GPP_{CC} , whereby the GPP_{EVI} performs slightly better than the GPP_{ϕ} . The lowest BIAS is estimated by the GPP_{EVI} model, which is mainly related to the strong overestimation of GPP in the lower value range which balance the underestimation in the upper value range. Therefore, lowest RMSE is also provided by the GPP_{ϕ} model. Altogether, the GPP_{ϕ} model performed best for the spatiotemporal dataset.

The GPP_{MR} model performed very well in estimating spatial patterns in upscaled GPP_{EC} . Nevertheless, it has to be noted that GPP_{MR} and upscaled GPP_{EC} are not completely independent since both use EVI as model driver (GPP_{MR} uses EVI as a proxy for fAPAR, GPP_{EC} is scaled with EVI). However, since the measurement field in Merzenhausen is relatively homogenous (c.f. Figure 44), it is hypothesized that the regression improvement, due to a dependent variable, is relatively weak.

Table 6: Overview of spatiotemporal model performance. The GPP_{EVI} , GPP_{F760} and GPP_{ϕ} were validated with ecosystem canopy chamber derived GPP_{CC} at seven loctions. Field patterns of GPP_{MR} were compared with upscaled GPP derived from eddy-covariance and HyPlant EVI. Best results are marked in bold numbers. Because of the different forcing data GPP_{MR} is not directly comparable to the other models.

spatiotemporal models				
	GPP_{EVI}	GPP_{F760}	GPP_{ϕ}	GPP_{MR}
R^2	0.8	0.8	0.84	0.83
slope	0.49	0.54	0.71	0.75
RMSE ($\mu\text{mol CO}_2 / \text{m}^2\text{s}$)	5.86	6.71	5.23	1.48
relative RMSE (%)	19.35	22.14	17.26	6.62
BIAS (%)	-4.28	-16.23	-11.43	7.36

6. Discussion

6.1. In situ measurements

The in-situ measurements in 2012 show that LUE_{CC} follows a typical diurnal cycle, where values are highest early in the morning and decrease with excess light supply (c.f. Figure A49), high air temperatures, and decreasing soil water contents due to high evapotranspiration (Hilker et al., 2008). Since the maximum air temperature during the observation period did not exceed 23°C, we assume that temperature alone is not a limiting factor. Furthermore, the agricultural field was repeatedly fertilized, thus nitrogen/nutrient deficits are unlikely. Therefore, we assume that the LUE was decreased by 1) a downregulation of photosynthesis due to high levels of incoming radiation and 2) the associated stomatal closure to reduce transpiration. The diurnal course of $F_{760yield,MSS}$ is similar to that of LUE_{CC} , however, it is characterized by a different slope. During the decrease of LUE_{CC} and $F_{760yield,MSS}$, excess light energy is dissipated as heat (NPQ). The subsequent increase of LUE_{CC} and $F_{760yield,MSS}$ during the afternoon hours is most likely caused by a decrease of NPQ and a larger fraction of energy being used for photosynthesis. These results indicate that, in our study, changing radiation conditions are, most likely, the dominant effect on the downregulation of photosynthesis during noon time. The consistent use of F to estimate changes in photosynthetic activity critically relies on reliable estimates of NPQ. As mentioned, in homogenous canopies NPQ can be accessed by the photochemical reflectance index (PRI) (Grace et al., 2007; Meroni et al., 2008; Rahimzadeh-Bajgirani et al., 2012; Weng et al., 2006), but unfortunately the PRI was not available for the 2012 campaign.

The highly variable ratio of LUE_{CC} to $F_{760yield,MSS}$ over the day, especially during early morning, (cf., Figure 13D) contrasts with the assumption of a constant ratio under moderate light conditions in the morning (Yoshida et al., 2015). Figure 15 indicates a changing relationship between F_{yield} and LUE after solar noon. After solar noon, the LUE does not recover to the same level as before solar noon, which may be related to the still increasing temperature and progressive lower water availability. It has to be noted that the high R^2 partly results from the interpolation method used for estimating $F_{760yield}$ and LUE_{CC} . Nevertheless, non-interpolated results of the Merzenhausen campaign are in agreement with these findings, which suggests that diurnal LUE should not be easily linearly related to $F_{760yield}$.

The in-situ measurements in 2015 show a general decrease of diurnal LUE with increasing solar radiation and an analog increase of PRI. A decrease of LUE can be explained by protection mechanisms against strong solar radiation. Due to its sensitivity to the xanthophyll cycle, the PRI is an indicator for the protection

mechanism of NPQ. An increase in PRI represents an amplifying of the xanthophyll cycle and the connected release of energy by NPQ as heat. A decrease in LUE with a simultaneous increase in PRI can be found for all measurement days (c.f. Figure A49).

The relationship between LUE and the two fluorescence yields ($F_{760\text{yield}}$ and $F_{687\text{yield}}$) are more complex. Under moderate environmental and sole high temperature conditions (green circles and red squares in Figure 14) $F_{760\text{yield}}$ steadily decreases while $F_{687\text{yield}}$ is steady over the days. The relatively low and steady PRI indicates that the solar energy is mainly used for photosynthesis, which is in agreement with a high and increasing LUE. Interestingly, until solar noon (around 12 a.m.) the relationship between $F_{760\text{yield}}$ and LUE is weak and positive, and after solar noon is strongly negative. For unstressed days their absolute values are at their highest values.

On the days with increased environmental stress (black stars and blue triangle in Figure 14), the LUE and both fluorescence yields are generally low while PRI is strongest. With rising temperature and no available soil water, the stomata close to prevent desiccation. CO_2 diffusion into the plant will consequently be minimized, which results in a downregulation of the Calvin-cycle and the light reactions (c.f. Section 2.1.1-2.1.3) and a decrease of the LUE. The strong PRI indicates that excessive energy is mainly released as heat by the NPQ protection mechanism. Due to a strong increase in $F_{687\text{yield}}$ and relatively low $F_{760\text{yield}}$ (especially for the day affected by water scarcity and high VPD) the F_{ratio} is very high, which could indicate a strong activity of the protection mechanisms in PSII (c.f. Section 2.1.5). It has to be noted that due to severe stress, the plant canopy could also be affected by leaf wilting and leaf rolling (c.f. Section 2.1.4 and Figure 28). This would increase the $F_{687\text{yield}}$ due to decreased reabsorption effects. Nevertheless, recent work observed the same behavior of the F_{ratio} in response to drought stress for winter wheat, where the canopy structure is much less affected by water scarcity (Cendrero-Mateo et al., 2015). This suggests that two effects reveal plant stress in the fluorescence signal: the structural change in the canopy and changes in the process of photosynthesis.

The general increase in LUE after solar noon to an even higher level than in the morning (c.f. Figure A49) implies that the sugar beet plants are able to adapt to changing environmental conditions. In the first week of the measurement campaign an intense heat period was recorded. During this time, the LUE does not recover after solar noon. LUE shows only little response to increased temperature when there is abundance of soil water, this implies that high temperature alone may not be a good indicator for constraining LUE. The vapor pressure deficit (VPD) describes the difference between the amount of moisture in the air and the moisture holding capacity of the air at a given temperature. High VPD will result in increased transpiration which can be regulated by stomata conductance. Therefore, the vapor pressure deficit (VPD)

is used in the following as an indicator for limitations on the LUE due to stomata closure.

The diurnal relationships between LUE and $F_{760\text{yield}}$ show very variable behaviors within and between days (c.f. Figure A52 in appendix). While most days show a boomerang-shaped relationship between LUE and F_{yield} (in agreement with 2012 measurements), the diurnal course can be inverted. These results point out that the relationship between LUE and F_{yield} is not always linear and mostly changes around solar noon. Since the strongest environmental stress occurs around solar noon and the energy yields of fluorescence and photosynthesis are both low at this time, it can be assumed that the excessive energy is released as NPQ. The PRI as a proxy for NPQ shows a steady decline starting at 11th July 2015 (c.f. Figure A49). In part this is related to improved environmental conditions after the heat wave, which results in higher LUE. Since F_{yield} increases in both peaks, a reduced amount of energy is dissipated as NPQ. It has to be noted that a decrease in PRI could also be related to a decrease in the pigment pools during the end of the growing season (Stylinski et al., 2002) or to structural changes in the canopy (Wu et al., 2010). A correction method developed by Wu et al. (2010) was applied to the PRI, to correct for chlorophyll and structural effects. Unfortunately this correction method overcorrected the PRI, which resulted in a destruction of the diurnal patterns (not shown). Therefore, it has been decided not to apply this correction method.

6.2. Remote sensing of intra- and inter-daily plant adaptation strategies

Results of Section 5.2.2 show that the best inter- and intra-daily predictor of plant response to VPD variations is the F_{ratio} while the best predictor for the influence of PAW is the PRI and $F_{760\text{yield}+687\text{yield}}$. These results are in conformity with the meta-analysis by (Ač et al., 2015), who found the F_{ratio} to be the best predictor for heat stress while water stress is in general associated with a decrease of the red and far-red fluorescence (c.f. Section 2.7). With high VPD and low PAW, the stomata close to protect the plant for desiccation. With closed stomata, less CO_2 can enter the plant for the assimilation process, the dark reactions slows down, and excessive light energy is mainly released as NPQ which results in an increase of PRI. Under increased environmental stress conditions $F_{760\text{yield}}$ and $F_{687\text{yield}}$ decreases. When PAW is below zero, the variance in $F_{687\text{yield}}$ strongly increases. For days under severe water scarcity and high VPD, the $F_{687\text{yield}}$ shows higher values than for $F_{760\text{yield}}$, resulting in an overall high F_{ratio} . This could either indicate a changing contribution of PSII and PSI emitted fluorescence, a decrease of F_{687} reabsorption as consequence of canopy wilting and folding, or a combination of both mechanisms. However, both mechanisms defining

the F_{ratio} are direct reactions to water scarcity, which can be used to improve the prediction of plant productivity under drought conditions.

Results of Section 5.2.3 show that the PRI has the strongest relationship to intra- and inter-daily LUE, with a clear discrimination of PAW, while no discrimination of VPD is found. The F_{ratio} however, clearly discriminates high and low VPD values and shows a sensitivity towards PAW. An even more nuanced discrimination of water scarcity and VPD is visible in the PRI to F_{ratio} relationship, where clusters of similar VPD and PAW values are evident. Intra-daily $F_{760\text{yield}}$ and $F_{687\text{yield}}$ are difficult to relate with LUE because of their strong variance. Since the fluorescence data is already integrated from 6 seconds sampling time to 30 minutes, the strong variance is more likely a result of the complex processes within photosystems, than noise. It is important to note that $F_{760\text{yield}+687\text{yield}}$ shows a stronger relationship with LUE than the sole F_{yield} signals. Since $F_{760\text{yield}}$ and $F_{687\text{yield}}$ are differently affected by PSII and PSI, the combination of both signals seems to add information, explaining more variation in the LUE. An increase or decrease in intra-daily F_{yield} can have varying reasons and strongly depend on NPQ, since this is the main process for releasing excess energy within the photosystems (van der Tol et al., 2014). This also explains the strong non-linear relationship between intra- and inter-daily LUE and PRI. These findings are consistent with the strong intra- and inter daily relationships between PRI and LUE. The relationships between the different variables are generally stronger for the daily averaged data, especially for the relationship between $F_{760\text{yield}+687\text{yield}}$ and LUE and also $F_{760\text{yield}+687\text{yield}}$, and PRI.

Results of Section 5.2.4 show that strong relationship of PRI with LUE and its discrimination of PAW, in combination with the capability of the F_{ratio} to discriminate between high and low values of PAW and VPD, results in an overall good explanation of the intra-daily dynamics of the LUE. The results support the findings of Sections 5.2.2 and 5.2.3 that under high NPQ (high PRI values) and lowest LUE, the contribution of emitted F from PSI to total emitted F increases drastically (high F_{ratio}). Even though this strong increase of the F_{ratio} is partly connected to a decrease in reabsorption, other studies (Ač et al., 2015; Cendrero-Mateo et al., 2015) and results of the spatiotemporal patterns in this work (c.f. Section 5.2.6) present similar results for vegetation less affected by stress related changes in the canopy structure (e.g. maize or winter wheat). Outliers of relatively high LUE with high PRI, F_{ratio} , VPD and negative PAW, could be related to measurement errors of the eddy-covariance method. Due to a complex non-linear relationship, between LUE, PRI and F_{ratio} an appropriate model was not found.

Results of Section 5.2.5 demonstrate that a combination of PRI and F_{yield} improves the estimation of LUE. While the intra-daily dataset shows a complex non-linear relationship between the three variables PRI, F_{ratio} and LUE, the inter-daily relationship between PRI, $F_{760\text{yield}+687\text{yield}}$ and LUE allows defining a suitable regression model.

Since the additive signal of $F_{760\text{yield}}$ and $F_{687\text{yield}}$ shows a stronger correlation with LUE (c.f. Sections 5.2.3 and 5.2.5) it is strongly suggested to move further towards the retrieval of total fluorescence. Although the SFM retrieval (Meroni et al., 2009b) is capable of retrieving total fluorescence, a high spectral resolution (0.3 nm FWHM) is needed for a proper discrimination of the Fraunhofer lines. Since the current setup of the *SIF-Sys* does not fulfill these specifications (c.f. Section 3.3.1.) the retrieval of F_{tot} was not possible. Results of the intra- and inter-daily dataset provide strong evidence that fluorescence strongly contributes in the interpretation of short term stress reactions and their impact on LUE.

6.3. Remote sensing of spatiotemporal plant adaptation strategies

Results show that amongst the vegetation indices, the EVI, performs best as a proxy for spatial variability of fAPAR in the LUE model. Since the EVI was designed to be less sensitive to saturation effects and to soil reflectance (Huete et al., 2002), it estimated the upper and lower levels of plant productivity better than the other vegetation indices tested. However, the estimates of GPP_{EVI} show both saturation effects at high canopy density and the effects of soil reflectance for sparse canopies. Since the EVI is particularly sensitive to canopy structure, fAPAR values did not change significantly across the investigated fields over the day. Minor changes detected are most likely related to surface anisotropy effects in combination with the illumination geometry rather than to plant adaptation to changing environmental conditions.

The comparison of *HyPlant*'s first fluorescence maps in both peaks (F_{760} and F_{680}) indicates that differences in canopy structure and species have an impact on F_{ratio} (cf. Figure 26 & Figure 27). During unstressed conditions, variations in F_{ratio} are most likely related to structural variables such as canopy chlorophyll content: F_{760} generally increases with increasing chlorophyll concentration, while F_{687} decreases due to re-absorption of the emitted F signal in this wavelength (Buschmann, 2007). Under environmental stress (i.e., drought, heat), values of F_{ratio} can change due to changes in the leaf and canopy structure (e.g., leaf angle adjustments and movement (Arena et al., 2008; Kadioglu et al., 2012)), again affecting the re-absorption of red fluorescence. Moreover, these variations may be related to physiological changes that, in turn, affect F_{ratio} , which reflects a changing contribution of fluorescence emission from Photosystem I (PSI) and Photosystem II (PSII) in response to plant stress (Porcar-Castell et al., 2014). The meta-analysis by (Ač et al., 2015) showed that water-, temperature- and nitrogen-stress differ in their effect on F_{ratio} . Since rapeseed is still in the growing phase, the high values of F_{ratio} are most likely linked to lower reabsorption due to low chlorophyll content and low leaf area. High values of F_{ratio} in sugar beet fields with low EVI, however, cannot be solely linked to lower re-absorption effects.

From electrical conductivity measurements and soil profiles it is known that various fields in this area show high gravel content, originating from sediments of a fossil river bed of the Rur river (Rudolph et al., 2015; Weihermüller et al., 2007). The high gravel content strongly affects the water holding capacity as well as the soil organic carbon. This results in a significant lower plant density in sugar beet field B and the eastern border of field D, E and G. With increasing temperature and low water availability, sugar beet plants located on the fossil river bed are strongly affected by water stress, compared to other plants. The derived F_{ratio} map captures this effect and reveals higher F_{ratio} values for water stressed plants, in agreement with results discussed in (Ač et al., 2015). The ability to track the variation of this ratio from unstressed to stressed conditions over time and space can therefore help in distinguishing between different sources of stress.

Maps of $F_{760\text{yield}}$ are characterized by a strong diurnal variability, which can be related to dynamic plant adaptation strategies to variable environmental conditions. In Section 5.1 it was shown that under non- and low-stress conditions in the morning, the LUE presents an exponential decrease relative to $F_{760\text{yield}}$ (c.f. Figure 15). After noon, this relationship becomes linear and $F_{760\text{yield}}$ increases much more strongly than LUE. A similar behavior can be observed in the $F_{760\text{yield}}$ maps derived from *HyPlant*, where most fields present little changes in $F_{760\text{yield}}$ before noon and a stronger increase after noon. Interestingly, in sugar beet fields with high F_{ratio} , the $F_{760\text{yield}}$ is mostly constant over the day. It is therefore assumed that the positive relationship of LUE to F_{yield} could be inverted during strong environmental stress conditions, when NPQ reaches high levels (Figure 41).

The different behavior in $F_{760\text{yield}}$ of sugar beet (low increase until noon and the subsequent stronger increase) compared to maize (steady but low increase over the day) might be explained by a better adaptation of C4 plants to dry and high light conditions, while the low $F_{760\text{yield}}$ in rapeseed could be associated to their early growing stage.

6.4. Estimation of intra- and inter-daily GPP

Results of Section 5.4 show that all four models have problems in estimating intra-daily GPP, while the estimation of inter-daily GPP shows significantly better results. Since all models depend on different parameters and parameter combinations, their performance mainly depends on the ability of the indices to capture the vegetation state. Here, the results of intra- and inter-daily estimations are discussed and validated.

As the GPP_{EVI} model uses daily averaged LUE derived from measurements, the diurnal plant adaptation depends on EVI only. Greenness-based vegetation indices (like the EVI) are generally known for their overestimation of sparse and underestimation of dense vegetation cover. Since the canopy density of the observed sugar beet was

relatively homogenous and dense (due to the end of growing season), the systematic underestimation of intra- and inter-daily GPP_{EVI} was relatively small (-6.83 % and -7.93% respectively, c.f. Figure 32). Despite the moderate R^2 of intra-daily estimates (0.48), the strong variance and the systematic underestimation highlight the problematic representation of intra-daily plant adaptation by the EVI. The inter-daily results show less variance and significantly higher R^2 (0.83), but also a stronger negative bias, indicating a systematic underestimation of seasonal GPP by the EVI due to spectral saturation effects. The overall model uncertainty is relatively small (about 10%), which is mainly due to the low standard error in the EVI measurements. It has to be noted that the GPP_{EVI} model, as it is used in this thesis, strongly depends on daily measured LUE and therefore is limited in its application. Actually, the concept of this model can be applied for global estimations of GPP, but these models are based on calculated LUE, which has been shown to be highly uncertain (Huete et al., 2002; Turner et al., 2003; Running et al., 2004; Xiao et al., 2008). In this work the GPP_{EVI} serves more as a reference for the performance of reflectance based VIs, used for comparison.

Results of the GPP_{F760} model show low R^2 and high RMSE for intra- and inter-daily GPP estimations. Since both parameters (GPP and F_{760}) depend on APAR, a much stronger coefficient of determination should be expected. A separate consideration of samples under stressed and non-stressed conditions showed no improvement in the estimation. Since F_{760} represents only a small fraction of the dissipated energy, it can be assumed that F_{760} alone is an insufficient proxy for GPP. The uncertainty of the model for intra- and inter-daily estimates (16.76% and 18.12% respectively) is mainly defined by the uncertainty of F_{760} measurements.

The performance of the GPP_{Φ} model strongly differs between intra- and inter-daily estimates. While intra-daily estimates present strong variance, resulting in the lowest R^2 (0.29) and the highest RMSE (7.63 $\mu\text{mol CO}_2/\text{m}^2\text{s}$, 30.15%), the inter-daily results show high R^2 (0.78) and the lowest RMSE (2.23 $\mu\text{mol CO}_2/\text{m}^2\text{s}$, 8.85%). Both models depend on the daily averaged LUE/ $F_{760\text{yield}}$ ratio. Results of Section 5.1 showed that, depending on NPQ, the diurnal relationship between LUE and $F_{760\text{yield}}$ varies strongly within and between days. The negligence of NPQ results in a misinterpretation of intra-daily GPP. Inter-daily estimations however, seem to be less sensitive to diurnal changes in the LUE/ $F_{760\text{yield}}$ ratio and NPQ, resulting in significant better results. The error propagation of the uncertainty in F_{760} , $F_{760\text{yield}}$ and LUE results in an overall high uncertainty of almost 47%.

The GPP_{MR} model shows the best results for intra-daily GPP estimation. The use of PRI as an indicator for NPQ significantly improves the intra-daily estimates. Interestingly, GPP_{MR} distinguish between high and low values of VPD: while GPP is overestimated for low values of VPD, it is underestimated for high values of VPD. This

can be related to the findings of Section 5.2.2 and 5.2.3 which demonstrate the discriminability of PAW and VPD by a combination of PRI and F. These findings support the argument that a combination of PRI and fluorescence allows for an improved representation of intra-daily plant adaptation. The inter-daily estimation shows similar results than the GPP_{Φ} model, indicating that the PRI, as an estimator for NPQ, does not significantly improve the estimation of inter-daily GPP. Due to the sensitivity of the multiple regression model to PRI, the overall uncertainty (8.62% intra-daily and 9.56% inter-daily) mainly depends on its standard error. It has to be noted that the uncertainty of the independent variable (LUE) was neglected in the multiple regression model. Therefore, the overall uncertainty of the GPP_{MR} model is underestimated.

6.5. Spatiotemporal estimation of GPP

The comparison of GPP_{EVI} , GPP_{F760} and GPP_{Φ} with GPP_{CC} (c.f. Section 5.6) indicate a better performance of the F-based estimations of GPP at low CO_2 assimilation rates. A potential explanation is that F_{760} is not affected by signal contributions from the canopy background (e.g., soil, non-photosynthetic material). This finding is in agreement with the results of Section 6.4, where a similar behavior of GPP_{EVI} was found. Additional information of the LUE to $F_{760yield}$ ratio allows a better representation of low and high plant productivity for the GPP_{Φ} model, in contrast to the GPP_{F760} model. The uncertainty levels of GPP_{F760} and GPP_{Φ} estimates highlight the need for improved instrumentation, particularly in terms of signal stability (SNR). Nevertheless, similar spatial patterns found for GPP_{Φ} and GPP_{EVI} maps provide evidence that airborne-based F_{760} measurements are sensitive to spatial variations of photosynthetic activity. The low GPP estimates from both models in field B, the eastern border of field D, E and the lower eastern corner of field G (Figure 40), can be related to a high gravel content of the soils, originating from sediments of a fossil river bed of the Rur river (Rudolph et al., 2015; Weihermüller et al., 2007). The lower water holding capacity of such soils limits plant growth, which is clearly reflected in the observations.

The comparison between GPP_{MR} and GPP_{EC} indicate a systematic overestimation of the multiple regression model, especially in the lower value range. Since the upscaling of GPP_{EC} is based on EVI, the overestimation of GPP_{MR} in the higher value range could be related to an underestimation of GPP_{EC} due to saturation effects in EVI. The stronger overestimation of GPP_{MR} in the lower value range may be related to the overestimation in the F_{yield} within the tractor tracks.

6.6. Model applicability for satellite based remote sensing data

The biggest advantage of the GPP_{F760} model is its easy applicability for satellite-based remote sensing data. Besides ground measurements of GPP, only satellite-derived F_{760} is needed to estimate global GPP. The first successful application of this model with GOSAT retrieved fluorescence was shown by Frankenberg et al. (2011). The spatial and temporal high resolution data of this thesis however, showed that F_{760} alone is a poor indicator for the dynamics in photosynthesis. This leads to the assumption that the strong relationship of GPP with fluorescence retrieved by GOSAT, that has coarse spatiotemporal resolution (0.5° and monthly time-step), is mainly due to their common dependent variable APAR.

The diurnal and seasonal change in the LUE to $F_{760yield}$ relationship makes the satellite application of the GPP_ϕ model problematic. Operational ground measurement combining systems of EC and spectrometer within different ecosystems would be necessary to calculate the daily mean LUE to F_{yield} ratio. Since only a few fluorescence measurement systems are in use at the moment, the applicability of the GPP_ϕ model at global scale is currently unfeasible.

Even though the GPP_{MR} model showed the most promising results, its application to satellite data poses several challenges. A satellite based estimation of GPP_{MR} would require measurements of PRI and F_{yield} . As discussed in Sections 3.3 and 5.6.4 the PRI is affected by canopy structure and leaf pigment pools (like chlorophyll), which aggravates the interpretation of the PRI as an indicator for NPQ. Therefore, new algorithms have to be developed to remove the seasonal changes in PRI (Wu et al., 2010). The F_{yield} is calculated from F and APAR. Global estimates of APAR are based on modeled PAR and reflectance-based fAPAR. Since fAPAR is also attributed with a certain uncertainty (Fensholt et al., 2004) the overall uncertainty of F_{yield} increases. Furthermore, in-situ measurements of fluorescence, reflectance and CO_2 fluxes in different ecosystems are needed to parameterize the multiple regression model.

6.7. Measurement uncertainty of the SIF-Sys

The strong random error in both F signals and the strong systematic error in the F_{687} signal at the beginning of the measurement campaign are very likely related to high temperature within the electronic section of the measurement system. While the section with the spectrometer was consistently cooled down to $25\text{ }^\circ\text{C}$, the electronic section heated up to temperatures exceeding $50\text{ }^\circ\text{C}$. Figure A53 shows that there is a positive relationship between the overestimation of the F_{687} signal and the temperature in the electronic section of the measurement system ($R = 0.54$). A high temperature gradient between the cooled and uncooled part of the FLOX system could have an effect on the

optical fibers. This could affect the measured spectra which, in turn, affects the curve fitting of the iFLD method, resulting in an overestimation of fluorescence. The F_{687} is more strongly affected by this error because the iFLD curve fitting of the O_2B bands is much more sensitive than the curve fitting of the O_2A band. Even if the quantification of this error allows for a correction, it is strongly suggested to analyze these effects in more detail and to avoid, in future campaigns, high temperatures in any part of the measurement system.

6.8. Reliability of retrieved F_{760} and F_{687} maps

HyPlant's FLUO module allows, for the first time, simultaneous retrievals of F_{760} and F_{687} in validated physical units with high spatial resolution (cf., Section 5.5.1 and Rascher et al. (2015)). Maps of F_{760} and F_{687} for 2012 and 2015 appear noisy when compared with the maps of calculated VIs (Figure 26 & Figure 43). These effects are caused by a combination of the lower signal-to-noise ratio (F emissions are a small radiation flux of the signal eventually measured at a remote sensor) and the detector sensitivity (the high spectral and spatial resolution reduces the energy actually measured at the detector array). However, apparent noise effects do not limit the interpretation of the F retrievals and can be further compensated by applying a spatial-spectral binning. In the 2012 *HyPlant* maps, gradients in F_{760} and derived data products (i.e., GPP_{760}) from the border to the center of the fields were observed. These gradients are partly caused by a sensor effect (i.e., a point spread function non-uniformity) which was solved by a hardware change in 2014 and thus do not appear in the 2015 *HyPlant* map. This effect, however, does not impact the results of the spatiotemporal GPP estimation since measurements from homogeneous field centers were deliberately analyzed. With the 2012 *HyPlant* campaign some of the first maps of F_{687} , providing interesting insights into the information content of F. The higher variability of F_{687} relative to F_{760} was also documented by Rossini et al. (2015) over a grassland site and is most likely caused by the higher retrieval noise associated with the narrow O_2B absorption band.

7. Towards a mechanistic model linking fluorescence with photosynthesis

Findings of the preceding chapters showed that seasonal changes in LUE can be accessed by the PRI and fluorescence. However, the PRI is only a proxy for NPQ, and fluorescence is still not available in its full spectrum. Furthermore, fluorescence and PRI only represent the light reactions, while the LUE is also defined by the dark reactions and the stomata conductance. Therefore, dynamic changes in diurnal LUE cannot be fully captured by PRI and fluorescence.

In this chapter, a new mechanistic scheme is proposed to account for the mentioned shortcomings of empirical models. Instead of relating PRI and fluorescence to LUE, results of this work were used to determine the electron transport rate (ETR), which then can be used to determine the maximum rate of electron transport (J_{max}). J_{max} is, besides V_{cmax} (maximum rate of carboxylation), an important parameter in the Farquhar et al. (1980) photosynthesis model used by the majority of land surface models. J_{max} can be derived from leaf level PAM fluorometer measurements (c.f. Section 2.3) and is normally sampled on several leaves and plants to derive an average J_{max} . Seasonal measurement of J_{max} , which also account for spatial heterogeneity, are time and cost intensive. The possibility to derive ETR and consequentially J_{max} from remotely sensed data would, therefore, not only reduce work and costs, but also allow for a better representation of plant adaptation in land surface models.

The model proposed here is based on the assumption that absorbed light is distributed between the pathways of photochemical-quenching (PQ), non-photochemical quenching (NPQ) and fluorescence (F):

$$APAR = PQ + NPQ + F \quad (49)$$

While APAR can be calculated from modeled or measured PAR and reflectance based fAPAR, NPQ and total F can only be estimated by the proxy PRI and F_{760} , respectively. To calculate NPQ from the PRI, the normalized PRI values (ranging from 0-1) are set to correspond to the range between minimum and maximum NPQ:

$$NPQ \approx \left(\frac{(PRI - PRI_{min})}{(PRI_{max} - PRI_{min})} \cdot (NPQ_{max} - NPQ_{min}) + NPQ_{min} \right) \cdot APAR \quad (50)$$

while F_{tot} was calculated as:

$$F_{tot} \approx \left(\frac{(F_{760} - F_{760,min})}{(F_{760,max} - F_{760,min})} \cdot (F_{tot,max} - F_{tot,min}) + F_{tot,min} \right) \cdot APAR \quad (51)$$

Maximum and minimum values of PRI and F_{760} can be derived from seasonal spectral measurements, while maximum and minimum values of NPQ and F_{tot} are plant dependent parameters which can only be derived from leaf level measurements. Since no leaf level measurements were available for this study, NPQ_{max} , NPQ_{min} , $F_{tot,max}$ and $F_{tot,min}$ were set to 98%, 17.5%, 2% and 0.5% respectively (Buschmann C. oral presentation). The ETR can then be calculated as:

$$ETR = (APAR - NPQ - F_{tot}) \cdot 0.5 \quad (52)$$

Where the factor 0.5 assumes an equal excitation of both photosystems. By driving Eq. 52 with a diurnal dataset of PRI and F_{760} , the maximum ETR (equivalent to J_{max}) can be determined.

Figure 45 shows the artificial diurnal cycle of GPP and the input data for the ETR model: APAR, F_{760} and PRI. GPP increases with APAR until 10 a.m., stabilizes with highest APAR and subsequently decreases after 2 p.m. F_{760} follows the diurnal cycle of APAR and PRI the diurnal cycle of GPP. The artificial dataset represents a day during growing season under sole light stress conditions over noon.

Figure 46 shows the measured diurnal cycle of GPP, APAR, F_{760} and PRI on August 30 2015 within a sugar beet field. The maximum temperature was 30°C, the maximum VPD 20hPA and the minimum PAW 15 mm. GPP follows a typical diurnal cycle with highest values around solar noon. Since the canopy of the sugar beet is fully developed, the overall CO_2 assimilation rate is relatively high ($40 \mu\text{mol } CO_2 \text{ m}^{-2}\text{s}^{-1}$). The F_{760} and PRI follow a similar diurnal cycle as APAR. The PRI is very low, with maximum at -0.33, indicating a low activity of the xanthophyll cycle.

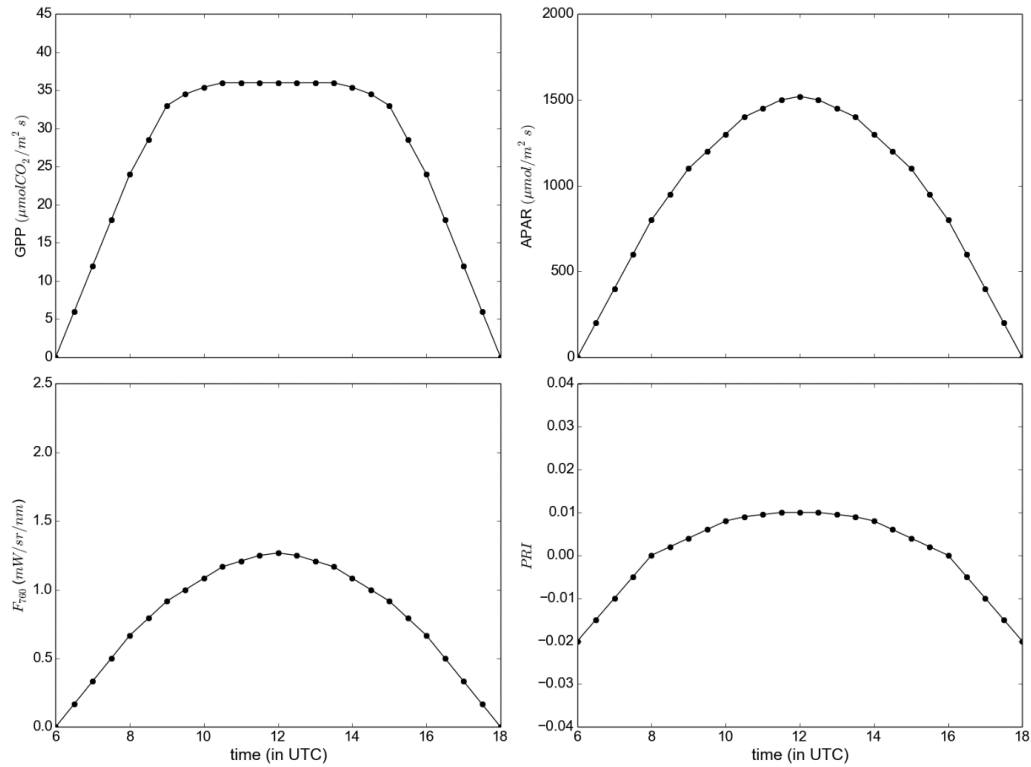


Figure 45: Idealized diurnal cycle of GPP, APAR, F_{760} and PRI based on artificial data.

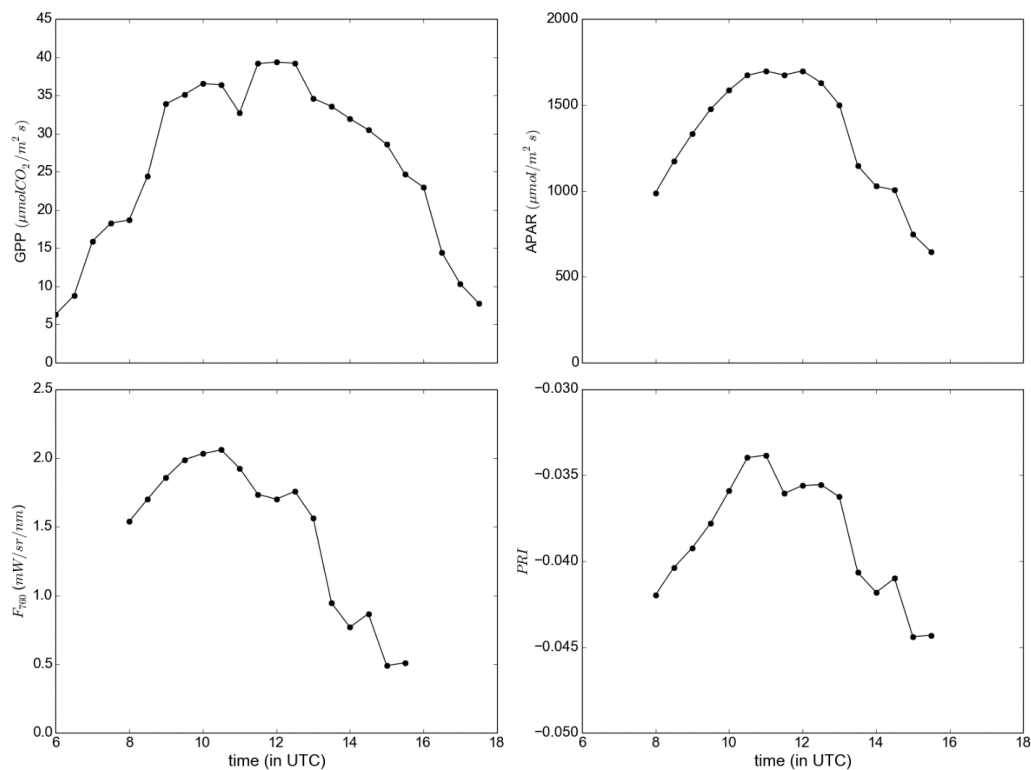


Figure 46: Measured diurnal cycle of GPP, APAR, F_{760} and PRI within a sugar beet field on the 30.08.2015 in Merzenhausen, Germany. The temperature was max. 30 C°, VPD 20 hPA and PAW between 15 and 20 mm.

Artificial and measured PRI, F_{760} and APAR were used to drive the ETR model (Eq. 52). Results are plotted against APAR to allow a better comparison with the literature (Figure 47 & Figure 48).

The idealized and measured data show that, with increasing APAR, the CO_2 assimilation saturates and consequently the LUE decreases. As a protection mechanism, NPQ and F_{tot} increase exponentially with APAR. Literature shows that the reaction of NPQ and F_{tot} to increasing APAR varies strongly over day, season and species, which makes this comparison difficult. However, in general, a linear or exponential increase can be found (Bilger et al., 1995; Cendrero-Mateo et al., 2015; Porcar-Castell, 2011; Schickling, 2012). PQ and ETR show an asymptotic increase but no saturation effect like GPP, which is also in disagreement with the literature. It has to be noted that ETR is normally estimated by exposing a leaf with an increasing light pulse. Since the ETR model is forced with diurnal measurements, and the photosystems adapt to changing environmental conditions, the light response curves of the measured data show less strong saturation effects and more variability. Resulting absolute values of estimated ETR are in agreement with ETR measurements performed in sugar beet with similar CO_2 assimilation rate (max. $40 \mu\text{mol CO}_2 \text{ m}^{-2}\text{s}^{-1}$ with an ETR of max. $400 \mu\text{mol m}^{-2} \text{ s}^{-1}$) (Schickling, 2012). However, in order to validate the proposed model scheme, a combined dataset of diurnal sun induced fluorescence and leaf-level PAM fluorometer measurements, encompassing a full growing season, would be required.

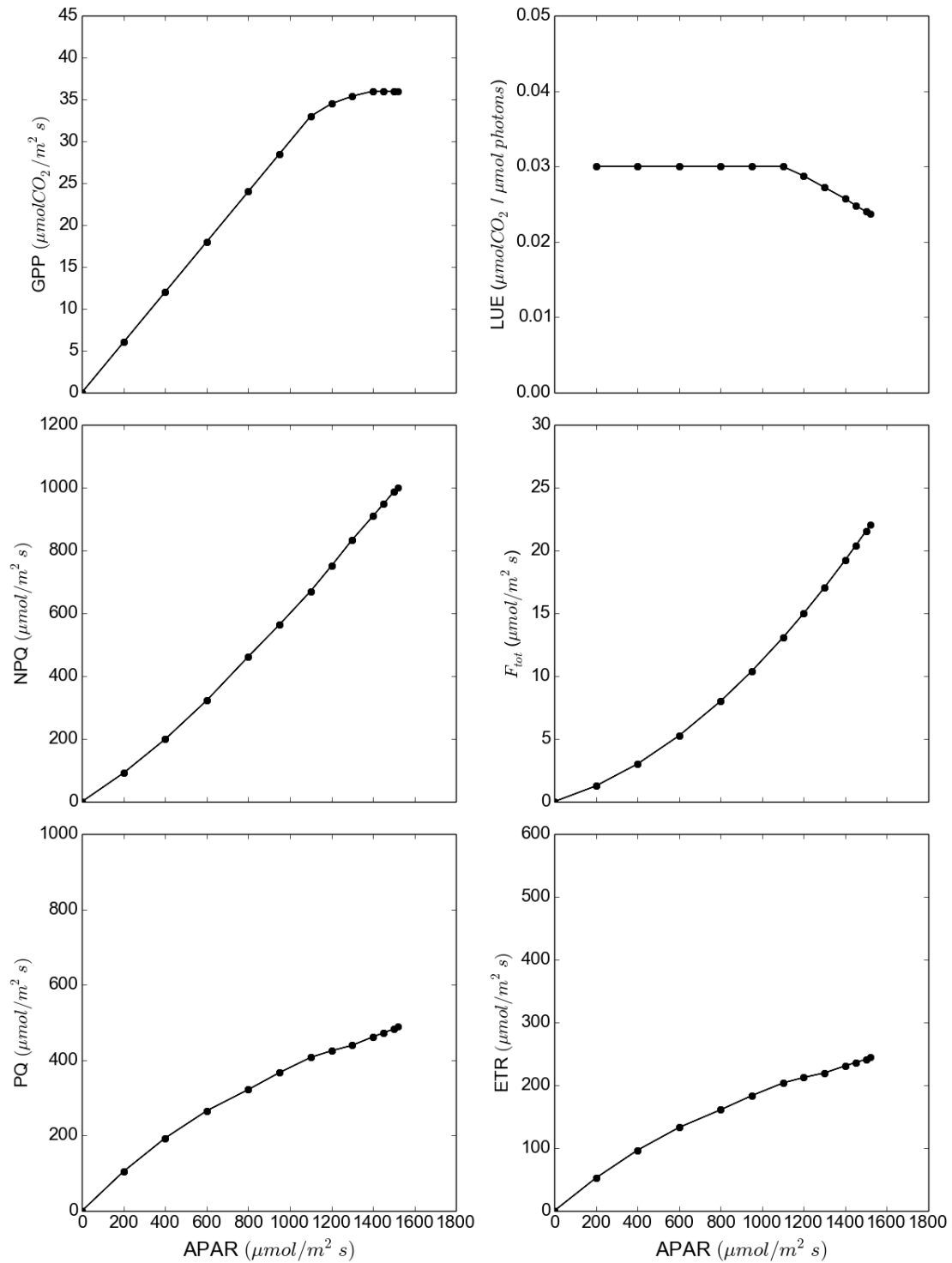


Figure 47: NPQ, F_{tot} , PQ and calculated ETR by the ETR mode. The ETR model was driven by artificial data to test the model for plausibility.

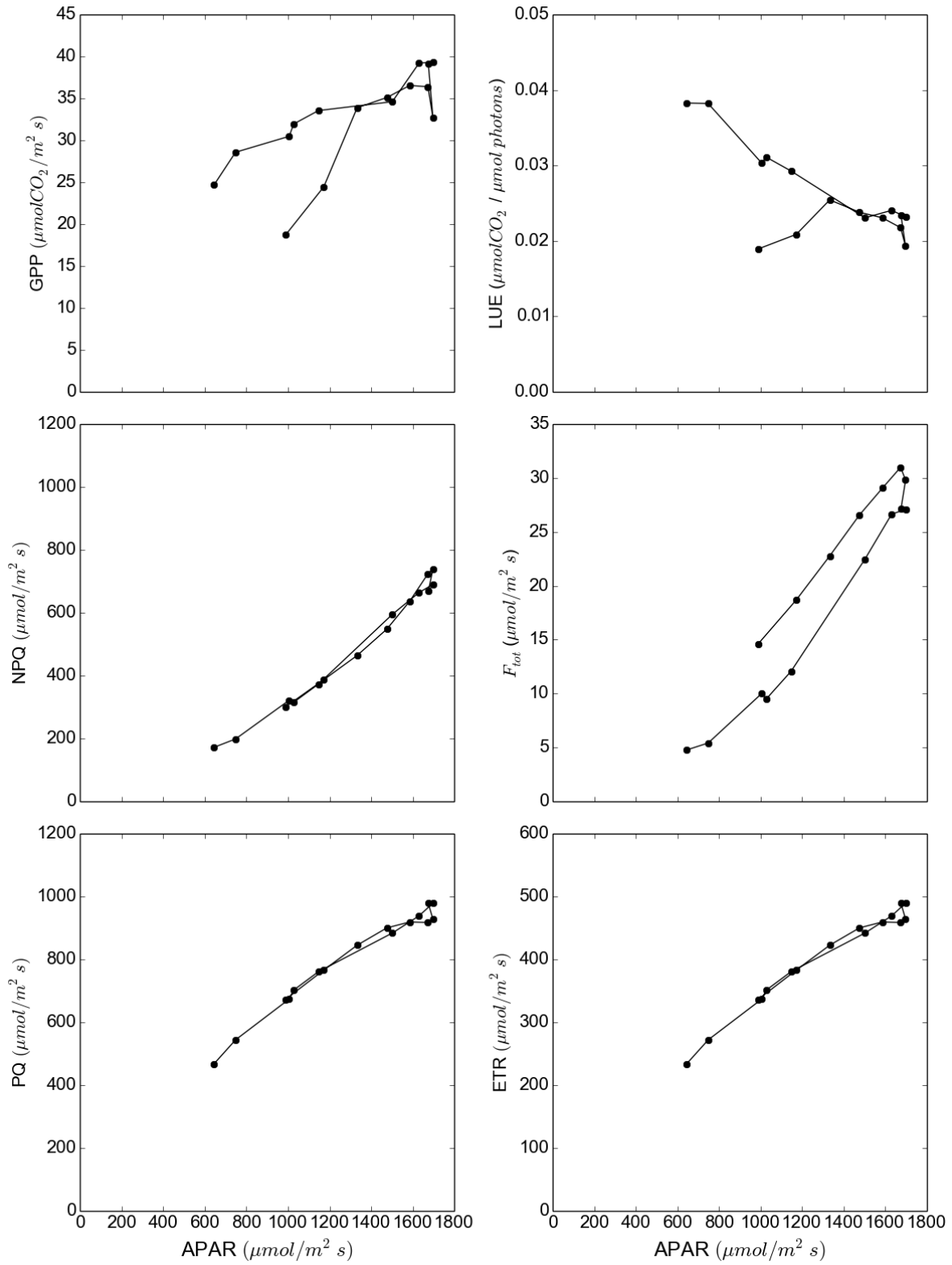


Figure 48: Measured NPQ, F_{tot} , PQ and calculated ETR by the ETR model. The ETR model was driven by SIF-Sys measurements within a sugar beet field on the 30.08.2015 in Merzenhausen, Germany

8. Summary and Conclusion

In this work, the first high resolution maps of red and far-red fluorescence as well as the first continuous ground-based measurements of seasonal red and far-red fluorescence are presented (c.f. Section 3.3.1). The novel LED-based uncertainty estimation of the ground measurement system (*SIF-Sys*) shows that the uncertainty of sun induced fluorescence at 760nm (F_{760}) and especially at 687nm (F_{687}) increases with temperature. A spectral shift between the radiance and irradiance optic was corrected, but surely further increased the overall uncertainty (c.f. Section 5.3). A sufficient cooling and a careful calibration of the measurement system is essential. Since the O₂B band is not as deep and not as well defined as the O₂A band, the retrieval of F_{687} shows a significant higher uncertainty (up to 9.1% for F_{760} and up to 64% for F_{687} daily average error). Measurements with novel systems showed that the uncertainty of the F_{687} retrieval can be reduced by increasing the spectral resolution (c.f. Section 6.7). A higher spectral resolution is also inevitable for the retrieval of the full fluorescence signal. Future technological and methodological advances will allow interpreting the fluorescence signal in its full sense.

It was shown that due to the sensitivity of the photochemical reflectance index (PRI) to the xanthophyll cycle, which in turn is linked to the non-photochemical quenching (NPQ), and the representation of total fluorescence efficiency (F_{yield}) by $F_{760\text{yield}}$ and $F_{687\text{yield}}$, the intra- and inter-daily variations in light use efficiency (LUE) can be best described by a combination of these signals ($R^2 = 0.65$ and 0.89 respectively). The first null hypothesis (“*The additive signal of $F_{760+687\text{yield}}$ does not add information to the prediction of changes in light use efficiency based solely on the PRI*”) can therefore be rejected (c.f. Section 5.2.3 and 5.2.5). Results also showed that the strength of $F_{760\text{yield}}$ and $F_{687\text{yield}}$ and the ratio of F_{687} and F_{760} (F_{ratio}) bring important insights about plant adaptation strategies (c.f. Section 5.2.4 and 5.2.5). It must also be noted, that the PRI and fluorescence are linked to the light reactions, while the LUE is also determined by the dark reactions and the stomata conductance. Therefore, the PRI and fluorescence cannot fully explain the diurnal dynamics of LUE. Nevertheless, the inter-daily relationships between fluorescence parameters, PRI and LUE are much stronger than the diurnal ones. The diurnal dynamics in plant adaptation strategies thus seem to be less important when integrated over a day (c.f. Section 6.2 and 6.3). These findings are important for future experiments concerning the interpretation of satellite-retrieved fluorescence and its link to photosynthesis.

Maps of $F_{760\text{yield}}$ show APAR-independent spatial-temporal changes over the day, with distinct behaviors between crop types. The significant lower values of $F_{760\text{yield}}$ in corn and rapeseed, the fundamentally different behavior of $F_{760\text{yield}}$ in sugar beet and maize during the day, and the changing F_{ratio} in time and between species are strong indicators

of a distinct response of plant species to environmental stress and their F emission (c.f. Section 5.2.6). Spatio-temporal patterns of combined F_{687} and F_{760} estimates and their relationship to APAR significantly contribute to our understanding of canopy structural effects on the re-absorption of F and of the delicate balance between the three competing pathways of photosynthesis, NPQ, and F (c.f. Section 6.3). These findings reject the second null hypothesis: *Spatiotemporal plant adaptation strategies are not detectable within maps of red- and far-red fluorescence*”.

Results contribute evidence that F allows improving estimates of GPP and its dynamics under changing environmental conditions. Due to the direct link between fluorescence and photosynthesis, complementary information compared to commonly used greenness-based remote sensing variables can be retrieved from spectroscopic measurements. The multiple regression model using PRI, $F_{760\text{yield}}$ and $F_{687\text{yield}}$ as predictors of LUE showed best results ($R^2 = 0.55$ and 0.79 for intra- and inter-daily estimations respectively) (c.f. Section 5.5 and 5.6). Supporting the idea that a combination of PRI and fluorescence can be used to access diurnal and seasonal CO_2 assimilation rates (c.f. Section 6.4, 6.5, 6.6). The third null hypothesis (“*The PRI, as a proxy for NPQ, does not improve fluorescence based intra- and inter-daily GPP estimations*”) can therefore be rejected.

In conclusion, this thesis provides evidence that the use of sun induced fluorescence improves estimates of GPP, where in particular the combination of F_{yield} and PRI shows the most promising results. In addition it is was shown that the ratio of red and far-red F and their yields can be potentially used to identifying spatio-temporal plant adaptation strategies in response to environmental stress.

9. Outlook

With the recent selection of FLEX as part of the future Earth Explorer 8 mission by ESA (planned launch in 2022), it can be expected that the availability, quality and spatiotemporal coverage of sun-induced chlorophyll measurements will strongly increase over the next years. More measurements are needed to understand the complex relationship between F, NPQ and photosynthesis of different species and under changing environmental conditions. The results of this work demonstrated the importance of measuring fluorescence in both oxygen absorption bands. It is furthermore recommended to move towards a retrieval of total fluorescence, as it provides more complete information about the state of vegetation.

In this work, the potential for estimating GPP and LUE by using empirical and semi-mechanistic models was shown, where the combination of F and PRI showed to improve the intra- and inter-daily estimation of GPP. Since the PRI is affected by canopy structure and seasonal changes in the pigment pools, the interpretation of the PRI as an indicator for NPQ is difficult. Therefore, new algorithms have to be developed to remove the seasonal degradation of the PRI. In the future, FLEX will provide all relevant parameters identified in this study (F in both peaks and PRI as a proxy for NPQ). This, in combination with additional ground measurements for validation and comparison, yields a high potential to advance our understanding and capability to quantify biosphere dynamics in response to global change. Since fluorescence measured from space suffers from spatiotemporal gaps due to cloud contamination, pure remote sensing based GPP estimates will only be able to track seasonal changes. Process-based land surface models can be used to overcome this problem by either using sun induced chlorophyll fluorescence as observational constrain on photosynthesis (Lee et al., 2015; Parazoo et al., 2014), or using sun-induced chlorophyll fluorescence to improve parameterization of important variables like J_{\max} and $V_{c\max}$. As shown in this work, the use of APAR dependent sun induced chlorophyll fluorescence is problematic, since it can lead to the misinterpretation of the actual photosynthetic activity of the plant. Therefore, it will be necessary to calculate global maps of F_{yield} , which in turn requires high quality information on APAR.

This work highlights the difficulties in interpreting the complex relationship between sun induced chlorophyll fluorescence and photosynthesis on inter- and especially intra-daily timescale, but also shows its potential to improve photosynthesis' estimates. The results found raise the question whether there is enough process-understanding to explain the link between GPP and sun induced chlorophyll fluorescence. Although new insights about the link between GPP and F are presented here, more studies over full growing seasons and within different vegetation types are needed in the future.

Appendix

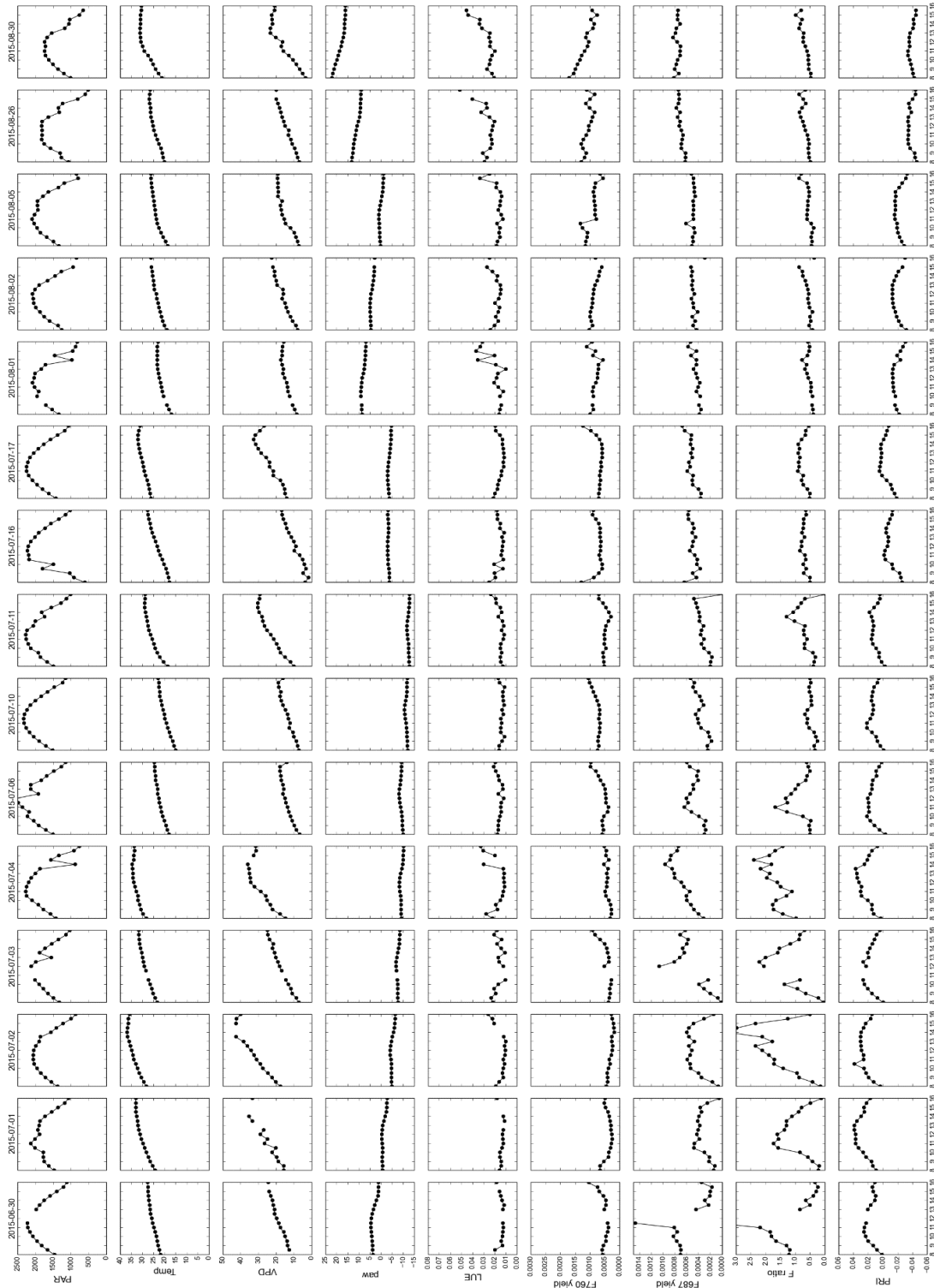


Figure A49: Overview of measured diurnal parameters within sugar beet for all 15 clear sky days in 2015, Merzenhausen, Germany. The photosynthetic active radiation (PAR), temperature and vapor pressure deficit (VPD) were obtained from a meteorological station, the light use efficiency (LUE) was derived from eddy covariance measurements, the plant available water (PAW) was calculated from two soil moisture sensors, the $F_{760\text{yield}}$ and $F_{687\text{yield}}$, the F_{ratio} and the photochemical reflectance index (PRI) were derived from a spectrometer system (SIF-Sys). All measurements were taken within the sugar beet field.

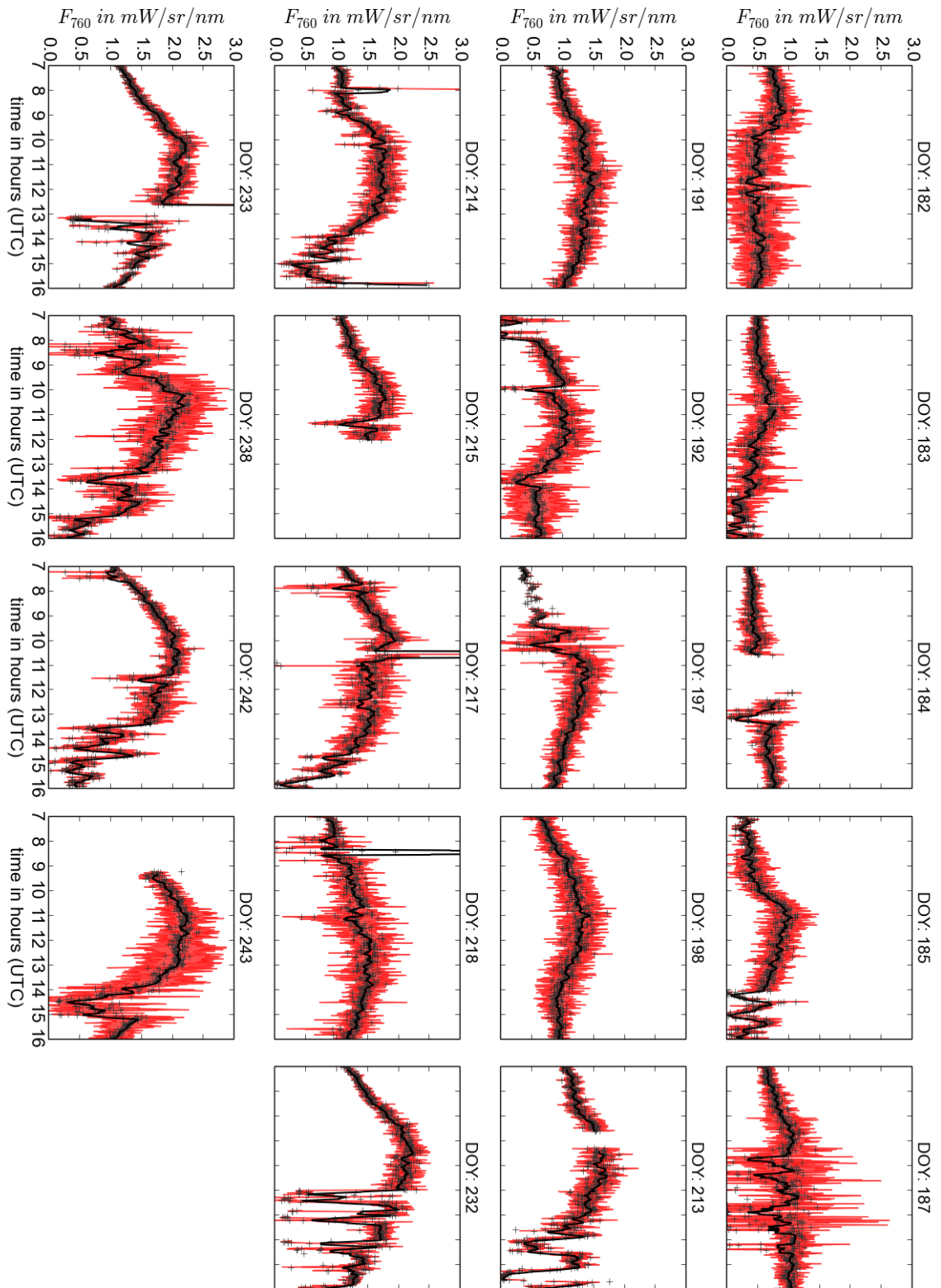


Figure A50: Overview of F_{760} measurements under clear sky condition and resampled to one minute. The red area describes the uncertainty calculated from a LED reference measurement. Measurements were taken in 2015 within a sugar beet field located in Merzenhausen, Germany.

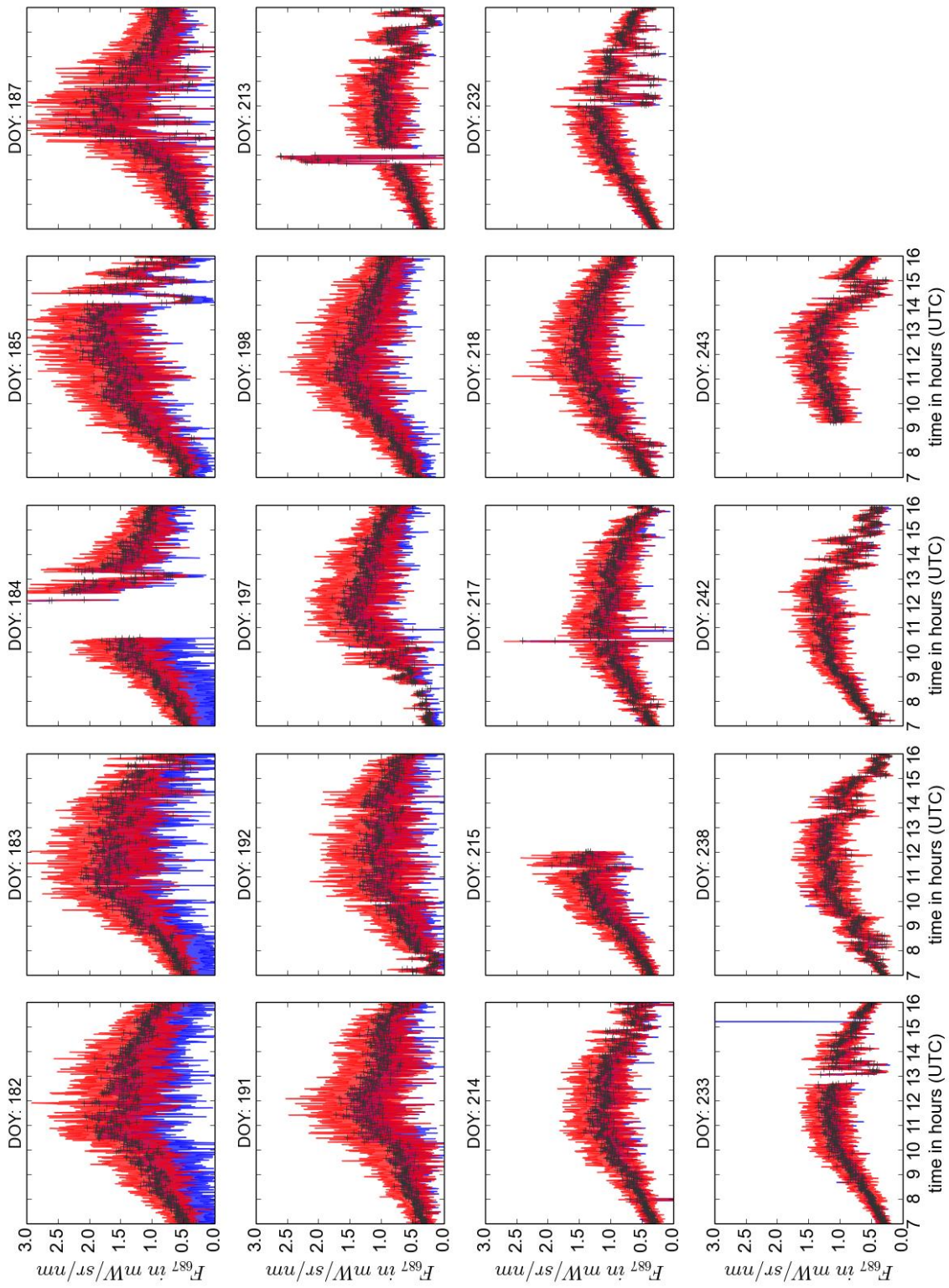


Figure A51: Overview of F_{687} measurements under clear sky condition and resampled to one minute. The red area describes the uncertainty and the blue area describes the overestimation of the F_{687} signal calculated from a LED reference measurement. Measurements were taken in 2015 within a sugar beet field located in Merzenhausen, Germany.

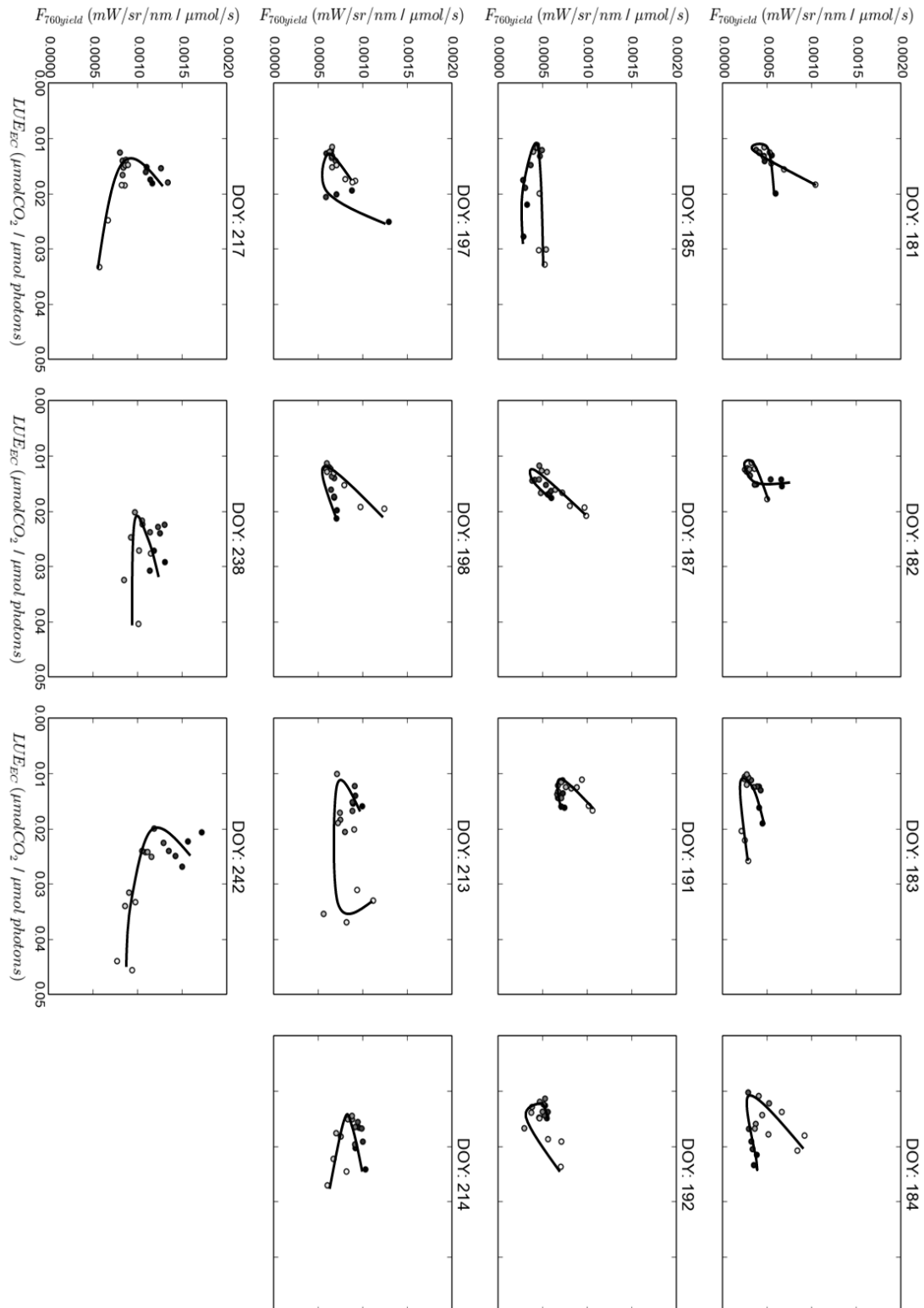


Figure A52: Diurnal relationship between LUE_{EC} and $F_{760yield}$. Black line shows idealized behavior of diurnal relationship. The grayscale indicates the morning (white: 8 a.m.) and afternoon samples (black: 4 p.m.). Measurements were taken in 2015 within a sugar beet field located in Merzenhausen, Germany.

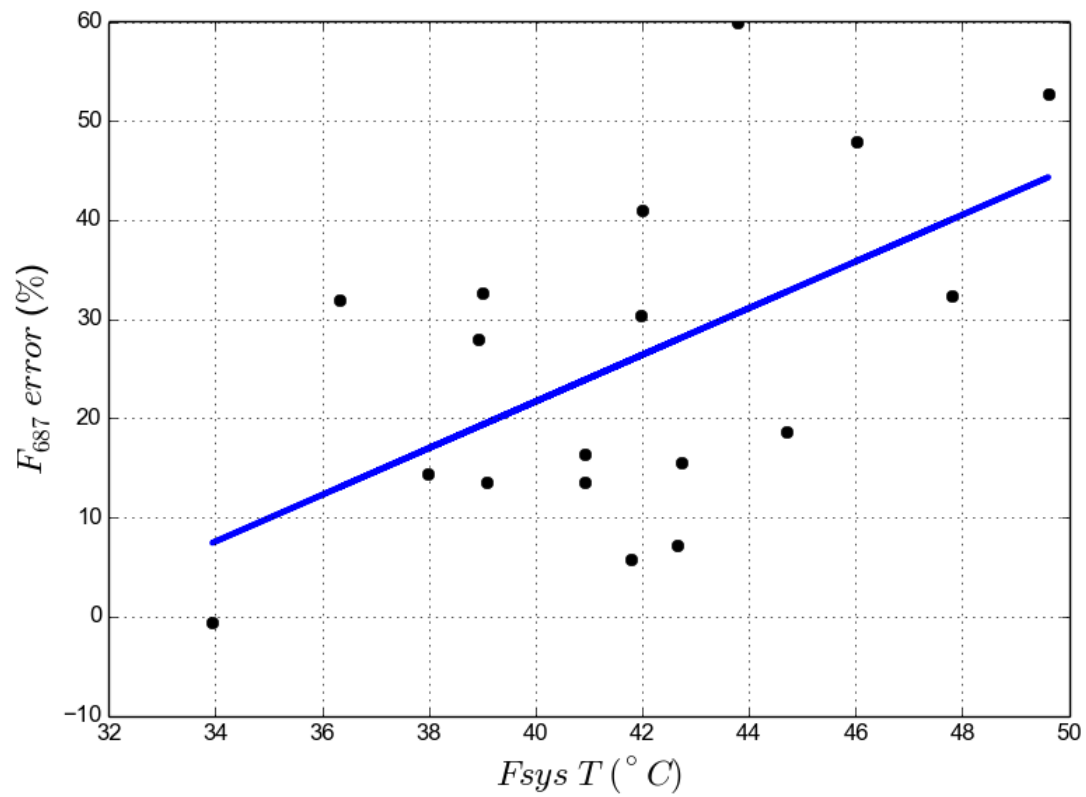


Figure A53: Daily averaged relative F_{687} offset in relationship to temperature within the electronic section of the measurement system SIF-Sys. Measurements were taken in 2015 within a sugar beet field located in Merzenhausen, Germany.

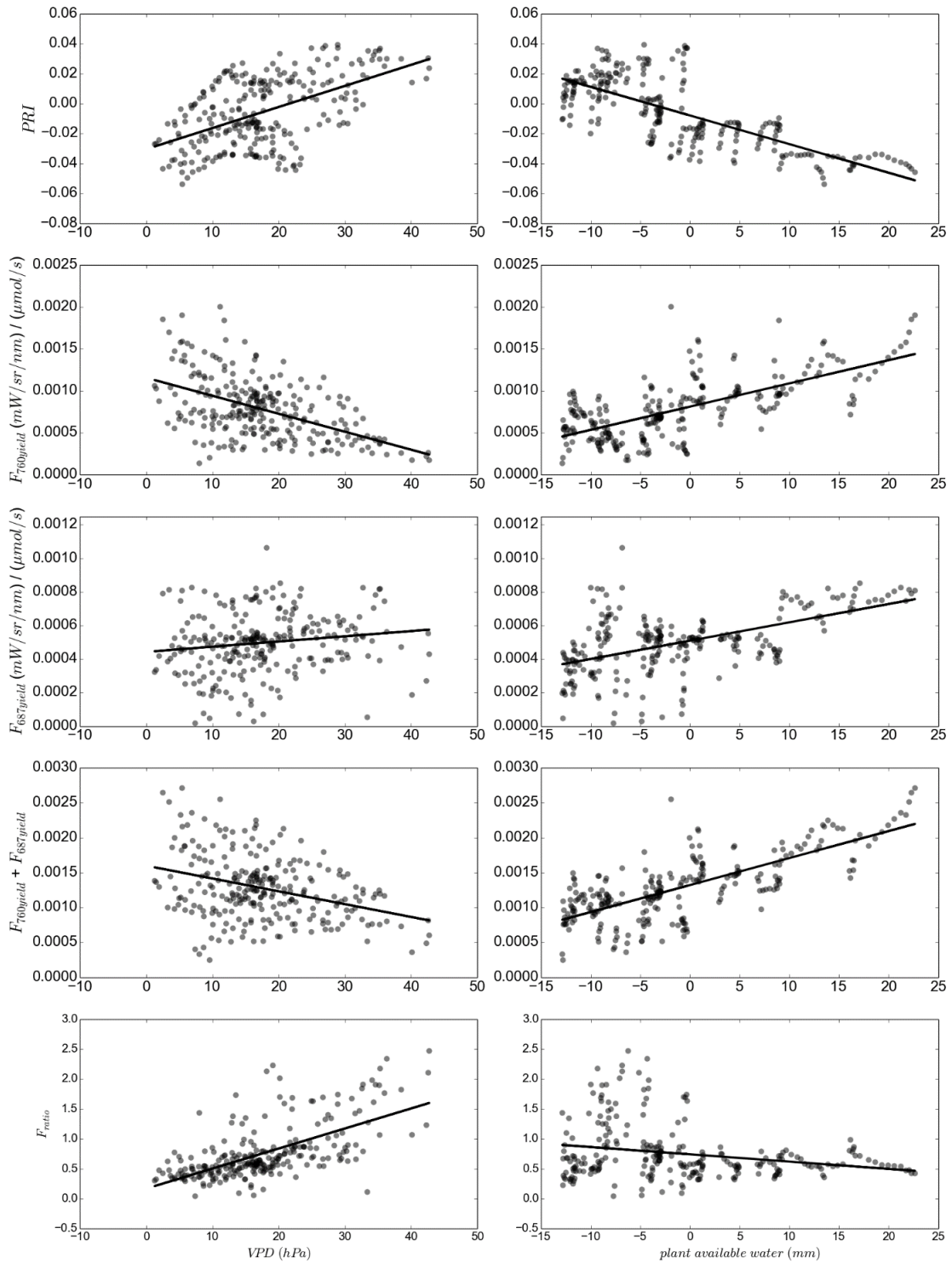


Figure A54: Relationship of 30-min PRI, F_{ratio} and F_{yields} to vapor pressure deficit and plant available water. Small circles indicate: $PAW < 0$ mm; medium circles: $0 \text{ mm} < PAW < 10$ mm; big circles: $PAW > 10$ mm. Black line represent best linear model fit. Measurements were taken in 2015 within a sugar beet field located in Merzenhausen, Germany

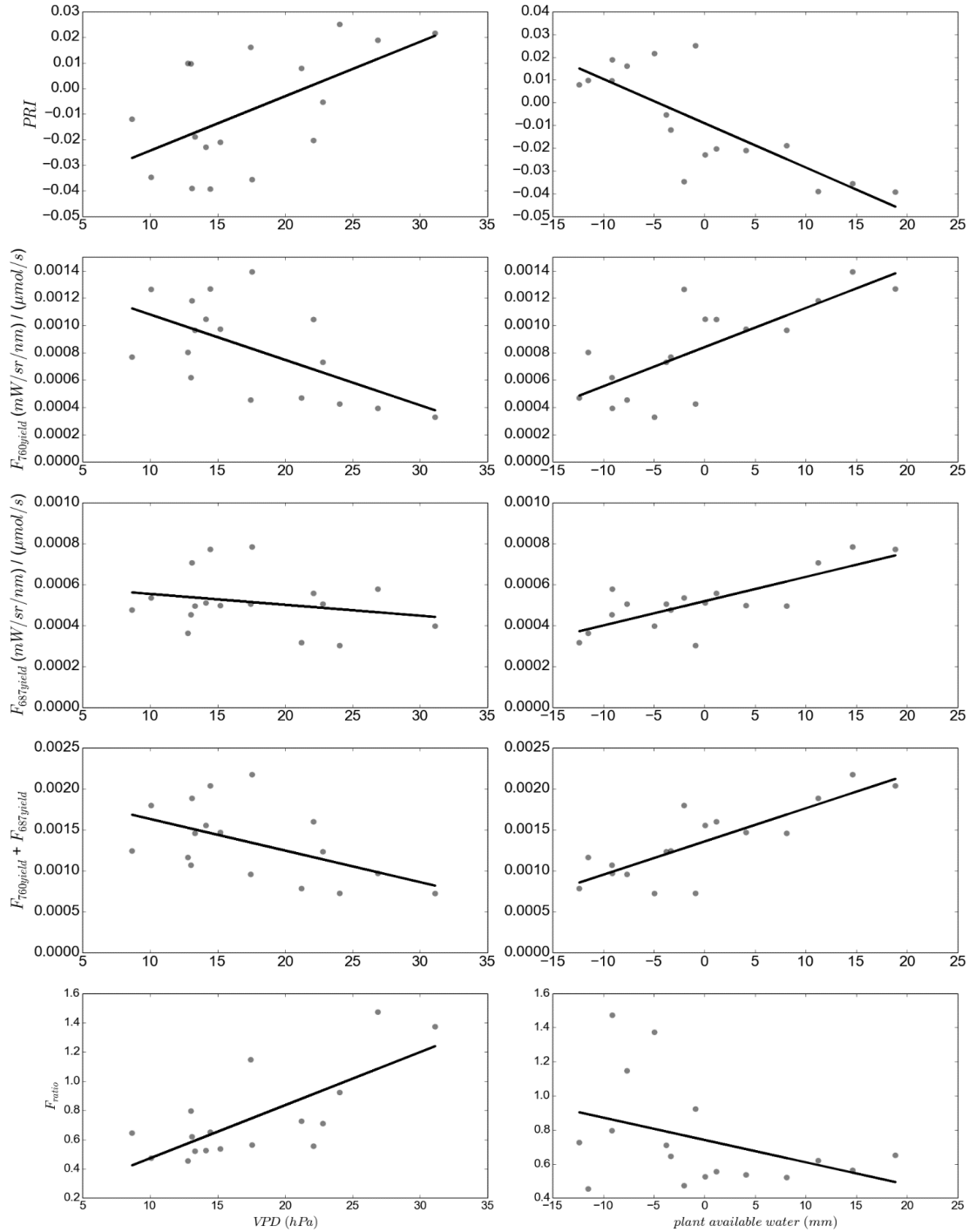


Figure A55: Relationship of daily PRI, F_{ratio} and F_{yields} to vapor pressure deficit and plant available water. Small circles indicate: $PAW < 0$ mm; medium circles: $0 \text{ mm} < PAW < 10$ mm; big circles: $PAW > 10$ mm. Black line represent best linear model fit. Measurements were taken in 2015 within a sugar beet field located in Merzenhausen, Germany.

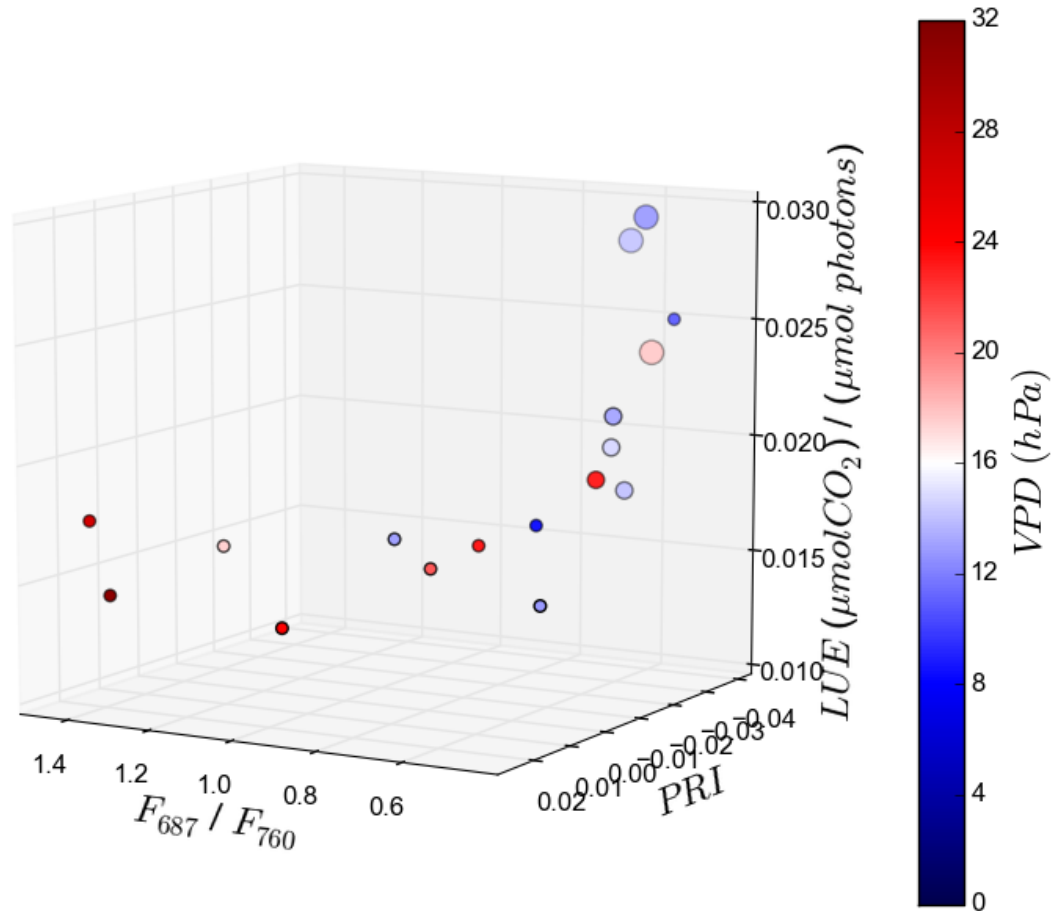


Figure A56: 3 Dimensional plot of daily F_{ratio} , PRI and LUE relationship under changing environmental conditions. Small circles indicate: $PAW < 0$ mm; medium circles: $0 \text{ mm} < PAW < 10$ mm; big circles: $PAW > 10$ mm. Color gradient indicates the vapor pressure deficit. Measurements were taken in 2015 within a sugar beet field located in Merzenhausen, Germany.

Bibliography

- Ač, A., Malenovský, Z., Olejníčková, J., Gallé, A., Rascher, U., Mohammed, G., 2015. Meta-analysis assessing potential of steady-state chlorophyll fluorescence for remote sensing detection of plant water, temperature and nitrogen stress. *Remote Sens. Environ.* 168, 420–436. <https://doi.org/10.1016/j.rse.2015.07.022>
- Adams, W.W., Winter, K., Schreiber, U., Schramel, P., 1990. Photosynthesis and Chlorophyll Fluorescence Characteristics in Relationship to Changes in Pigment and Element Composition of Leaves of *Platanus occidentalis* L. during Autumnal Leaf Senescence. *Plant Physiol.* 92, 1184–1190. <https://doi.org/10.1104/pp.92.4.1184>
- Agati, G., Cerovic, Z.G., Moya, I., 2000. The Effect of Decreasing Temperature up to Chilling Values on the in vivo F685/F735 Chlorophyll Fluorescence Ratio in *Phaseolus vulgaris* and *Pisum sativum*: The Role of the Photosystem I Contribution to the 735 nm Fluorescence Band. *Photochem. Photobiol.* 72, 75–84. [https://doi.org/10.1562/0031-8655\(2000\)0720075TEODTU2.0.CO2](https://doi.org/10.1562/0031-8655(2000)0720075TEODTU2.0.CO2)
- Ahrends, H.E., Haseneder-Lind, R., Schween, J.H., Crewell, S., Stadler, A., Rascher, U., 2014. Diurnal Dynamics of Wheat Evapotranspiration Derived from Ground-Based Thermal Imagery. *Remote Sens.* 6, 9775–9801. <https://doi.org/10.3390/rs6109775>
- Alonso, L., Gomez-Chova, L., Vila-Frances, J., Amoros-Lopez, J., Guanter, L., Calpe, J., Moreno, J., 2008. Improved Fraunhofer Line Discrimination Method for Vegetation Fluorescence Quantification. *IEEE Geosci. Remote Sens. Lett.* 5, 620–624. <https://doi.org/10.1109/LGRS.2008.2001180>
- Antal, T.K., Kovalenko, I.B., Rubin, A.B., Tyystjärvi, E., 2013. Photosynthesis-related quantities for education and modeling. *Photosynth. Res.* 117, 1–30. <https://doi.org/10.1007/s11120-013-9945-8>
- Arena, C., Vitale, L., Santo, A.V.D., 2008. Paraheliotropism in *Robinia pseudoacacia* Plants: An Efficient Means to Cope with Photoinhibition, in: Allen, J.F., Gantt, E., Golbeck, J.H., Osmond, B. (Eds.), *Photosynthesis. Energy from the Sun*. Springer Netherlands, pp. 1403–1406. https://doi.org/10.1007/978-1-4020-6709-9_302
- Baldocchi, D., 2008. ‘Breathing’ of the terrestrial biosphere: lessons learned from a global network of carbon dioxide flux measurement systems. *Aust. J. Bot.* 56, 1–26.
- Baldocchi, D.D., Falge, E., Gu, L., Olson, R., Hollinger, D., Running, S., Anthoni, P., Bernhofer, C., Davis, K., Fuentes, J., Goldstein, A., Katul, G., Law, B., Lee, X., Malhi, Y., Meyers, T., Munger, J.W., Oechel, W., Pilegaard, K., Schmid, H.P., Valentini, R., Verma, S., Vesala, T., Wilson, K., Wofsy, S., 2001. FLUXNET: A new tool to study

- the temporal and spatial variability of ecosystem-scale carbon dioxide, water vapor and energy flux densities. *Bull. Am. Meteorol. Soc.* 82, 2415–2435.
- Bilger, W., Schreiber, U., Bock, M., 1995. Determination of the quantum efficiency of photosystem II and of non-photochemical quenching of chlorophyll fluorescence in the field. *Oecologia* 102, 425–432. <https://doi.org/10.1007/BF00341354>
- Bonan, G.B., 2008. *Ecological Climatology: Concepts and Applications*. Cambridge University Press, New York.
- Bonan, G.B., 1995. Land-Atmosphere interactions for climate system Models: coupling biophysical, biogeochemical, and ecosystem dynamical processes. *Remote Sens. Environ., Remote Sensing of Land Surface for Studies of Global Change* 51, 57–73. [https://doi.org/10.1016/0034-4257\(94\)00065-U](https://doi.org/10.1016/0034-4257(94)00065-U)
- Bonan, G.B., Oleson, K.W., Fisher, R.A., Lasslop, G., Reichstein, M., 2012. Reconciling leaf physiological traits and canopy flux data: Use of the TRY and FLUXNET databases in the Community Land Model version 4. *J. Geophys. Res. Biogeosciences* 117, G02026. <https://doi.org/10.1029/2011JG001913>
- Burkart, A., Schickling, A., Mateo, M.P.C., Wrobel, T.J., Rossini, M., Cogliati, S., Julitta, T., Rascher, U., 2015. A Method for Uncertainty Assessment of Passive Sun-Induced Chlorophyll Fluorescence Retrieval Using an Infrared Reference Light. *IEEE Sens. J.* 15, 4603–4611. <https://doi.org/10.1109/JSEN.2015.2422894>
- Burkart, S., Manderscheid, R., Weigel, H.-J., 2007. Design and performance of a portable gas exchange chamber system for CO₂- and H₂O-flux measurements in crop canopies. *Environ. Exp. Bot.* 61, 25–34. <https://doi.org/10.1016/j.envexpbot.2007.02.007>
- Buschmann, C., 2007. Variability and application of the chlorophyll fluorescence emission ratio red/far-red of leaves. *Photosynth. Res.* 92, 261–271. <https://doi.org/10.1007/s11120-007-9187-8>
- Cendrero-Mateo, M.P., Carmo-Silva, A.E., Porcar-Castell, A., Hamerlynck, E.P., Papuga, S.A., Moran, M.S., 2015. Dynamic response of plant chlorophyll fluorescence to light, water and nutrient availability. *Funct. Plant Biol.* 42, 746–757.
- Cendrero-Mateo, M.P., Moran, M.S., Papuga, S.A., Thorp, K.R., Alonso, L., Moreno, J., Ponce-Campos, G., Rascher, U., Wang, G., 2016. Plant chlorophyll fluorescence: active and passive measurements at canopy and leaf scales with different nitrogen treatments. *J. Exp. Bot.* 67, 275–286. <https://doi.org/10.1093/jxb/erv456>
- Chapin, F.S., Matson, P., Mooney, H.A., 2006. *Principles of Terrestrial Ecosystem Ecology*. Springer Science & Business Media.

- Cheng, Y.-B., Middleton, E.M., Zhang, Q., Huemmrich, K.F., Campbell, P.K.E., Corp, L.A., Cook, B.D., Kustas, W.P., Daughtry, C.S., 2013. Integrating Solar Induced Fluorescence and the Photochemical Reflectance Index for Estimating Gross Primary Production in a Cornfield. *Remote Sens.* 5, 6857–6879. <https://doi.org/10.3390/rs5126857>
- Cogliati, S., Rossini, M., Julitta, T., Meroni, M., Schickling, A., Burkart, A., Pinto, F., Rascher, U., Colombo, R., 2015a. Continuous and long-term measurements of reflectance and sun-induced chlorophyll fluorescence by using novel automated field spectroscopy systems. *Remote Sens. Environ.* 164, 270–281. <https://doi.org/10.1016/j.rse.2015.03.027>
- Cogliati, S., Verhoef, W., Kraft, S., Sabater, N., Alonso, L., Vicent, J., Moreno, J., Drusch, M., Colombo, R., 2015b. Retrieval of sun-induced fluorescence using advanced spectral fitting methods. *Remote Sens. Environ.* 169, 344–357. <https://doi.org/10.1016/j.rse.2015.08.022>
- Damm, A., Elbers, J., Erler, A., Gioli, B., Hamdi, K., Hutjes, R., Kosvancova, M., Meroni, M., Miglietta, F., Moersch, A., Moreno, J., Schickling, A., Sonnenschein, R., Udelhoven, T., Van Der Linden, S., Hostert, P., Rascher, U., 2010a. Remote sensing of sun-induced fluorescence to improve modeling of diurnal courses of gross primary production (GPP). *Glob. Change Biol.* 16, 171–186. <https://doi.org/10.1111/j.1365-2486.2009.01908.x>
- Damm, A., Erler, A., Hillen, W., Meroni, M., Schaepman, M.E., Verhoef, W., Rascher, U., 2011. Modeling the impact of spectral sensor configurations on the FLD retrieval accuracy of sun-induced chlorophyll fluorescence. *Remote Sens. Environ.* 115, 1882–1892. <https://doi.org/10.1016/j.rse.2011.03.011>
- Damm, A., Guanter, L., Laurent, V.C.E., Schaepman, M.E., Schickling, A., Rascher, U., 2014. FLD-based retrieval of sun-induced chlorophyll fluorescence from medium spectral resolution airborne spectroscopy data. *Remote Sens. Environ.* 147, 256–266. <https://doi.org/10.1016/j.rse.2014.03.009>
- Damm, A., Guanter, L., Paul-Limoges, E., van der Tol, C., Hueni, A., Buchmann, N., Eugster, W., Ammann, C., Schaepman, M.E., 2015. Far-red sun-induced chlorophyll fluorescence shows ecosystem-specific relationships to gross primary production: An assessment based on observational and modeling approaches. *Remote Sens. Environ.* 166, 91–105. <https://doi.org/10.1016/j.rse.2015.06.004>
- Damm, A., Schickling, A., Schläpfer, D., Schaepman, M.E., Rascher, U., 2010b. Deriving sun-induced chlorophyll fluorescence from airborne based spectrometer data. ESA. <https://doi.org/10.5167/uzh-35343>

- Dau, H., 1994. Molecular Mechanisms and Quantitative Models of Variable Photosystem II Fluorescence. *Photochem. Photobiol.* 60, 1–23. <https://doi.org/10.1111/j.1751-1097.1994.tb03937.x>
- Demmig-Adams, B., Adams, W.W., 2006. Photoprotection in an ecological context: the remarkable complexity of thermal energy dissipation. *New Phytol.* 172, 11–21. <https://doi.org/10.1111/j.1469-8137.2006.01835.x>
- Denman, K.L., Brasseur, G., Chidthaisong, A., Ciais, P., Cox, P.M., Dickinson, R.E., Hauglustaine, D., Heinze, C., Holland, E., Jacob, D., Lohmann, U., Ramachandran, S., da Silva Dias, P.L., Wofsy, S.C., Zhang, X., 2007. Couplings Between Changes in the Climate System and Biogeochemistry, in: Solomon, S., Qin, D., Manning, M., Chen, Z., Marquis, M., Averyt, K.B., Tignor, M., Miller, H.L. (Eds.), *Climate Change 2007: The Physical Science Basis. Contribution of Working Group I to the Fourth Assessment Report of the Intergovernmental Panel on Climate Change*. Cambridge University Press, Cambridge, United Kingdom and New York, NY, USA., pp. 499–587.
- Drolet, G.G., Middleton, E.M., Huemmrich, K.F., Hall, F.G., Amiro, B.D., Barr, A.G., Black, T.A., McCaughey, J.H., Margolis, H.A., 2008. Regional mapping of gross light-use efficiency using MODIS spectral indices. *Remote Sens. Environ.* 112, 3064–3078. <https://doi.org/10.1016/j.rse.2008.03.002>
- Ehleringer, J., Björkman, O., Mooney, H.A., 1976. Leaf Pubescence: Effects on Absorptance and Photosynthesis in a Desert Shrub. *Science* 192, 376–377. <https://doi.org/10.1126/science.192.4237.376>
- Eichelmann, H., Oja, V., Rasulov, B., Padu, E., Bichele, I., Pettai, H., Mänd, P., Kull, O., Laisk, A., 2005. Adjustment of leaf photosynthesis to shade in a natural canopy: reallocation of nitrogen. *Plant Cell Environ.* 28, 389–401. <https://doi.org/10.1111/j.1365-3040.2004.01275.x>
- Ensminger, I., Busch, F., Huner, N.P.A., 2006. Photostasis and cold acclimation: sensing low temperature through photosynthesis. *Physiol. Plant.* 126, 28–44. <https://doi.org/10.1111/j.1399-3054.2006.00627.x>
- Farquhar, G.D., von Caemmerer, S., Berry, J.A., 2001. Models of Photosynthesis. *Plant Physiol.* 125, 42–45. <https://doi.org/10.1104/pp.125.1.42>
- Farquhar, G.D., von Caemmerer, S., Berry, J.A., 1980. A biochemical model of photosynthetic CO₂ assimilation in leaves of C₃ species. *Planta* 149, 78–90. <https://doi.org/10.1007/BF00386231>
- Fensholt, R., Sandholt, I., Rasmussen, M.S., 2004. Evaluation of MODIS LAI, fAPAR and the relation between fAPAR and NDVI in a semi-arid environment using in situ

measurements. *Remote Sens. Environ.* 91, 490–507.
<https://doi.org/10.1016/j.rse.2004.04.009>

Field, C.B., Randerson, J.T., Malmström, C.M., 1995. Global net primary production: Combining ecology and remote sensing. *Remote Sens. Environ., Remote Sensing of Land Surface for Studies of Global Change* 51, 74–88. [https://doi.org/10.1016/0034-4257\(94\)00066-V](https://doi.org/10.1016/0034-4257(94)00066-V)

Foken, T., 2006. *Angewandte Meteorologie*. Springer Berlin Heidelberg.

Franck, F., Juneau, P., Popovic, R., 2002. Resolution of the Photosystem I and Photosystem II contributions to chlorophyll fluorescence of intact leaves at room temperature. *Biochim. Biophys. Acta BBA - Bioenerg.* 1556, 239–246.
[https://doi.org/10.1016/S0005-2728\(02\)00366-3](https://doi.org/10.1016/S0005-2728(02)00366-3)

Frankenberg, C., Berry, J., Guanter, L., Joiner, J., 2013. Remote sensing of terrestrial chlorophyll fluorescence from space [WWW Document]. URL <http://spie.org/x92267.xml> (accessed 6.11.13).

Frankenberg, C., Fisher, J.B., Worden, J., Badgley, G., Saatchi, S.S., Lee, J.-E., Toon, G.C., Butz, A., Jung, M., Kuze, A., Yokota, T., 2011. New global observations of the terrestrial carbon cycle from GOSAT: Patterns of plant fluorescence with gross primary productivity. *Geophys. Res. Lett.* 38, L17706. <https://doi.org/10.1029/2011GL048738>

Frankenberg, C., O'Dell, C., Berry, J., Guanter, L., Joiner, J., Koehler, P., Pollock, R., Taylor, T.E., 2014. Prospects for chlorophyll fluorescence remote sensing from the Orbiting Carbon Observatory-2. *Remote Sens. Environ.* 147, 1–12.
<https://doi.org/10.1016/j.rse.2014.02.007>

Gamon, J.A., Peñuelas, J., Field, C.B., 1992. A narrow-waveband spectral index that tracks diurnal changes in photosynthetic efficiency. *Remote Sens. Environ.* 41, 35–44.
[https://doi.org/10.1016/0034-4257\(92\)90059-S](https://doi.org/10.1016/0034-4257(92)90059-S)

García, R.L., Norman, J.M., McDermitt, D.K., 1990. Measurements of canopy gas exchange using an open chamber system. *Remote Sens. Rev.* 5, 141–162.
<https://doi.org/10.1080/02757259009532126>

García-Plazaola, J.I., Becerril, J.M., 2001. Seasonal changes in photosynthetic pigments and antioxidants in beech (*Fagus sylvatica*) in a Mediterranean climate: implications for tree decline diagnosis. *Funct. Plant Biol.* 28, 225–232.

Genty, B., Briantais, J.-M., Baker, N.R., 1989. The relationship between the quantum yield of photosynthetic electron transport and quenching of chlorophyll fluorescence. *Biochim. Biophys. Acta BBA - Gen. Subj.* 990, 87–92. [https://doi.org/10.1016/S0304-4165\(89\)80016-9](https://doi.org/10.1016/S0304-4165(89)80016-9)

- Genty, B., Wonders, J., Baker, N.R., 1990. Non-photochemical quenching of F_o in leaves is emission wavelength dependent: consequences for quenching analysis and its interpretation. *Photosynth. Res.* 26, 133–139. <https://doi.org/10.1007/BF00047085>
- Gitelson, A.A., Buschmann, C., Lichtenthaler, H.K., 1998. Leaf chlorophyll fluorescence corrected for re-absorption by means of absorption and reflectance measurements. *J. Plant Physiol.* 152, 283–296. [https://doi.org/10.1016/S0176-1617\(98\)80143-0](https://doi.org/10.1016/S0176-1617(98)80143-0)
- Grace, J., Nichol, C., Disney, M., Lewis, P., Quaife, T., Bowyer, P., 2007. Can we measure terrestrial photosynthesis from space directly, using spectral reflectance and fluorescence? *Glob. Change Biol.* 13, 1484–1497. <https://doi.org/10.1111/j.1365-2486.2007.01352.x>
- Graf, A., Werner, J., Langensiepen, M., van de Boer, A., Schmidt, M., Kupisch, M., Vereecken, H., 2013. Validation of a minimum microclimate disturbance chamber for net ecosystem flux measurements. *Agric. For. Meteorol.* 174–175, 1–14. <https://doi.org/10.1016/j.agrformet.2013.02.001>
- Guanter, L., Frankenberg, C., Dudhia, A., Lewis, P.E., Gómez-Dans, J., Kuze, A., Suto, H., Grainger, R.G., 2012. Retrieval and global assessment of terrestrial chlorophyll fluorescence from GOSAT space measurements. *Remote Sens. Environ.* 121, 236–251. <https://doi.org/10.1016/j.rse.2012.02.006>
- Guanter, L., Zhang, Y., Jung, M., Joiner, J., Voigt, M., Berry, J.A., Frankenberg, C., Huete, A.R., Zarco-Tejada, P., Lee, J.-E., Moran, M.S., Ponce-Campos, G., Beer, C., Camps-Valls, G., Buchmann, N., Gianelle, D., Klumpp, K., Cescatti, A., Baker, J.M., Griffis, T.J., 2014. Global and time-resolved monitoring of crop photosynthesis with chlorophyll fluorescence. *Proc. Natl. Acad. Sci.* 111, E1327–E1333. <https://doi.org/10.1073/pnas.1320008111>
- Haboudane, D., Miller, J.R., Pattey, E., Zarco-Tejada, P.J., Strachan, I.B., 2004. Hyperspectral vegetation indices and novel algorithms for predicting green LAI of crop canopies: Modeling and validation in the context of precision agriculture. *Remote Sens. Environ.* 90, 337–352. <https://doi.org/10.1016/j.rse.2003.12.013>
- Haboudane, D., Miller, J.R., Tremblay, N., Zarco-Tejada, P.J., Dextraze, L., 2002. Integrated narrow-band vegetation indices for prediction of crop chlorophyll content for application to precision agriculture. *Remote Sens. Environ.* 81, 416–426. [https://doi.org/10.1016/S0034-4257\(02\)00018-4](https://doi.org/10.1016/S0034-4257(02)00018-4)
- Hilker, T., Coops, N.C., Wulder, M.A., Black, T.A., Guy, R.D., 2008. The use of remote sensing in light use efficiency based models of gross primary production: A review of current status and future requirements. *Sci. Total Environ.*, BIOGEOCHEMISTRY OF FORESTED ECOSYSTEM - Selected papers from BIOGEMON, the 5th International Symposium on Ecosystem Behaviour, held at the University of

California, Santa Cruz, on June 25–30, 2006 404, 411–423. <https://doi.org/10.1016/j.scitotenv.2007.11.007>

- Huete, A., Didan, K., Miura, T., Rodriguez, E.P., Gao, X., Ferreira, L.G., 2002. Overview of the radiometric and biophysical performance of the MODIS vegetation indices. *Remote Sens. Environ.*, The Moderate Resolution Imaging Spectroradiometer (MODIS): a new generation of Land Surface Monitoring 83, 195–213. [https://doi.org/10.1016/S0034-4257\(02\)00096-2](https://doi.org/10.1016/S0034-4257(02)00096-2)
- Huner, N.P.A., Maxwell, D.P., Gray, G.R., Savitch, L.V., Krol, M., Ivanov, A.G., Falk, S., 1996. Sensing environmental temperature change through imbalances between energy supply and energy consumption: Redox state of photosystem II. *Physiol. Plant.* 98, 358–364. <https://doi.org/10.1034/j.1399-3054.1996.980218.x>
- IPCC, 2013. *Climate Change 2013: The Physical Science Basis. Contribution of Working Group I to the Fifth Assessment Report of the Intergovernmental Panel on Climate Change.*
- Ivanov, A., Sane, P., Zeinalov, Y., Malmberg, G., Gardeström, P., Huner, N., Öquist, G., 2001. Photosynthetic electron transport adjustments in overwintering Scots pine (*Pinus sylvestris* L.). *Planta* 213, 575–585. <https://doi.org/10.1007/s004250100522>
- Jackson, R.D., Moran, M.S., Gay, L.W., Raymond, L.H., 1987. Evaluating evaporation from field crops using airborne radiometry and ground-based meteorological data. *Irrig. Sci.* 8, 81–90. <https://doi.org/10.1007/BF00259473>
- Joiner, J., Yoshida, Y., Vasilkov, A.P., Yoshida, Y., Corp, L.A., Middleton, E.M., 2011. First observations of global and seasonal terrestrial chlorophyll fluorescence from space. *Biogeosciences* 8, 637–651. <https://doi.org/10.5194/bg-8-637-2011>
- Julitta, T., Corp, L.A., Rossini, M., Burkart, A., Cogliati, S., Davies, N., Hom, M., Mac Arthur, A., Middleton, E.M., Rascher, U., Schickling, A., Colombo, R., 2016. Comparison of Sun-Induced Chlorophyll Fluorescence Estimates Obtained from Four Portable Field Spectroradiometers. *Remote Sens.* 8, 122. <https://doi.org/10.3390/rs8020122>
- Jung, M., Reichstein, M., Bondeau, A., 2009. Towards global empirical upscaling of FLUXNET eddy covariance observations: validation of a model tree ensemble approach using a biosphere model. *Biogeosciences* 6, 2001–2013. <https://doi.org/10.5194/bg-6-2001-2009>
- Jung, M., Reichstein, M., Margolis, H.A., Cescatti, A., Richardson, A.D., Arain, M.A., Arneth, A., Bernhofer, C., Bonal, D., Chen, J., Gianelle, D., Gobron, N., Kiely, G., Kutsch, W., Lasslop, G., Law, B.E., Lindroth, A., Merbold, L., Montagnani, L., Moors, E.J., Papale, D., Sottocornola, M., Vaccari, F., Williams, C., 2011. Global patterns of land-atmosphere fluxes of carbon dioxide, latent heat, and sensible heat derived from eddy

- covariance, satellite, and meteorological observations. *J. Geophys. Res. Biogeosciences* 116, G00J07. <https://doi.org/10.1029/2010JG001566>
- Kadioglu, A., Terzi, R., Saruhan, N., Saglam, A., 2012. Current advances in the investigation of leaf rolling caused by biotic and abiotic stress factors. *Plant Sci., Abiotic stress tolerances* 182, 42–48. <https://doi.org/10.1016/j.plantsci.2011.01.013>
- Lange, O., 1962. Eine “Klapp-Küvette” zur CO₂-Gaswechselregistrierung an Blättern von Freilandpflanzen mit dem URAS. *Ber. Deut. Bot. Ges.* 75, 41–50.
- Langensiepen, M., Kupisch, M., van Wijk, M.T., Ewert, F., 2012. Analyzing transient closed chamber effects on canopy gas exchange for optimizing flux calculation timing. *Agric. For. Meteorol.* 164, 61–70. <https://doi.org/10.1016/j.agrformet.2012.05.006>
- LANUV NRW, 2014. *Klimaatlas NRW*.
- Lawlor, D.W., 2001. *Photosynthesis: Molecular, Physiological and Environmental Processes*. BIOS Scientific Publishers.
- Lee, J.-E., Berry, J.A., van der Tol, C., Yang, X., Guanter, L., Damm, A., Baker, I., Frankenberg, C., 2015. Simulations of chlorophyll fluorescence incorporated into the Community Land Model version 4. *Glob. Change Biol.* 21, 3469–3477. <https://doi.org/10.1111/gcb.12948>
- Livingston, G.P., Hutchinson, G.L., 1995. Enclosure-based measurement of trace gas exchange: application and source of error, in: *Biogenic Trace Gases: Measuring Emissions from Soil and Water*. Blackwell Science, Oxford.
- Lu, C., Lu, Q., Zhang, J., Kuang, T., 2001. Characterization of photosynthetic pigment composition, photosystem II photochemistry and thermal energy dissipation during leaf senescence of wheat plants grown in the field. *J. Exp. Bot.* 52, 1805–1810. <https://doi.org/10.1093/jexbot/52.362.1805>
- Maier, S.W., Günther, K.P., Stellmes, M., 2003. Sun-Induced Fluorescence: A New Tool for Precision Farming. *Digit. Imaging Spectr. Tech. Appl. Precis. Agric. Crop Physiol.* *asaspecialpubli*, 209–222. <https://doi.org/10.2134/asaspecpub66.c16>
- Martin, B., Måtensson, O., Öquist, G., 1978. Seasonal Effects on Photosynthetic Electron Transport and Fluorescence Properties in Isolated Chloroplasts of *Pinus silvestris*. *Physiol. Plant.* 44, 102–109. <https://doi.org/10.1111/j.1399-3054.1978.tb01622.x>
- Meroni, M., Busetto, L., Colombo, R., Guanter, L., Moreno, J., Verhoef, W., 2010. Performance of Spectral Fitting Methods for vegetation fluorescence quantification. *Remote Sens. Environ.* 114, 363–374. <https://doi.org/10.1016/j.rse.2009.09.010>

- Meroni, M., Colombo, R., 2006. Leaf level detection of solar induced chlorophyll fluorescence by means of a subnanometer resolution spectroradiometer. *Remote Sens. Environ.* 103, 438–448. <https://doi.org/10.1016/j.rse.2006.03.016>
- Meroni, M., Rossini, M., Guanter, L., Alonso, L., Rascher, U., Colombo, R., Moreno, J., 2009a. Remote sensing of solar-induced chlorophyll fluorescence: Review of methods and applications. *Remote Sens. Environ.* 113, 2037–2051. <https://doi.org/10.1016/j.rse.2009.05.003>
- Meroni, M., Rossini, M., Guanter, L., Alonso, L., Rascher, U., Colombo, R., Moreno, J., 2009b. Remote sensing of solar-induced chlorophyll fluorescence: Review of methods and applications. *Remote Sens. Environ.* 113, 2037–2051. <https://doi.org/10.1016/j.rse.2009.05.003>
- Meroni, M., Rossini, M., Picchi, V., Panigada, C., Cogliati, S., Nali, C., Colombo, R., 2008. Assessing Steady-state Fluorescence and PRI from Hyperspectral Proximal Sensing as Early Indicators of Plant Stress: The Case of Ozone Exposure. *Sensors* 8, 1740–1754. <https://doi.org/10.3390/s8031740>
- Meyer, Y., Buchanan, B.B., Vignols, F., Reichheld, J.-P., 2009. Thioredoxins and Glutaredoxins: Unifying Elements in Redox Biology. *Annu. Rev. Genet.* 43, 335–367. <https://doi.org/10.1146/annurev-genet-102108-134201>
- Monteith, J.L., 1972. Solar Radiation and Productivity in Tropical Ecosystems. *J. Appl. Ecol.* 9, 747–766. <https://doi.org/10.2307/2401901>
- Monteith, J.L., Moss, C.J., 1977. Climate and the Efficiency of Crop Production in Britain [and Discussion]. *Philos. Trans. R. Soc. Lond. B. Biol. Sci.* 281, 277–294. <https://doi.org/10.2307/2417832>
- Moya, I., Camenen, L., Evain, S., Goulas, Y., Cerovic, Z.G., Latouche, G., Flexas, J., Ounis, A., 2004. A new instrument for passive remote sensing: 1. Measurements of sunlight-induced chlorophyll fluorescence. *Remote Sens. Environ.* 91, 186–197. <https://doi.org/10.1016/j.rse.2004.02.012>
- Norman, J.M., Kucharik, C.J., Gower, S.T., Baldocchi, D.D., Crill, P.M., Rayment, M., Savage, K., Striegl, R.G., 1997. A comparison of six methods for measuring soil-surface carbon dioxide fluxes. *J. Geophys. Res. Atmospheres* 102, 28771–28777. <https://doi.org/10.1029/97JD01440>
- Ögren, E., Öquist, G., 1984. Photoinhibition of photosynthesis in *Lemna gibba* as induced by the interaction between light and temperature. III. Chlorophyll fluorescence at 77 K. *Physiol. Plant.* 62, 193–200. <https://doi.org/10.1111/j.1399-3054.1984.tb00370.x>
- Ozanne, C.M.P., Anhof, D., Boulter, S.L., Keller, M., Kitching, R.L., Körner, C., Meinzer, F.C., Mitchell, A.W., Nakashizuka, T., Dias, P.L.S., Stork, N.E., Wright, S.J.,

- Yoshimura, M., 2003. Biodiversity Meets the Atmosphere: A Global View of Forest Canopies. *Science* 301, 183–186. <https://doi.org/10.1126/science.1084507>
- Papale, D., Valentini, R., 2003. A new assessment of European forests carbon exchanges by eddy fluxes and artificial neural network spatialization. *Glob. Change Biol.* 9, 525–535. <https://doi.org/10.1046/j.1365-2486.2003.00609.x>
- Parazoo, N.C., Bowman, K., Fisher, J.B., Frankenberg, C., Jones, D.B.A., Cescatti, A., Pérez-Priego, Ó., Wohlfahrt, G., Montagnani, L., 2014. Terrestrial gross primary production inferred from satellite fluorescence and vegetation models. *Glob. Change Biol.* 20, 3103–3121. <https://doi.org/10.1111/gcb.12652>
- Peguero-Pina, J.J., Morales, F., Flexas, J., Gil-Pelegrín, E., Moya, I., 2008. Photochemistry, remotely sensed physiological reflectance index and de-epoxidation state of the xanthophyll cycle in *Quercus coccifera* under intense drought. *Oecologia* 156, 1–11. <https://doi.org/10.1007/s00442-007-0957-y>
- Peterson, R.B., Oja, V., Laisk, A., 2001. Chlorophyll fluorescence at 680 and 730 nm and leaf photosynthesis. *Photosynth. Res.* 70, 185–196. <https://doi.org/10.1023/A:1017952500015>
- Pfündel, E., 1998. Estimating the contribution of Photosystem I to total leaf chlorophyll fluorescence. *Photosynth. Res.* 56, 185–195. <https://doi.org/10.1023/A:1006032804606>
- Pfündel, E., Agati, G., Cerovic, Z., 2008. Optical properties of plant surfaces, in: *Annual Plant Reviews, Biology of the Plant Cuticle*. Blackwell Publishing.
- Plascyk, J.A., 1975. The MK II Fraunhofer Line Discriminator (FLD-II) for Airborne and Orbital Remote Sensing of Solar-Stimulated Luminescence. *Opt. Eng.* 14, 339–0. <https://doi.org/10.1117/12.7971842>
- Plascyk, J.A., Gabriel, F.C., 1975. The Fraunhofer Line Discriminator MKII-An Airborne Instrument for Precise and Standardized Ecological Luminescence Measurement. *IEEE Trans. Instrum. Meas.* 24, 306–313. <https://doi.org/10.1109/TIM.1975.4314448>
- Porcar-Castell, A., 2011. A high-resolution portrait of the annual dynamics of photochemical and non-photochemical quenching in needles of *Pinus sylvestris*. *Physiol. Plant.* 143, 139–153. <https://doi.org/10.1111/j.1399-3054.2011.01488.x>
- Porcar-Castell, A., Garcia-Plazaola, J.I., Nichol, C.J., Kolari, P., Olascoaga, B., Kuusinen, N., Fernández-Marín, B., Pulkkinen, M., Juurola, E., Nikinmaa, E., 2012. Physiology of the seasonal relationship between the photochemical reflectance index and photosynthetic light use efficiency. *Oecologia* 170, 313–323. <https://doi.org/10.1007/s00442-012-2317-9>

- Porcar-Castell, A., Tyystjärvi, E., Atherton, J., Tol, C. van der, Flexas, J., Pfündel, E.E., Moreno, J., Frankenberg, C., Berry, J.A., 2014. Linking chlorophyll a fluorescence to photosynthesis for remote sensing applications: mechanisms and challenges. *J. Exp. Bot.* eru191. <https://doi.org/10.1093/jxb/eru191>
- Rahimzadeh-Bajgiran, P., Munehiro, M., Omasa, K., 2012. Relationships between the photochemical reflectance index (PRI) and chlorophyll fluorescence parameters and plant pigment indices at different leaf growth stages. *Photosynth. Res.* 113, 261–271. <https://doi.org/10.1007/s11120-012-9747-4>
- Rascher, U., Alonso, L., Burkart, A., Cilia, C., Cogliati, S., Colombo, R., Damm, A., Drusch, M., Guanter, L., Hanus, J., Hyvärinen, T., Julitta, T., Jussila, J., Kataja, K., Kokkalis, P., Kraft, S., Kraska, T., Matveeva, M., Moreno, J., Muller, O., Panigada, C., Pöhl, M., Pinto, F., Prey, L., Pude, R., Rossini, M., Schickling, A., Schurr, U., Schüttemeyer, D., Verrelst, J., Zemek, F., 2015. Sun-induced fluorescence - a new probe of photosynthesis: First maps from the imaging spectrometer HyPlant. *Glob. Change Biol.* <https://doi.org/10.1111/gcb.13017>
- Rawls, W.J., Brakensiek, D.L., 1989. Estimation of Soil Water Retention and Hydraulic Properties, in: Morel-Seytoux, H.J. (Ed.), *Unsaturated Flow in Hydrologic Modeling*, NATO ASI Series. Springer Netherlands, pp. 275–300. https://doi.org/10.1007/978-94-009-2352-2_10
- Reichstein, M., Falge, E., Baldocchi, D., Papale, D., Aubinet, M., Berbigier, P., Bernhofer, C., Buchmann, N., Gilmanov, T., Granier, A., Grünwald, T., Havránková, K., Ilvesniemi, H., Janous, D., Knohl, A., Laurila, T., Lohila, A., Loustau, D., Matteucci, G., Meyers, T., Miglietta, F., Ourcival, J.-M., Pumpanen, J., Rambal, S., Rotenberg, E., Sanz, M., Tenhunen, J., Seufert, G., Vaccari, F., Vesala, T., Yakir, D., Valentini, R., 2005. On the separation of net ecosystem exchange into assimilation and ecosystem respiration: review and improved algorithm. *Glob. Change Biol.* 11, 1424–1439. <https://doi.org/10.1111/j.1365-2486.2005.001002.x>
- Reicosky, D.C., 1990. Canopy gas exchange in the field: Closed chambers. *Remote Sens. Rev.* 5, 163–177. <https://doi.org/10.1080/02757259009532127>
- Rogers, A., 2014. The use and misuse of $V(c,max)$ in Earth System Models. *Photosynth. Res.* 119, 15–29. <https://doi.org/10.1007/s11120-013-9818-1>
- Rossini, M., Meroni, M., Celesti, M., Cogliati, S., Julitta, T., Panigada, C., Rascher, U., van der Tol, C., Colombo, R., 2016. Analysis of Red and Far-Red Sun-Induced Chlorophyll Fluorescence and Their Ratio in Different Canopies Based on Observed and Modeled Data. *Remote Sens.* 8, 412. <https://doi.org/10.3390/rs8050412>
- Rossini, M., Meroni, M., Migliavacca, M., Manca, G., Cogliati, S., Busetto, L., Picchi, V., Cescatti, A., Seufert, G., Colombo, R., 2010. High resolution field spectroscopy

- measurements for estimating gross ecosystem production in a rice field. *Agric. For. Meteorol.* 150, 1283–1296. <https://doi.org/10.1016/j.agrformet.2010.05.011>
- Rossini, M., Nedbal, L., Guanter, L., Ač, A., Alonso, L., Burkart, A., Cogliati, S., Colombo, R., Damm, A., Drusch, M., Hanus, J., Janoutova, R., Julitta, T., Kokkalis, P., Moreno, J., Novotny, J., Panigada, C., Pinto, F., Schickling, A., Schüttemeyer, D., Zemek, F., Rascher, U., 2015. Red and far red Sun-induced chlorophyll fluorescence as a measure of plant photosynthesis. *Geophys. Res. Lett.* 42, 2014GL062943. <https://doi.org/10.1002/2014GL062943>
- Rouse, J.W., 1974. Monitoring the vernal advancement and retrogradation (green wave effect) of natural vegetation.
- Rudolph, S., van der Kruk, J., von Hebel, C., Ali, M., Herbst, M., Montzka, C., Pätzold, S., Robinson, D.A., Vereecken, H., Weihermüller, L., 2015. Linking satellite derived LAI patterns with subsoil heterogeneity using large-scale ground-based electromagnetic induction measurements. *Geoderma* 241–242, 262–271. <https://doi.org/10.1016/j.geoderma.2014.11.015>
- Rumeau, D., Peltier, G., Cournac, L., 2007. Chlororespiration and cyclic electron flow around PSI during photosynthesis and plant stress response. *Plant Cell Environ.* 30, 1041–1051. <https://doi.org/10.1111/j.1365-3040.2007.01675.x>
- Running, S.W., Nemani, R.R., Heinsch, F.A., Zhao, M., Reeves, M., Hashimoto, H., 2004. A Continuous Satellite-Derived Measure of Global Terrestrial Primary Production. *BioScience* 54, 547–560. [https://doi.org/10.1641/0006-3568\(2004\)054\[0547:ACSMOG\]2.0.CO;2](https://doi.org/10.1641/0006-3568(2004)054[0547:ACSMOG]2.0.CO;2)
- Ryu, Y., Baldocchi, D.D., Kobayashi, H., van Ingen, C., Li, J., Black, T.A., Beringer, J., van Gorsel, E., Knohl, A., Law, B.E., Rouspard, O., 2011. Integration of MODIS land and atmosphere products with a coupled-process model to estimate gross primary productivity and evapotranspiration from 1 km to global scales. *Glob. Biogeochem. Cycles* 25, GB4017. <https://doi.org/10.1029/2011GB004053>
- Schickling, A., 2012. Remote sensing of sun-induced fluorescence for improved modeling of gross primary productivity in a heterogeneous agricultural area (No. PreJuSER-20447). *Troposphäre*.
- Schimel, D., Pavlick, R., Fisher, J.B., Asner, G.P., Saatchi, S., Townsend, P., Miller, C., Frankenberg, C., Hibbard, K., Cox, P., 2015. Observing terrestrial ecosystems and the carbon cycle from space. *Glob. Change Biol.* 21, 1762–1776. <https://doi.org/10.1111/gcb.12822>
- Schreiber, U., 2004. Pulse-Amplitude-Modulation (PAM) Fluorometry and Saturation Pulse Method: An Overview, in: Papageorgiou, G.C., Govindjee (Eds.), *Chlorophyll a*

Fluorescence, *Advances in Photosynthesis and Respiration*. Springer Netherlands, pp. 279–319. https://doi.org/10.1007/978-1-4020-3218-9_11

Seneviratne, S.I., Lüthi, D., Litschi, M., Schär, C., 2006. Land–atmosphere coupling and climate change in Europe. *Nature* 443, 205–209. <https://doi.org/10.1038/nature05095>

Sitch, S., Smith, B., Prentice, I.C., Arneth, A., Bondeau, A., Cramer, W., Kaplan, J.O., Levis, S., Lucht, W., Sykes, M.T., Thonicke, K., Venevsky, S., 2003. Evaluation of ecosystem dynamics, plant geography and terrestrial carbon cycling in the LPJ dynamic global vegetation model. *Glob. Change Biol.* 9, 161–185. <https://doi.org/10.1046/j.1365-2486.2003.00569.x>

Stadler, A., Rudolph, S., Kupisch, M., Langensiepen, M., van der Kruk, J., Ewert, F., 2015. Quantifying the effects of soil variability on crop growth using apparent soil electrical conductivity measurements. *Eur. J. Agron.* 64, 8–20. <https://doi.org/10.1016/j.eja.2014.12.004>

Steduto, P., Çetinkökü, Ö., Albrizio, R., Kanber, R., 2002. Automated closed-system canopy-chamber for continuous field-crop monitoring of CO₂ and H₂O fluxes. *Agric. For. Meteorol.* 111, 171–186. [https://doi.org/10.1016/S0168-1923\(02\)00023-0](https://doi.org/10.1016/S0168-1923(02)00023-0)

Stull, R.B. (Ed.), 1988. *An Introduction to Boundary Layer Meteorology*. Springer Netherlands, Dordrecht.

Stylinski, C.D., Gamon, J.A., Oechel, W.C., 2002. Seasonal Patterns of Reflectance Indices, Carotenoid Pigments and Photosynthesis of Evergreen Chaparral Species. *Oecologia* 131, 366–374.

Turner, D.P., Ritts, W.D., Cohen, W.B., Gower, S.T., Zhao, M., Running, S.W., Wofsy, S.C., Urbanski, S., Dunn, A.L., Munger, J.W., 2003. Scaling Gross Primary Production (GPP) over boreal and deciduous forest landscapes in support of MODIS GPP product validation. *Remote Sens. Environ.* 88, 256–270. <https://doi.org/10.1016/j.rse.2003.06.005>

van der Tol, C., J.a. Berry, P.k.e. Campbell, U. Rascher, 2014. Models of fluorescence and photosynthesis for interpreting measurements of solar induced chlorophyll fluorescence. *J. Geophys. Res. Biogeosciences* 2014JG002713. <https://doi.org/10.1002/2014JG002713>

van der Tol, C., Verhoef, W., Timmermans, J., Verhoef, A., Su, Z., 2009. An integrated model of soil-canopy spectral radiances, photosynthesis, fluorescence, temperature and energy balance. *Biogeosciences* 6, 3109–3129. <https://doi.org/10.5194/bg-6-3109-2009>

- Van Der Werf, G.R., Randerson, J.T., Collatz, G.J., Giglio, L., 2003. Carbon emissions from fires in tropical and subtropical ecosystems. *Glob. Change Biol.* 9, 547–562. <https://doi.org/10.1046/j.1365-2486.2003.00604.x>
- Verhoeven, A., 2014. Sustained energy dissipation in winter evergreens. *New Phytol.* 201, 57–65. <https://doi.org/10.1111/nph.12466>
- Verrelst, J., van der Tol, C., Magnani, F., Sabater, N., Rivera, J.P., Mohammed, G., Moreno, J., 2016. Evaluating the predictive power of sun-induced chlorophyll fluorescence to estimate net photosynthesis of vegetation canopies: A SCOPE modeling study. *Remote Sens. Environ.* 176, 139–151. <https://doi.org/10.1016/j.rse.2016.01.018>
- Walters, R.G., 2005. Towards an understanding of photosynthetic acclimation. *J. Exp. Bot.* 56, 435–447. <https://doi.org/10.1093/jxb/eri060>
- Wang, K., Liu, C., Zheng, X., Pihlatie, M., Li, B., Haapanala, S., Vesala, T., Liu, H., Wang, Y., Liu, G., Hu, F., 2013. Comparison between eddy covariance and automatic chamber techniques for measuring net ecosystem exchange of carbon dioxide in cotton and wheat fields. *Biogeosciences* 10, 6865–6877. <https://doi.org/10.5194/bg-10-6865-2013>
- Weihermüller, L., Huisman, J.A., Lambot, S., Herbst, M., Vereecken, H., 2007. Mapping the spatial variation of soil water content at the field scale with different ground penetrating radar techniques. *J. Hydrol.* 340, 205–216. <https://doi.org/10.1016/j.jhydrol.2007.04.013>
- Weng, J., Chen, Y., Liao, T., 2006. Relationships between chlorophyll fluorescence parameters and photochemical reflectance index of tree species adapted to different temperature regimes. *Funct. Plant Biol.* 33, 241–246.
- Wieneke, S., Ahrends, H., Damm, A., Pinto, F., Stadler, A., Rossini, M., Rascher, U., 2016. Airborne based spectroscopy of red and far-red sun-induced chlorophyll fluorescence: Implications for improved estimates of gross primary productivity. *Remote Sens. Environ.* <https://doi.org/10.1016/j.rse.2016.07.025>
- Wu, C., Huang, W., Yang, Q., Xie, Q., 2015. Improved estimation of light use efficiency by removal of canopy structural effect from the photochemical reflectance index (PRI). *Agric. Ecosyst. Environ.* 199, 333–338. <https://doi.org/10.1016/j.agee.2014.10.017>
- Wu, C., Niu, Z., Tang, Q., Huang, W., 2010. Revised photochemical reflectance index (PRI) for predicting light use efficiency of wheat in a growth cycle: validation and comparison. *Int. J. Remote Sens.* 31, 2911–2924. <https://doi.org/10.1080/01431160903121118>
- Xiao, J., Zhuang, Q., Baldocchi, D.D., Law, B.E., Richardson, A.D., Chen, J., Oren, R., Starr, G., Noormets, A., Ma, S., Verma, S., Wharton, S., Wofsy, S.C., Bolstad, P.V., Burns, S.P., Cook, D.R., Curtis, P.S., Drake, B.G., Falk, M., Fischer, M.L., Foster, D.R., Gu,

- L., Hadley, J.L., Hollinger, D.Y., Katul, G.G., Litvak, M., Martin, T.A., Matamala, R., McNulty, S., Meyers, T.P., Monson, R.K., Munger, J.W., Oechel, W.C., U, K.T.P., Schmid, H.P., Scott, R.L., Sun, G., Suyker, A.E., Torn, M.S., 2008. Estimation of Net Ecosystem Carbon Exchange for the Conterminous United States by Combining MODIS and AmeriFlux Data. *Pap. Nat. Resour.*
- Xiao, X., Zhang, Q., Braswell, B., Urbanski, S., Boles, S., Wofsy, S., Moore III, B., Ojima, D., 2004. Modeling gross primary production of temperate deciduous broadleaf forest using satellite images and climate data. *Remote Sens. Environ.* 91, 256–270. <https://doi.org/10.1016/j.rse.2004.03.010>
- Yang, X., Tang, J., Mustard, J.F., Lee, J.-E., Rossini, M., Joiner, J., Munger, J.W., Kornfeld, A., Richardson, A.D., 2015. Solar-induced chlorophyll fluorescence that correlates with canopy photosynthesis on diurnal and seasonal scales in a temperate deciduous forest. *Geophys. Res. Lett.* 42, 2015GL063201. <https://doi.org/10.1002/2015GL063201>
- Yoshida, Y., Joiner, J., Tucker, C., Berry, J., Lee, J.-E., Walker, G., Reichle, R., Koster, R., Lyapustin, A., Wang, Y., 2015. The 2010 Russian drought impact on satellite measurements of solar-induced chlorophyll fluorescence: Insights from modeling and comparisons with parameters derived from satellite reflectances. *Remote Sens. Environ.* 166, 163–177. <https://doi.org/10.1016/j.rse.2015.06.008>
- Zarco-Tejada, P.J., Miller, J.R., Mohammed, G.H., Noland, T.L., Sampson, P.H., 2000. Chlorophyll Fluorescence Effects on Vegetation Apparent Reflectance: II. Laboratory and Airborne Canopy-Level Measurements with Hyperspectral Data. *Remote Sens. Environ.* 74, 596–608. [https://doi.org/10.1016/S0034-4257\(00\)00149-8](https://doi.org/10.1016/S0034-4257(00)00149-8)
- Zhang, Y., Guanter, L., Berry, J.A., Joiner, J., van der Tol, C., Huete, A., Gitelson, A., Voigt, M., Köhler, P., 2014. Estimation of vegetation photosynthetic capacity from space-based measurements of chlorophyll fluorescence for terrestrial biosphere models. *Glob. Change Biol.* 20, 3727–3742. <https://doi.org/10.1111/gcb.12664>
- Zhao, M., Running, S.W., 2010. Drought-induced reduction in global terrestrial net primary production from 2000 through 2009. *Science* 329, 940–943. <https://doi.org/10.1126/science.1192666>

Danksagung

Ich danke dem SFB/TR 32 und seinen Organisatoren dafür, dass mir die Möglichkeit gegeben wurde diese Arbeit zu verfassen.

Zu aller erst möchte ich meinen Betreuern Prof. Dr. Karl Schneider, Prof. Dr. Susanne Crewell und Prof. Dr. Uwe Rascher für die Betreuung und Begutachtung dieser Arbeit bedanken.

Ins besondere danke ich Prof. Dr. Susanne Crewell dafür, dass sie mir steht's den Rücken freigehalten hat und ich in ihrer Arbeitsgruppe meinen wissenschaftlichen Horizont erweitern durfte. Prof. Dr. Uwe Rascher danke ich für seine fachliche Unterstützung und die anregenden Diskussionen ohne die diese Arbeit so nicht möglich gewesen wäre. Prof. Dr. Karl Schneider danke ich dafür, dass er steht's ein offenes Ohr für Fragen und Probleme hatte und durch kritisches Hinterfragen diese Arbeit konsistenter hat werden lassen.

Des Weiteren danke ich Dr. Hella Ellen Ahrends für die Betreuung und Initiierung dieser Doktorarbeit. Ohne ihrer innovativen Projektidee ich mich wahrscheinlich niemals mit diesem spannenden Forschungsgebiet auseinandergesetzt hätte.

Ich möchte allen Danken die bei den Datenerhebungen und ihrer Auswertung mitgeholfen haben. Ins besondere gilt mein Dank hierbei Dr. Andreas Burkart, Dr. Anke Schickling, Patrick Rademske, Dr. Micol Rossini, Dr. Tomasso Julitta, Dr. Alexander Graf, Marius Schmidt, Prof. Dr. Matthias Langensiepen, Anja Stadler und Dr. Alexander Damm.

Mein Dank gilt außerdem den Kollegen aus der Meteorologie, insbesondere Dr. Jan Schween für die fachlichen Diskussionen und die Beantwortung meiner meteorologischen Fragen.

Vom ganzen Herzen möchte ich meinen Eltern und meinen Freunden für ihre Unterstützung und ihrem Verständnis, insbesondere in den letzten Monaten der Abgabe, bedanken. Lisa, Anna, Friederike, Sebastian auf euch mag ich nicht mehr verzichten wollen.

Quero agradecer-te Ana pelo teu apoio e pelo entusiasmo que demonstraste pelo meu trabalho. Deste um novo sabor à minha vida com o teu caos organizado.

Erklärung

Ich versichere, dass ich die von mir vorgelegte Dissertation selbstständig angefertigt, die benutzten Quellen und Hilfsmittel vollständig angegeben und die Stellen der Arbeit – einschließlich Tabellen, Karten und Abbildungen –, die anderen Werken in Wortlaut oder dem Sinn nach entnommen sind, in jedem Einzelfall als Entlehnung kenntlich gemacht habe; dass diese Dissertation noch keiner anderen Fakultät oder Universität zur Prüfung vorgelegen hat; dass sie – abgesehen von unten angegebenen Teilpublikationen – noch nicht veröffentlicht worden ist sowie, dass ich eine solche Veröffentlichung vor Abschluss des Promotionsverfahrens nicht vornehmen werde. Die Bestimmungen dieser Promotionsordnung sind mir bekannt. Die von mir vorgelegte Dissertation ist von Prof. Dr. K. Schneider betreut worden.

Köln, den 07.05.2016

Sebastian Wieneke

Teilveröffentlichungen

The analysis of GPP estimation by use of airborne based retrieved red and far-red sun induced chlorophyll fluorescence presented and discussed in Section 3.2, 4.3, 5.1, 5.2.6, 5.6, 6.1, 6.3, 6.5, 6.8, 8 and 8 has been recently published:

Wieneke, S., Ahrends, H., Damm, A., Pinto, F., Stadler, A., Rossini, M., Rascher, U., 2016. Airborne based spectroscopy of red and far-red sun-induced chlorophyll fluorescence: Implications for improved estimates of gross primary productivity. *Remote Sens. Environ.* doi:10.1016/j.rse.2016.07.025

Lebenslauf

Kontakt:	Sebastian Wieneke Trajanstr. 10 50678 Köln Deutschland Email: swieneke@meteo.uni-koeln.de
Personalien:	
Geburtsdatum	Geboren am 26.10.1981 in Steinheim, Nordrhein Westfalen, Deutschland
Staatsbürgerschaft	deutsch
Familienstand	unverheiratet, keine Kinder
Akademische- ausbildung:	
02/2012 – 11/2016	Doktorand in den Naturwissenschaften Universität zu Köln Institut für Geophysik und Meteorologie PhD Thesis: “Remote sensing of red and far-red sun-induced chlorophyll fluorescence to estimate gross primary productivity and plant stress in sugar beet” Supervisor: Prof. Dr. Karl Schneider, Prof. Dr. Susanne Crewell, Prof. Dr. Uwe Rascher, Dr. Hella Ahrends

- 04/2005 – 12/2011 Studium der Geographie (Diplom)
Philipps-Universität Marburg
Nebenfächer: Politikwissenschaften, Friedens- und
Konfliktforschung
Diplomarbeit:
“Bottom-Up” N₂O and NO_x inventory for tropical savanna
soils in northern Australia - Empirical and process based
modeling and data-induced uncertainties (Note: 1.6)
- Hauptprüfer:
Prof. Dr. Jörg Bendix (Philipps-Universität Marburg,
Institut für Geographie, Forschungsgruppenleiter
Klimageographie und Umweltmodellierung, Marburg,
Deutschland)
- Zweitprüfer:
Prof. Dr. Klaus Butterbach-Bahl (Institut für Meteorologie
und Klimaforschung – Atmosphärische Umweltforschung,
Forschungsgruppenleiter – Regionalisierung von
Treibhausgasemissionen, Garmisch-Partenkirchen,
Deutschland)
- Schulbildung:**
- 02/2002 - 1/2005 Abitur am Westfalen-Kolleg, Paderborn, NRW
- 10/1992 – 08/1998 Friedrich Wilhelm Weber Realschule, Bad Driburg, NRW
- Berufsausbildung:**
- 08/1998 – 02/2002 Ausbildung zum Industriemechaniker Fachrichtung Geräte-
und Feinwerktechnik mit Zusatzausbildung in Mechatronik,
Wincore Nixdorf, Paderborn
- Nicht
wissenschaftliches
Engagement:**
- Seit 04/2016 Mitglied des Promotionsausschusses der Mathematisch-
Naturwissenschaftlichen Fakultät der Universität zu Köln
- 06/2015 – 04/2016 Doktorandenvertreter der Mathematisch-
Naturwissenschaftlichen Fakultät der Universität zu Köln
im Albertus Magnus Graduate Center (AMGC)

04/2014 – 07/2015 Doktorandenvertreter der Meteorologie in der Geoscience Graduate School (GSGS)

04/2014 – 07/2015 Mitglied in der Steuerungsgruppe der GSGS

Veröffentlichungen: **Wieneke, S;** Ahrends, H; Damm, A; Pinto, F; Stadler A; Rossini M; Rascher U. (2016): Airborne based spectroscopy of red and far-red sun-induced chlorophyll fluorescence: Implications for improved estimates of gross primary productivity, Remote Sensing of Environment

Metzger, S; Junkermann, W; Mauder, M; Butterbach-Bahl, K; Trancón y Widemann, B; Neidl, F; Schäfer, K; **Wieneke, S;** Zheng, X H; Schmid, HP; Foken, T, 2013: Spatially explicit regionalization of airborne flux measurements using environmental response functions, Biogeosciences, 10, 2193-2217